Alexander KOSPACH

# Computational investigation of the effect of kinematic waves on jet breakup

## MASTERARBEIT

**zur Erlangung des akademischen Grades
eines Diplom-Ingenieurs**

**Masterstudium Technomathematik**

# Kurzfassung

Der Zerfall eines zylindrischen, gestörten Flüssigkeitsfreistrahles wird numerisch untersucht im kapillaren Aufbruchsregime. In Simulationen von Mehrphasenströmungen stellt die korrekte Erfassung der Phasengrenze eine schwierige Herausforderung dar. In dieser Arbeit wird die Strömung von zwei nichtmischbaren Fluiden betrachtet, konkret Wasser und Luft, unter der Verwendung von zwei verschiedenen "Volume Of Fluid" (VOF) Methoden, dem "Koren Flux limiter" Verfahren und dem "High Resolution Interface Capturing" (HRIC) Verfahren, um die Phasengrenze Wasser/Luft zu bestimmen. Gerade Vorhersagequalität des HRIC Verfahrens ist von besonderem Interesse, weil es in kommerziellen CFD Softwareprogrammen (z. B. Comet, oder Fluent) häufig verwendet wird. Für die Modellierung der Oberfächenspannungskräfte wird das "Continuum Surface Force" (CSF) Modell verwendet. Rayleigh's klassische Theorie beschreibt den kapillaren Aufbruch, induziert durch eine zeitlich wachsende Instabilität, ohne die Ausbreitung der Störung entlang der Flüssigkeitssäule zu berücksichtigen. Meier et al. (1992) widmenten sich dieser Problematik und stellten ihre experimentellen Beobachtungen einer theoretischen Beschreibung der Laufzeittheorie gegenüber, welche die gestörte Flüssigkeitsströmung durch die Lösung einer instationären eindimensionalen Impulsgleichung unter der Vernachlässigung von Reibungs- und Oberflächenkräften beschreibt. Eine Reihe von gestörten Flüssikeitsstrahlen wurde simuliert mit unterschiedlichen Amplituden und Frequenzen der Geschwindigkeitsmodulation am Einströmrand. Die numerischen Ergebnisse haben gezeigt, dass die Laufzeittheorie ziemlich gut die Bedingungen am Düseneintritt wiedergibt, während die Bedingungen stromaufwärts vom Punkt des Strahlzerfalles im Wesentlichen von Rayhleigh's Theorie des kapillaren Aufburchs bestätigen. Verglichen mit den Experimenten von Meier et al. (1992) ergaben die numerischen Simulationen im Allgemeinen längere Aufbruchlängen. Die vorausgesagten Änderungen der Aufbruchlänge für veränderte Geschwindigkeitsmodulationen am Düseneintritt zeigten jedoch die gleichen Tendenzen wie in den Experimenten.

# Abstract

The disintegration of a perturbed liquid cylindrical jet in the capillary breakup regime is numerically investigated. In multi-phase flow simulations the accurate capturing of the interface is a challenging task. The present work considers the flow of two immiscible fluids, i.e. water and air, using two different volume of fluid (VOF) approaches, the Koren flux limiter scheme and the high resolution interface capturing (HRIC) scheme to capture the liquid/gas interface. The performance of the HRIC scheme is of special interest, because it is used in popular commercial CFD software (e.g. Comet, Fluent). The surface tension force is computed using the continuum surface force (CSF) model. Rayleigh's classical theory describes the capillary breakup induced by a temporally growing instability, without considering the propagation of the perturbation along the liquid column. Meier et al. (1992) addressed this issue by analyzing their experimental observations against a theoretical description of the travelling time theory, which assumes the perturbed liquid flow as being governed by a transient one-dimensional equation of motion neglecting viscous and surface tension forces. A series of perturbed liquid jets were simulated varying the amplitudes and frequencies of the inflow velocity modulations. The numerical solutions showed that the travelling time theory fairly well describes the conditions near the nozzle, while the conditions near the liquid breakup occurring further downstream essentially confirms Rayleigh's theory on capillary breakup. As compared to the experiments of Meier et al. (1992) the numerical simulations generally overpredicted the disintegration lengths. The predicted changes in the disintegration length for varying inflow velocity modulations still exhibited the same tendencies as seen in the experiments.

# Acknowledgment

# Contents

# Nomenclature

## Roman symbols

| Symbol | Description | Dimension |
|--------|-------------|-----------|
| $c$ | color function | $[-]$ |
| $Co$ | Courant number | $[-]$ |
| $D$ | diameter | $[\text{m}]$ |
| $d$ | number of faces of the control volume | $[-]$ |
| $\mathbf{d}$ | normal vector to the cell face | $[\text{m}]$ |
| $f$ | frequency | $[1/\text{s}]$ |
| $\mathbf{f}$ | force vector | $[\text{N}]$ |
| $F$ | numerical flux | $[-]$ |
| $\mathcal{F}$ | filtering | $[-]$ |
| $G$ | cross-sectional area of the jet | $[\text{m}^2]$ |
| $\mathbf{g}$ | volumetric gravitational acceleration force | $[\text{m/s}^2]$ |
| $h$ | disturbance radius | $[\text{m}]$ |
| $\mathbf{I}$ | unit tensor | $[-]$ |
| $K$ | kinematic energy | $[\text{J}]$ |
| $\mathbf{K}$ | kernel of smoothing | $[-]$ |
| $k$ | wave number | $[\text{m}^{-1}]$ |
| $m$ | mode | $[-]$ |
| $\mathbf{n}$ | normal unit vector at the boundary | $[\text{m}]$ |
| $Oh$ | Ohnesorge number | $[-]$ |
| $p$ | pressure | $[\text{N/m}^2]$ |
| $P$ | surface energy | $[\text{J}]$ |
| $R$ | principal radius of curvature of the surface | $[\text{m}]$ |
| $r$ | radial coordinate | $[\text{m}]$ |
| $Re$ | Reynolds number | $[-]$ |
| $S$ | surface | $[\text{m}^2]$ |
| $s$ | ratio of consecutive gradients | $[-]$ |
| $\mathbf{T}$ | stress tensor | $[\text{N/m}^2]$ |
| $t$ | time | $[\text{s}]$ |
| $\mathbf{S}$ | rate of strain tensor | $[\text{s}^{-1}]$ |
| $\overline{U}$ | average advection velocity | $[\text{m/s}]$ |
| $\mathbf{u}$ | velocity vector $[u\ v\ w]$ | $[\text{m/s}]$ |
| $V$ | volume | $[\text{m}^3]$ |
| $We$ | Weber number | $[-]$ |
| $y$ | lateral extension | $[\text{m}]$ |
| $z$ | axial coordinate | $[\text{m}]$ |

# Greek Symbols

| Symbol | Description | Dimension |
|--------|-------------|-----------|
| $\alpha$ | growth or damping function of the disturbance | [m] |
| $\beta$ | parameter | $[-]$ |
| $\Gamma$ | surface of the computational domain | [m$^2$] |
| $\gamma$ | flux limiter function | $[-]$ |
| $\epsilon$ | amplitude | $[-]$ |
| $\zeta$ | blending factor | $[-]$ |
| $\theta$ | cross-flow coordinate | [rad] |
| $\vartheta$ | actual time in Lagrange coordinates | [s] |
| $\kappa$ | mean curvature | [m$^{-1}$] |
| $\lambda$ | wave length | [m] |
| $\mu$ | dynamic viscosity | [kg/ms] |
| $\xi$ | potential | [m$^2$/s] |
| $\rho$ | density | [kg/m$^3$] |
| $\sigma$ | surface tension coefficient | [N/m] |
| $\tau$ | starting time of the flow particles in Lagrange coordinates | [s] |
| $\phi$ | azimuthal coordinate | [rad] |
| $\Phi$ | arbitrary velocity component | [m/s] |
| $\omega$ | growth rate | $[-]$ |
| $\nabla$ | vector of spatial derivatives | [m$^{-1}$] |

# Subscripts and Superscripts

| Symbol | Description |
|--------|-------------|
| 0 | reference quantities |
| 1 | denotes fluid one, i.e. water |
| 2 | denotes fluid two, i.e. air |
| $b$ | body |
| $C$ | center cell |
| $D$ | downwind cell |
| $exp$ | experiment |
| $f$ | face value |
| $i$ | indices of the disrcetized radial coordinate |
| $in$ | inflow |
| $inl$ | inlet of the liquid |
| $j$ | indices of the discretized cross-flow coordinate |
| $k$ | indices of the discretized azimuthal coordinate |
| $lat$ | lateral |
| $out$ | outflow |
| $p$ | control volume for $p$ |
| $*$ | dimensionless parameter |
| $n$ | time step iterator |
| $sim$ | simulated |
| $T$ | travelling time theory |
| $U$ | upwind cell |
| $u$ | control volume for $u$ |
| $v$ | control volume for $v$ |
| $w$ | control volume for $w$ |
| $\Phi$ | control volume for $\Phi$ |
| $\sigma$ | dependency on the surface tension |

# Abbreviations

CDS      central difference scheme
CSF      continuum surface force
ECBC     extended boundedness criterion
GCBC    general convective boundedness criterion
GL-CBC  Gaskell and Lau's convection-boundedness criterion
HRIC     high resolution interface capturing
ICM      interface capturing methods
ITM      interface tracking methods
LUI      linear-upwind interpolation
MAC     marker and cell
NVD     normalized variable diagram
KFL      Koren flux limiter
PLIC     piecewise linear interface calculation
SLIC     simple line interface calculation
SOU     second order upwind
TVD     total variation diminishing
VOF     volume of fluid

# 1 Introduction

The computational investigation of the effect of kinematic waves on liquid jet breakup is motivated through the importance of the phenomenon of jet breakup. The disintegration of a liquid column can be found in many industrial applications. One application is in inkjet printing, where printers use this phenomenon for a highly controlled generation of small droplets to be deposited on a substrate. Another typical application is the atomization using spray nozzles, where a continuous stream of liquid is rapidly disintegrated into a highly dispersed distribution of small droplets. It is hypothesized that jet breakup also occur in our lungs, Duclaux and Clanet (2004).
The breakup of liquid jets was already described in the pioneering work of Lord Rayleigh (Rayleigh, 1878). Rayleigh applied a linear stability analysis to an infinite liquid cylinder, where he could determine the most unstable perturbation mode, which grows in amplitude with time, so that the column finally breaks up into a sequence of individual droplets. Rayleigh's results were confirmed in various experimental studies, like those of Haenlein (1931), Goedde and Yuen (1970) and others, although all of these experimental investigations on jet breakup compared the observed spatial growth rates with the temporal growth rates obtained from Rayleigh's analysis. Keller and Rubinow (1973) addressed this inconsistency, and they therefore solved the dispersion equation governing the Rayleigh breakup regime for critical modes which lead to spatially increasing perturbations instead of temporally increasing perturbations. They found that the critical modes for spatial and temporal growth rates coincide at large Weber numbers $We = \frac{\rho u^2 D_{inl}}{\sigma} >> 1$. Considering an infinitely long liquid column all the aforementioned theoretical studies miss an important aspect inherently met in real jet flow conditions: the travelling time effects of the perturbations triggered at the nozzle exit. Following simple kinematic considerations the variation of the starting velocity of the fluid elements at the inflow leads to the formation of kinematic waves. Since the fluid elements injected with a higher velocity tend to surpass the slower moving elements injected with a lower velocity before, the kinematic waves steepen on their way downstream resulting in a significant distortion of the jet. Grabitz and Meier (1983) investigated this effect providing an exact analytical solution of the one-dimensional Euler equation based on the travelling time theory to describe the evolution of the distorted liquid column downstream of the orifice. Meier et al. (1992) conducted a comprehensive series of experiments, where they investigated the effect of kinematic waves on jet break-down, which are triggered by inlet velocity modulations with different frequencies and amplitudes. For the higher amplitudes they observed a fairly good agreement with the results of the one-dimensional theoretical solution calculated with the travelling time theory.
The present work numerically investigated the disintegration of a perturbed liquid

cylindrical jet in the capillary breakup regime. It shall be shown to which extent the used computational approach can reflect the evolution of the disturbance until the breakup of the liquid core, as it was observed in the experiment by Meier et al. (1992). The comparison of the numerical results against the solution calculated with the travelling time theory shall further give insight into the influence of the capillary forces on the propagating disturbances, which is neglected in the travelling time theory. The numerical simulations will consider some selected cases of the experiments of Meier et al. (1992) varying the frequency and the amplitude of the sinusoidal velocity perturbations. In these computations the incompressible Navier-Stokes equations are numerically solved using the Volume-of-Fluid (VOF) method as two-phase flow model (Hirt and Nichols, 1981). For the advection of the liquid-gas interface two different VOF methods, the Koren flux limiter schem (Koren, 1993), and the high resolution interface capturing (HRIC) scheme (Muzaferija et al., 1998), are tested and compared. The obtained results shall also give insight into the performance of these alternative approaches for treating the interface.

In chapter two the mathematical model is described in detail. The conservation laws are formulated assuming the two-phase distribution as a one-fluid continuum. For this approach constitutive relations are needed, and a color function is introduced. The color function is by definition one at a point inside liquid phase and is zero at a point inside the gas phase. To account for surface tension effects the continuum surface force (CFS) model is used (Brackbill et al., 1992). The model interprets surface tension as a continuous volumetric force acting in a volume containing an interface, rather than as a dynamic boundary condition imposed at the sharp interface. Allowing for a scaling to real flow conditions the governing equations are transformed to dimensionless form using appropriate normalizations.

In chapter three an outline is given of the numerical model which is used to solve the governing equations. The jet breakup of a water column is numerically simulated using a cone-shaped computational domain, which is based on a spherical coordinate system. A staggered grid is used, where the scalar variables are stored at the cell centers of the control volumes and the velocity components are located at the cell faces. Using a pressure-based incompressible flow solver the continuity equation is not explicitly solved. The satisfaction of the continuity equation is incorporated into the solution procedure of the momentum equations instead. For the integration of the color function equation in time an explicit second-order accurate Adams-Bashfort scheme is used. For integrating the equation of motion in time the so called "projection method", (Prosperetti and Tryggvason, 2007), is used. For the spatial discretization a finite volume approach is applied. Inflow, lateral and outflow boundary conditions for all unknown variables are imposed. For the present case of a free jet flow the outflow boundary requires special attention to ensure numerical stability by eliminating undesirable effects as far as possible.

In chapter four an introduction to volume of fluid (VOF) methods (Hirt and Nichols,

1981) is given. The VOF method represents a very popular approach among various other methods which have been developed for the challenging problem of interface propagation in multiphase flow calculations. Basically, they can be classified into two groups (Ferziger and Peric, 1996): First, interface tracking methods which define a sharp interface, whose motion is followed. Secondly, interface capturing methods which solve the equations of interest in the whole domain on a fixed grid and the fluids on either side of the interface are marked. Two typical examples of interface capturing methods are marker and cell (MAC) methods (Harlow and Welch, 1965), and VOF methods. In the VOF method a transport equation for the color function is introduced. VOF methods can be categorized into two groups dependent, how they deal with the color function equation. First, the interface reconstruction methods use the idea of geometric interface reconstruction. The transport equation of color function equation is not directly discretized to obtain a discrete algebraic representation of the underlying differential transport equation. Instead, geometrical considerations are used to model adequately the convection of the color function. Different interface reconstruction methods were proposed and some of the more important ones are mentioned. The second category are the high resolution schemes. The term "high resolution" scheme , introduced by Harten (1983), represents a class of conservative schemes which produce solutions free from spurious oscillations and with high accuracy especially near discontinuities met in compressible flows like shocks, or contact surfaces. As such, the class of high resolution schemes also provides good candidates for the numerical solution of the color function equation. High resolution schemes are essentially based on a flux limiter function approach or a normalized variable diagram (NVD) approach. The general ideas of this concepts are given, and the two schemes used in the present work, the Koren flux limiter scheme and the HRIC scheme, are described in detail. Finally, a comparison between the two schemes is shown for a simple one-dimensional test simulation.

In chapter five some important theories on the disintegration of jets are discussed. The classical theory of Lord Rayleigh (Rayleigh, 1878) describes the disintegration of liquid jets in the so called capillary breakup regime, where surface tension plays a dominant role. Among other possibly destabilizing effects like aerodynamic forces or turbulent fluctuations it has been shown by Meier et al. (1992), that pure kinematic effects can strongly drive the disintegration of a jet as well without considering any surface or body forces, which is generally termed travelling time theory.

In chapter six the numerical results are described in much detail. The fully converged numerical solutions are compared against the corresponding experimental observation of Meier et al. (1992) and against the predictions of the travelling time theory. The observed agreement as well the discrepancies between the numerical/analytical results and the experiments are discussed and interpreted.

In chapter seven conclusions from the most important findings are drawn, and suggestions based on the results for future work are given.

# 2 Mathematical Model

The jet breakup of a water column surrounded by air is computationally investigated using a continuum mechanics approach. The mathematical model for describing the underlying transport phenomena of the two involved immiscible incompressible fluids is the subject of this chapter. There are two possible ways of describing the flow of two immiscible fluids:

- The whole domain of interest is divided into two subdomains by the interface. For each subdomain the Navier-Stokes equations are solved for a single phase incompressible flow and the two subdomains are connected via appropriate boundary conditions. Surface tension effects must be incorporated into the boundary conditions.

- For the whole domain of interest just one single set of governing equations is solved. For this approach it is necessary to account for differences in the material properties of the different fluids and to add appropriate interface terms for the interfacial phenomena, such as surface tension, (Prosperetti and Tryggvason, 2007).

In this work the second approach is used. The governing conservation laws and the methodology for incorporating the interface effects are described in this chapter.

## 2.1 Conservation laws

The fluid flow is mathematically described by three conservation laws, the conservation of mass, momentum and energy. These laws completely determine the physical behaviour of the fluid. Considering isothermal incompressible flow just the conservation of mass and momentum are needed to get a closed form for the unknown quantities $\mathbf{u}$ and $p$.

### Conservation of mass

In classical mechanics mass can neither be produced nor destroyed. Thus, the temporal change of mass in a finite volume must be balanced by the net fluxes across the surface of the volume. In a mathematical framework the conservation of mass can be written as

$$\int_V \frac{\partial \rho}{\partial t} \, dV = -\int_S \rho \mathbf{u} \cdot \mathbf{n} \, dS. \tag{2.1}$$

Here $\rho$ is the density and $\mathbf{u}$ is the fluid velocity vector, $S = \partial V$ the boundary of $V$, and $\mathbf{n}$ the cell-normal unit vector. By applying Gauss' theorem to equation (2.1) the differential form

$$\frac{\partial \rho}{\partial t} + \nabla \cdot (\rho \mathbf{u}) = 0 \tag{2.2}$$

is obtained. This equation is often called the continuity equation, see for instance Spurk and Aksel (2007).

## Conservation of momentum

In analogy to mass conservation, the momentum conservation can also be derived from a finite volume consideration. Applying Newton's second law to fluid motion, the temporal change of momentum within a volume, including the momentum fluxes across its surface must be balanced by external surface and body forces. This balance is written as

$$\int_V \frac{\partial \rho \mathbf{u}}{\partial t}\, dV + \int_S (\rho \mathbf{u}\mathbf{u}) \cdot \mathbf{n}\, dS = \int_S \mathbf{T} \cdot \mathbf{n}\, dS + \int_V \mathbf{f}_b\, dV. \tag{2.3}$$

Here, $\mathbf{T}$ is the stress tensor and $\mathbf{f}_b$ is the volumetric body force. Again Gauss' theorem is applied and the differential form of the momentum equation is derived:

$$\frac{\partial \rho \mathbf{u}}{\partial t} + \nabla \cdot (\rho \mathbf{u}\mathbf{u}) = \nabla \cdot \mathbf{T} + \mathbf{f}_b \tag{2.4}$$

The diadic vector product $\mathbf{u}\mathbf{u}$ is defined as:

$$\mathbf{u}\mathbf{u} := \mathbf{u} \cdot \mathbf{u}^\top.$$

Assuming a Newtonian fluid the stress tensor is written as, see for instance Spurk and Aksel (2007),

$$\mathbf{T} = \left(-p - \frac{2}{3}\mu \nabla \cdot \mathbf{u}\right) \mathbf{I} + 2\mu \mathbf{S}, \tag{2.5}$$

where $p$ is the pressure, $\mu$ the dynamic viscosity of the fluid, $\mathbf{S} = \frac{1}{2}\left(\nabla \mathbf{u} + (\nabla \mathbf{u})^\top\right)$ the rate of strain tensor and $\mathbf{I}$ the unit tensor. The volumetric body force is composed of a contribution due to gravitational forces and a contribution due to surface tension forces:

$$\mathbf{f}_b = \rho \mathbf{g} + \mathbf{f}_\sigma$$

In the present work the effect of the gravitational forces is neglected, so that the only body force is $\mathbf{f}_\sigma$, which is due to surface tension. Basically surface tension is a tensile force tangential to the interface separating the two fluids, which tries to keep the fluid molecules at the free boundary in contact with the rest of the fluid. Its magnitude depends mainly of the material properties of the two fluids and the geometrical shape of the interface. Although it acts only at the interface, the surface tension is modeled here as a volumetric body force following the continuum surface force (CFS) model proposed by Brackbill et al. (1992). A detailed description of this surface force model is given in section 2.3.

## 2.2 Constitutive relations

Constitutive relations have to be added to account for the different densities and material properties of the two fluids. The local density and viscosity are computed as

$$\rho = c\rho_1 + (1-c)\rho_2, \tag{2.6}$$

$$\mu = c\mu_1 + (1-c)\mu_2, \tag{2.7}$$

respectively, where the subscripts 1 and 2 denote the different fluids. The function $c$ is called *color function* and is defined as:

$$c(\mathbf{x}, t) = \begin{cases} 1 & \text{for the point } (\mathbf{x}, t) \text{ inside fluid 1} \\ 0 & \text{for the point } (\mathbf{x}, t) \text{ inside fluid 2} \end{cases} \tag{2.8}$$

With the above definitions two main difficulties arise:

- The density and the viscosity are piecewise continuous functions and are not differentiable in the classical sense over the whole flow domain.

- Surface tension creates a pressure jump $\Delta p$ across a curved surface and the pressure jump manifests itself only at the interface.

## 2.3 Continuum surface force model

The continuum surface force (CSF) model, introduced by Brackbill et al. (1992), is used here to overcome the difficulties mentioned at the end of the previous subsection. The model interprets surface tension as a continuous volumetric force acting in a volume containing an interface, rather than as a dynamic boundary value condition imposed at the sharp interface.

Before explaining the CSF model in more detail some general aspects of surface tension are said in advance. At the interface of fluids surface tension occurs. Surface tension is an effect of attractive forces within the fluid at a microscopic level. These forces act uniformly into all directions at particles inside the fluid. On the interface the forces just act on one side because only particles of the same phase interact with each other. In consequence the fluid has a tendency to minimize its surface area. The surface tension coefficient $\sigma$ is defined as the force along a line of unit length, where the force is parallel to the surface but normal to the line, see for instance Spurk and Aksel (2007). Surface tension is therefore measured in force per unit length. An important aspect of surface tension is that it creates a pressure jump $\Delta p$ across a curved surface. Based on a simple force balance at the interface it can be shown that the magnitude of the pressure jump is a function of the mean interface curvature and the surface tension coefficient

$$\Delta p = p_i - p_o = \sigma \left( \frac{1}{R_1} + \frac{1}{R_2} \right) = \sigma \kappa, \tag{2.9}$$

where $R_1$ and $R_2$ are the principal radii of curvature of the surface, $\kappa$ the mean curvature, and $p$ the pressure. The higher pressure is always on the concave side of the interface, since surface tension results in a net normal force directed towards the center of curvature of the interface.

In the CSF model the pressure jump $\Delta p$ is included into the momentum equations as a volume force $f_\sigma = \nabla p$ concentrated at the interface. The problem of non-differentiability is overcome by introducing a transition region of small but finite thickness $h$. Accordingly the color function is redefined as follows:

$$c(\mathbf{x}, t) = \begin{cases} 1 & \text{for the point}(\mathbf{x}, t) \text{ inside fluid 1} \\ 0 & \text{for the point}(\mathbf{x}, t) \text{ inside fluid 2} \\ 0 < c < 1 & \text{for the point}(\mathbf{x}, t) \text{ inside the transition region} \end{cases}$$

To achieve such smoothly varying function $c$ is convolved with a smooth kernel $\mathbf{K}$, which is as assumed as a quadratic B-spline. The new continuous color function $c$ is twice differentiable. In figure 2.1(a) the transition region with a line $ab$ normal to the different layers of the interface is shown. In figure 2.1(b) the smooth change of the color function and the pressure profile in the transition region can be seen. It is assumed that the variation of the pressure coincides in the transition region with the variation of the color function.

   Under the above assumptions and assuming a constant surface tension coefficient $\sigma$
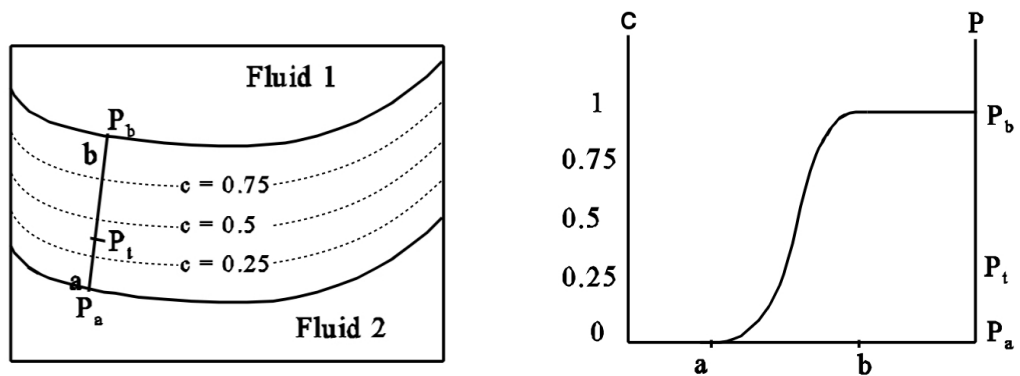


(a) Transition region with a line $ab$ normal to the different iso-contours of the color function.

(b) Coincident change of the color function and the pressure profile.

Figure 2.1: Representation of the transition region. Figures from Ubbink (1997).

Brackbill et al. (1992) derived a volume force written as

$$\mathbf{f}_\sigma(\mathbf{x}) = \sigma\kappa(\mathbf{x})\nabla c(\mathbf{x}). \tag{2.10}$$

Since $\nabla c$ is only non-zero in the transition region, the volumetric surface tension force $\mathbf{f}_\sigma$ acts only in the transition region. The curvature of an arbitrary surface $S$ at $\mathbf{x}_S$,

$\kappa$, is calculated from

$$\kappa(\mathbf{x}) = -\nabla \cdot \hat{\mathbf{n}}(\mathbf{x}), \qquad (2.11)$$

where $\hat{\mathbf{n}}$ is the unit normal to the surface pointing into fluid 1 (see figure 2.1(a)). The normal vector is obtained from the gradient of the smoothed color function

$$\mathbf{n}(\mathbf{x}) = \nabla c(\mathbf{x}). \qquad (2.12)$$

Using equation (2.12) the curvature $\kappa$ is computed as

$$\kappa = \nabla \cdot \hat{\mathbf{n}} = -\nabla \cdot \left( \frac{\nabla c}{\|\nabla c\|} \right). \qquad (2.13)$$

The equation shown above for the curvature implird that for $\kappa > 0$ fluid 1 lies on the concave side of the interface and for $\kappa < 0$ fluid 1 lies on the convex side as shown in figure 2.2. Substituting (2.13) into (2.10) the volumetric surface tension force $\mathbf{f}_\sigma$ is
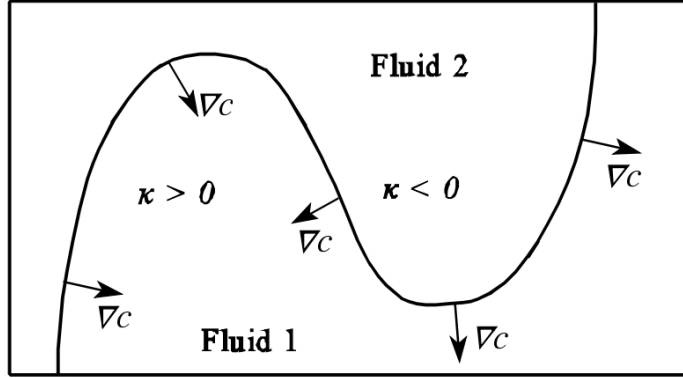


Figure 2.2: The gradient of the color function $\nabla c$ and the sign of the curvature $\kappa$. Figure form Ubbink (1997).

obtained just as only dependent of the color function $c$:

$$\mathbf{f}_\sigma = -\sigma \left( \nabla \cdot \left( \frac{\nabla c}{\|\nabla c\|} \right) \right) \nabla c \qquad (2.14)$$

It should be mentioned at this point that using the CSF method does not necessarily require a smoothening of the color function. Several authors have directly implemented a numerical approximation of equation (2.14) without smoothening the color function, and no major problems occurred, see for instance Scardovelli and Zaleski (1999). Using the HRIC scheme in the present calculations, as will be shown, smoothening is required.

## 2.4 Transport equation for the color function for incompressible phases

As noted as well by Hirt and Nichols (1981), the assumption of the incompressibility of both fluids implies that the color function $c$ has a zero material derivative, such that

$$\frac{Dc}{Dt} = \frac{\partial c}{\partial t} + \mathbf{u} \cdot \nabla c = 0. \tag{2.15}$$

By a reformulation of the continuity equation the incompressibility condition can be extended to a "single fluid" approach, as shown below:

$$\begin{aligned}
\nabla \cdot \mathbf{u} &= -\frac{1}{\rho}\left(\frac{\partial \rho}{\partial t} + \mathbf{u} \cdot \nabla \rho\right) = -\frac{1}{\rho}\frac{D\rho}{Dt} \\
&= -\frac{1}{\rho}\frac{D}{Dt}\left(c(\rho_1 - \rho_2) + \rho_2\right) \\
&= \frac{\rho_2 - \rho_1}{\rho}\frac{Dc}{Dt} = 0
\end{aligned}$$

## 2.5 Governing set of equations

The dimensional governing set of equations is rewritten, below in equations (2.16).

$$\frac{\partial \rho}{\partial t} + \nabla \cdot (\rho \mathbf{u}) = 0 \tag{2.16a}$$

$$\frac{\partial \rho \mathbf{u}}{\partial t} + \nabla \cdot (\rho \mathbf{u}\mathbf{u}) = -\nabla p + \nabla \cdot \left(\mu\left(\nabla \mathbf{u} + (\nabla \mathbf{u})^{\top}\right)\right) + \mathbf{f}_{\sigma} \tag{2.16b}$$

$$\frac{\partial c}{\partial t} + \nabla \cdot (c\mathbf{u}) = 0 \tag{2.16c}$$

$$\rho = c\rho_1 + (1-c)\rho_2 \tag{2.16d}$$

$$\mu = c\mu_1 + (1-c)\mu_2 \tag{2.16e}$$

It represents a closed system of equations, which can be solved for the primitive variables $\mathbf{u}$, $p$ and $c$.

Experimental studies of flows are mostly carried out on a laboratory scale, and the results are presented in dimensionless form, thus allowing for a rescaling to real flow conditions. The same approach can be adopted in numerical studies as well. The governing equations are transformed to dimensionless form using appropriate normalizations, which relate all variables to characteristic reference quantities, (Ferziger and Peric, 1996).
Introducing the reference quantities $L_0$, $U_0$, $\rho_0$ and $\mu_0$ the dimensionless variables for

the presently considered problem can be written as

$$x_i^* = \frac{x_i}{L_0}, \quad t^* = \frac{tU_0}{L_0}, \quad \mathbf{u}^* = \frac{\mathbf{u}}{U_0}, \tag{2.17a}$$

$$\mu^* = \frac{\mu}{\mu_0}, \quad \rho^* = \frac{\rho}{\rho_0}, \quad p^* = \frac{p}{\rho_0 U_0^2}, \quad \mathbf{f}_\sigma^* = \frac{L_0^2 \mathbf{f}_\sigma}{\sigma}. \tag{2.17b}$$

It is noted that no non-dimensionalization is required for $c$, which is already dimensionless by definition. Substituting the dimensionless groups into the governing equations the dimensionless representation is obtained as:

$$\frac{\partial \rho^*}{\partial t^*} + \nabla^* \cdot (\rho^* \mathbf{u}^*) = 0 \tag{2.18a}$$

$$\frac{\partial \rho^* \mathbf{u}^*}{\partial t^*} + \nabla^* \cdot (\rho^* \mathbf{u}^* \mathbf{u}^*) = -\nabla^* p^* + \frac{1}{\mathrm{Re}} \nabla^* \cdot \left( \mu^* \left( \nabla^* \mathbf{u}^* + (\nabla^* \mathbf{u}^*)^\top \right) \right) + \frac{1}{\mathrm{We}} \mathbf{f}_\sigma^* \tag{2.18b}$$

$$\frac{\partial c}{\partial t^*} + \nabla^* \cdot (c \mathbf{u}^*) = 0 \tag{2.18c}$$

$$\rho^* = c\rho_1^* + (1 - c)\rho_2^* \tag{2.18d}$$

$$\mu^* = c\mu_1^* + (1 - c)\mu_2^* \tag{2.18e}$$

The following dimensionless numbers appear in the equations:

- The Reynolds number

$$\mathrm{Re} := \frac{\rho_0 U_0 L_0}{\mu_0}$$

  can be understood as a ratio of inertial and viscous forces. They are also used to characterize different flow regimes, such as laminar or turbulent flow. Laminar flow occurs at low Reynolds numbers, where viscous forces are dominant, and turbulent flow occurs at high Reynolds numbers and is dominated by inertial forces. The critical Reynolds number, where the flow becomes unstable and a transition from laminar to turbulent occurs, depends on the considered flow configuration.

- The Weber number

$$\mathrm{We} := \frac{\rho_0 U_0^2 L_0}{\sigma}$$

  is the ratio of inertial forces to surface tension forces. It represents an important parameter to identify the different regimes of liquid breakup ranging from capillary breakup to spray atomization.

In the next chapter the numerical simulation methodology is discussed to explain in detail the numerical methods used in the present computational investigations.

# 3 Numerical Model

In this chapter an outline is given of the numerical model which is used to solve the governing equations. A numerical code, originally written by Boersma (1998), is used as a flow solver tool for the present computations. It was primarily developed to simulate single-phase cylindrical jet flow and it is written in Fortran and parallelized with message passing interface (MPI). It was extended to deal with the two-phase flow problem of atomizing high-speed liquid jets, (Heidron and Steiner, 2009). The dimensionless governing equations (2.16a) - (2.16e) are solved in spherical coordinates. The numerical method for solving the governing equations (2.18a) - (2.18e) is discussed in the following separately for the time and space discretization.

## 3.1 Computational domain

The jet breakup of a water column is numerically simulated using a cone-shaped computational domain, which is based on a spherical coordinate system. The com-
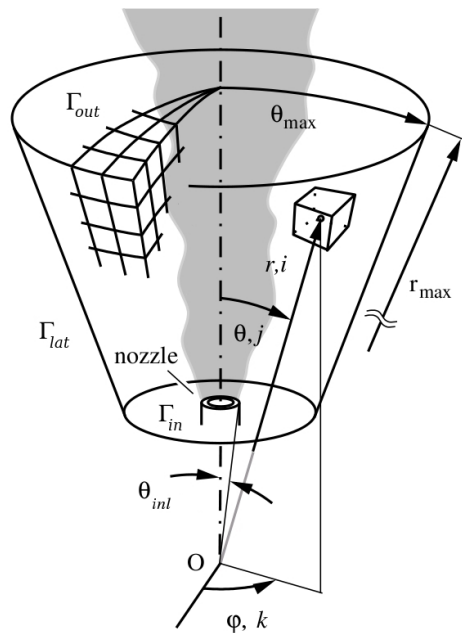


Figure 3.1: Schematical view of the computational domain. Figure from Walchshofer (2011).

putational domain is shown in figure 3.1. The indices of the discretized spherical coordinates $r$, $\theta$, $\phi$ are denoted by $i$, $j$ and $k$, respectively. The inflow boundary is denoted by $\Gamma_{in}$, the lateral by $\Gamma_{lat}$ and the outflow by $\Gamma_{out}$. Using a spherical coordinate system instead of a cylindrical was originally motivated to account inherently for the lateral expansion of the jet with increasing distance from the orifice, so that a sufficient distance between the outer edge of the boundary layer and the lateral boundary $\Gamma_{lat}$ is guaranteed. Thus, a significant motion generated by the jet basically never reaches the lateral boundary, which would trigger numerical instabilities. In the present simulations the radial distance of the inflow boundary is chosen large enough, to obtain an almost cylindrical computational domain with a cylindrical jet at the inflow.

## 3.2 Time discretization

The time discretization is relevant only for the solution of transport equations for the color function and the momentum. Using a pressure-based incompressible flow solver the continuity equation is not explicitly solved. The satisfaction of the continuity equation is incorporated into the solution procedure of the momentum equations instead.

### Transport equation for the color function

For the integration of the color function equation (2.16c) in time an explicit second-order accurate Adams-Bashforth scheme is used:
$$\frac{c^{n+1} - c^n}{\Delta t} = \frac{3}{2}A_c^n - \frac{1}{2}A_c^{n-1}.$$
Therein, $A_c^n$ represents the numerical approximation of the advection term at time $t^n$, hence
$$A_c^n \approx -\nabla \cdot (c^n \mathbf{u}^n).$$
The computation of the advection term is a non-trivial task, because the steep gradients of the color function has to be maintained. Using a diffusive upwind scheme would excessively smear the gradient so the interfaces between the phases can finally not clearly identified any more. Using on the other hand a very compressive downwind scheme leads to unphysical minima and maxima, which finally leads to an unstable solution. A detailed discussion of this important issue will be presented in section 4.

### Momentum equation

For integrating the equations of motion (2.16b) in time the so called "*projection method*", see for example Prosperetti and Tryggvason (2007), is used. This approach can be divided into three main steps, namely the predictor step, projection step and pressure correction step.

1. *Predictor step:*
   First the momentum flux $\widehat{\rho\mathbf{u}}$ is calculated without accounting for the pressure as follows using the same Adams-Bashforth scheme as shown above for the color function $c$:

   $$\frac{\widehat{(\rho\mathbf{u})} - (\rho\mathbf{u})^n}{\Delta t} = \frac{3}{2}\left(\mathbf{A}_\mathbf{u}^n + \mathbf{D}_\mathbf{u}^n + \mathbf{f}_\sigma^n\right) - \frac{1}{2}\left(\mathbf{A}_\mathbf{u}^{n-1} + \mathbf{D}_\mathbf{u}^{n-1} + \mathbf{f}_\sigma^{n-1}\right) \qquad (3.1)$$

   $\mathbf{A}_\mathbf{u}^n$ is the numerical approximation of the advection term at time $t^n$, hence

   $$\mathbf{A}_\mathbf{u}^n \approx -\nabla \cdot (\rho^n \mathbf{u}^n \mathbf{u}^n).$$

   $\mathbf{D}_\mathbf{u}^n$ is the numerical approximation of the diffusion term at time $t^n$, hence

   $$\mathbf{D}_\mathbf{u}^n \approx \nabla \cdot \left(\mu^n \left(\nabla \mathbf{u}^n + (\nabla \mathbf{u}^n)^\top\right)\right).$$

   $\mathbf{f}_\sigma^n$ is the numerical approximation of the surface tension term at time $t^n$, hence

   $$\mathbf{f}_\sigma^n \approx -\sigma \kappa^n \nabla c^n.$$

   The resulting velocity obtained from

   $$\hat{\mathbf{u}} = \frac{\widehat{\rho\mathbf{u}}}{\rho^{n+1}}$$

   with $\rho^{n+1} = \rho_1 c^{n+1} + (1 - c^{n+1})\rho_2$ is in general not divergence-free, so that it does not satisfy the continuity equation $\nabla \cdot \hat{\mathbf{u}} = 0$.

2. *Projection step:*
   In the second step the pressure gradient is added to yield the final momentum flux at the new time step:

   $$\frac{(\rho\mathbf{u})^{n+1} - \widehat{(\rho\mathbf{u})}}{\Delta t} = -\nabla p^{n+1} \qquad (3.2)$$

   The pressure at time step $n + 1$ is also unknown and must be calculated as well. Equation (3.2) is divided by the new density $\rho^{n+1}$, which yields

   $$\mathbf{u}^{n+1} - \underbrace{\frac{\widehat{(\rho\mathbf{u})}}{\rho^{n+1}}}_{=:\tilde{\mathbf{u}}} = -\frac{\Delta t}{\rho^{n+1}} \nabla p^{n+1}. \qquad (3.3)$$

   Taking the divergence of equation (3.3) and enforcing a divergence-free velocity at the new time, i. e. $\nabla \cdot \mathbf{u}^{n+1} = 0$, gives the Poisson equation for the pressure

   $$\nabla \cdot \left(\frac{\Delta t}{\rho^{n+1}} \nabla p^{n+1}\right) = \nabla \cdot \tilde{\mathbf{u}}. \qquad (3.4)$$

   The solution of the Poisson equation is one of the most challenging problems concerning the accuracy and computational costs. The Poisson equation (3.4) is solved using an algebraic multigrid algorithm.

3. *Pressure correction step:*
   To get the final divergence-free velocity $\mathbf{u}^{n+1}$ at time step $t^{n+1}$, the predicted velocity $\tilde{\mathbf{u}}$ is corrected by the gradient of the pressure:

$$\mathbf{u}^{n+1} = \tilde{\mathbf{u}} - \frac{\Delta t}{\rho^{n+1}} \nabla p^{n+1}.$$

## 3.3 Space discretization

For the space discretization a finite volume approach is used. The great advantage of using a finite volume approach is that the numerical scheme is per definition conservative. This means the conservation of mass and momentum are guaranteed by the numerical scheme. In the finite volume configuration volumetric average values in each control volume are used. Furthermore it is assumed that the average values coincide with the values at the center of the control volume.

A staggered grid is used, where the scalar variables are stored at the cell centers of the control volumes and the velocity components are located at the cell faces. For a better understanding the staggered control volumes for the pressure and velocities are shown in figure 3.2. For simplicity a two dimensional configuration of cartesian square control volumes with constant mesh size is shown. The control volume for the pressure, centered at the $(i, j)$ node is presented as grey-shaded area in figure 3.2(a). The locations of the edges are identified by half-indices $(i \pm 1/2, j \pm 1/2)$. The velocity components are solved using different control volumes, as displayed in figure 3.2(b). Using such staggered grids leads to a very robust numerical method which can be - despite of the complex looking indexing - relatively easy to implement, (Prosperetti and Tryggvason, 2007).

In the next sections the control volumes for the scalar variables ($p$, $c$, $\rho$, $\mu$) are always indicated by the subscript $p$, as $V_p$ represents the control volume for the $p$. The control volumes for the velocity components are indicated by subscripts $u$, $v$ and $w$. In the framework of the presently used volume of fluid (VOF) method, the color function at control volume $p$, is defined as a volume concentration

$$c = \frac{\text{Volume of fluid 1}}{\text{Volume of the control volume}} \ . \tag{3.5}$$

An introduction to VOF methods is given in chapter 4.
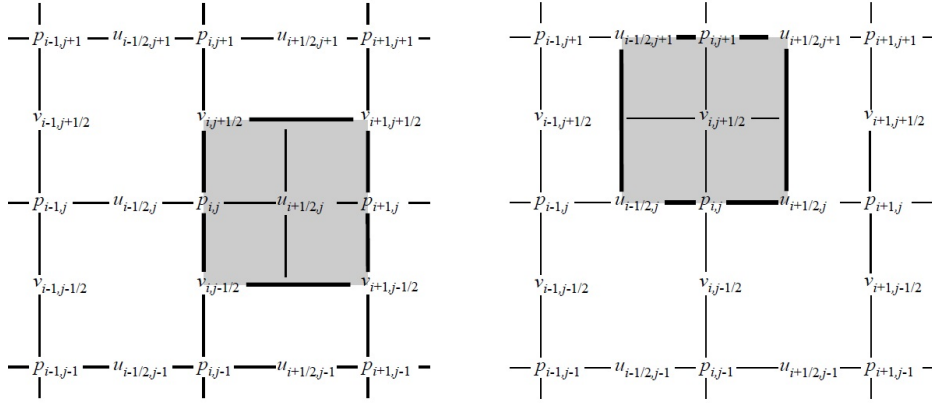
### Transport equation for the color function

In the derivation of the numerical approximation for the advection term of the color function equation (2.16c), its volume integral over the control volume $V_p$ is rewritten as a surface integral using Gauss' theorem

$$A_c = -\frac{1}{V_p} \int_{V_p} \nabla \cdot (c\mathbf{u}) \, dV = -\frac{1}{V_p} \int_{S_p} c\mathbf{u} \cdot \mathbf{n} \, dS = -\frac{1}{V_p} \sum_{f_p=1}^{d} \int_{S_{f_p}} c\mathbf{u} \cdot \mathbf{n} \, dS, \tag{3.6}$$
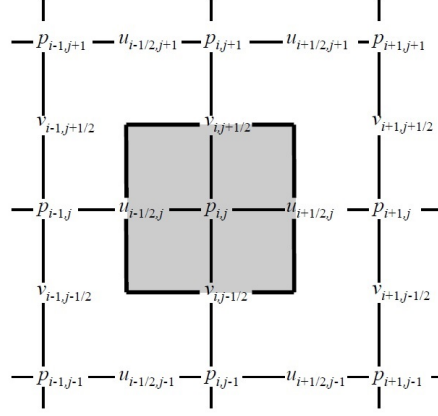
(a) The pressure control volume, centered at the $(i, j)$ node.



(b) The $u$-velocity and $v$-velocity control volume, centered at the $(i + 1/2, j)$ and $(i, j + 1/2)$ node.

Figure 3.2: Control volumes for pressure and velocity components on a staggered two-dimensional grid. Figures from Prosperetti and Tryggvason (2007).

where the faces of a control volume $p$ are denoted by $f_p$, and $d$ is the total number of faces of the control volume $p$. This expression is the exact representation of the average advection term at control volume $p$. The surface integral is approximated using the midpoint rule, where the integral is approximated as the integrand at the cell face center multiplied by the cell face area. This approximation of the integral is of second-order accuracy and it reads

$$\sum_{f_p=1}^{d} \int_{S_{f_p}} c\mathbf{u} \cdot \mathbf{n} \, dS \approx \sum_{f_p=1}^{d} c_{f_p} \mathbf{A}_{f_p} \cdot \mathbf{u}_{f_p} = \sum_{f_p=1}^{d} c_{f_p} F_{f_p}, \tag{3.7}$$

where $c_{f_p}$ and $\mathbf{u}_{f_p}$ represent the values at the center of the cell face. $\mathbf{A}_{f_p}$ is the face area vector, and $F_{f_p} := \mathbf{A}_{f_p} \cdot \mathbf{u}_{f_p}$ is the volumetric flux at the cell face for the control

volume $p$.

The resulting discretized formulation of the advection term at control volume $p$ reads

$$A_c^n := -\frac{1}{V_p} \sum_{f_p=1}^{k} c_{f_p}^n F_{f_p}^n. \tag{3.8}$$

The main problem of this approximation lies in the determination of the cell face value of the scalar $c_{f_p}$, which is localized at the cell centers and not at the cell faces. A simple linear interpolation would lead to over- and undershoots, which implies that the color function would have values less than zero or greater than one. Many methods have been developed to deal with this problem. In this present work two different schemes are used for the numerical experiments to determine the cell face values $c_{f_p}$:

- *Koren flux limiter scheme*: It falls into the group of total variation diminishing (TVD) schemes and uses the concept of a flux limiter function. Further explanations are given in section 4.3.1.

- *High Resolution Interface Capturing (HRIC) scheme*: It is a scheme derived from a normalized variable approach. Further explanations are given in section 4.3.2.

## Momentum equation

The momentum equations carry advection, diffusion and surface tension terms, which have to be numerically approximated. The following formulations are shown for an arbitrary component denoted by $\Phi$, which can represent $u, v, w$ without any loss of generality.

For the numerical approximation of the advection term into the direction of $\Phi$ the same approaches as for the advection term of the color function equation are used (Gauss' theorem, midpoint rule), such that

$$A_\Phi^n := -\frac{1}{V_\Phi} \sum_{f_\Phi=1}^{k} \rho_{f_\Phi}^n \Phi_{f_\Phi}^n F_{f_\Phi}^n.$$

All quantities which are unknown at the centers of the faces of the control volume $V_\Phi$, are approximated by linear interpolation.

The diffusion term involves second-order partial derivatives generally written as

$$\frac{\partial}{\partial d_i} \left( \mu \frac{\partial \Phi}{\partial d_j} \right), \tag{3.9}$$

where $d_i$ and $d_j$ can be any direction. Just the approximation of the general term (3.9) is considered without any loss of generality. Integration of the general term (3.9) over an arbitrary control volume $V$ gives

$$\int_V \frac{\partial}{\partial d_i} \left( \mu \frac{\partial \Phi}{\partial d_j} \right) dV = \mu_{i+} A_{i+} \left( \frac{\partial \Phi}{\partial d_j} \right)_{i+} - \mu_{i-} A_{i-} \left( \frac{\partial \Phi}{\partial d_j} \right)_{i-},$$

where $i+$ and $i-$ refer to the values at the boundary faces with respect to the direction $d_i$ with the cell face areas $A_{i+}$ and $A_{i-}$. The partial derivatives into the direction $d_j$ are approximated by a central difference scheme.

The surface tension terms involves the gradient of the color function and the curvature, which is obtained as the divergence of the normalized gradient of $c$. The gradient of the color function is approximated using a first-order forward difference scheme and is denoted here by $\nabla_\Phi$. The curvature $\kappa_p$, evaluated at the control volume $p$, is directly calculated from the gradient of the color function $c$ using again Gauss' theorem

$$\kappa_p = - \left[ \nabla \cdot \left( \frac{\nabla c}{\|\nabla c\|} \right) \right]_p = -\frac{1}{V_p} \sum_{f_p=1}^{n} \mathbf{A}_{f_p} \cdot \left( \frac{[\nabla c]_{f_p}}{[\|\nabla c\|]_{f_p}} \right),$$

where the gradients $[\nabla c]_{f_p}$ refer to the cell faces. The discretization of the surface tension term for the $\Phi$ component finally reads

$$f_{\sigma,\Phi}^n := -\sigma \kappa_\Phi \nabla_\Phi c^n,$$

where $\kappa_\Phi$ is approximated by linear interpolation from the values at the cell centers $\kappa_p$.

## 3.4 Boundary conditions

Inflow, lateral and outflow boundary conditions for all unknown variables $\mathbf{u}$, $p$ and $c$ must be imposed. For the present case of a free jet flow the outflow boundary requires special attention to ensure numerical stability by eliminating undesirable upstream effects as far as possible.

### Inflow boundary condition

The inflow boundary contains the orifice of the nozzle, where the liquid-phase fluid 1 is injected with a given velocity $\mathbf{u}_{inl}$ into the domain. The remaining part of the inflow boundary $\Gamma_{in}$ is assumed as occupied by the gaseous ambient fluid 2 at rest. For the pressure a homogeneous von Neumann boundary condition is applied. Summing up the following boundary conditions are imposed at the inflow:

$$\mathbf{u}(\mathbf{x}, t) = \begin{cases} \mathbf{u}_{inl}(\mathbf{x}, t), & \text{for } \theta \leq \theta_{inl}, \ \mathbf{x} \in \Gamma_{in} \\ \mathbf{0}, & \text{for } \theta > \theta_{inl}, \ \mathbf{x} \in \Gamma_{in} \end{cases},$$

$$c(\mathbf{x}, t) = \begin{cases} 1, & \text{for } \theta \leq \theta_{inl}, \ \mathbf{x} \in \Gamma_{in} \\ 0, & \text{for } \theta > \theta_{inl}, \ \mathbf{x} \in \Gamma_{in} \end{cases},$$

$$\frac{\partial p(\mathbf{x}, t)}{\partial n} = 0 \quad \text{for } \mathbf{x} \in \Gamma_{in}.$$

$\theta \leq \theta_{inl}$ refers to the conditions inside the orifice and $\theta > \theta_{inl}$ for the conditions outside. For the von Neumann boundary condition a first-order forward difference scheme is used here.

## Lateral boundary condition

Without any loss of generality the pressure is taken to be zero on the lateral boundary $\Gamma_{lat}$. For the velocity a homogeneous von Neumann boundary condition is used and just the presence of fluid 2 is assumed. In summary the lateral boundary condition can be stated as follows:

$$\frac{\partial \mathbf{u}(\mathbf{x}, t)}{\partial n} = 0 \quad \text{for } \mathbf{x} \in \Gamma_{lat},$$

$$c(\mathbf{x}, t) = 0 \quad \text{for } \mathbf{x} \in \Gamma_{lat},$$

$$p(\mathbf{x}, t) = 0 \quad \text{for } \mathbf{x} \in \Gamma_{lat}.$$

For the von Neumann boundary condition a first-order backward difference scheme is used here.

## Outflow boundary condition

The outflow boundary condition $\Gamma_{out}$ is a bit more tricky to handle. Because of the elliptic character of the equations the outflow boundary conditions can influence the flow domain. If large vortical structures appear they are leading to extended regions with reversed flow. If these structures reach the outflow boundary and a von Neumann boundary condition is used significant reversed flow can arise at the boundary, which can finally lead to numerical instabilities, (Fröhlich, 2006). To avoid this problem the widely used convective boundary condition, written as

$$\frac{\partial \mathbf{u}}{\partial t} + \overline{U}_{out} \frac{\partial \mathbf{u}}{\partial n} = 0, \tag{3.10}$$

is applied. The convective boundary condition enforces a predominantly outwards directed motion using an average advection velocity $\overline{U}_{out}$ instead of the local values. This implies that a different partial differential equation is solved at the outflow boundary as compared to the in the inner domain. It is in contrast a hyperbolic equation and the formulation (3.10) has, for positive $\overline{U}_{out}$, a real outward directed characteristic to prevent reversed flow. More detailed explanations for outflow boundary conditions can be found in Fröhlich (2006). For the pressure and for the color function a homogeneous von Neumann boundary condition is applied. Summing up the following boundary conditions are obtained at the outflow:

$$\frac{\partial \mathbf{u}(\mathbf{x}, t)}{\partial t} + \overline{U}_{out}(\mathbf{x}) \frac{\partial \mathbf{u}(\mathbf{x}, t)}{\partial n} = 0 \quad \text{for } \mathbf{x} \in \Gamma_{out}, \ \overline{U}_{out}(\mathbf{x}) > 0,$$

$$\frac{\partial p(\mathbf{x}, t)}{\partial n} = 0 \quad \text{for } \mathbf{x} \in \Gamma_{out},$$

$$\frac{\partial c(\mathbf{x}, t)}{\partial n} = 0 \quad \text{for } \mathbf{x} \in \Gamma_{out}.$$

All normal derivatives and the time derivative are approximated by a first-order backward difference scheme.

# 4 Volume Of Fluid (VOF) Methods

Before explaining the basic ideas of the VOF method in more detail and working out the main differences between the two presently applied interface capturing schemes, the HRIC and the Koren flux limiter scheme, an introduction and literature review on the fundamental concepts for the numerical simulation of multi-phase flow are given.

## 4.1 Introduction

There have been developed various methods for the challenging problem of interface propagation in multiphase flow calculations. Basically, they can be classified into two groups, (Ferziger and Peric, 1996):

- Interface Tracking Methods (ITM)
- Interface Capturing Methods (ICM)

In Figure 4.1 the main differences between the two methods are exemplarily shown.
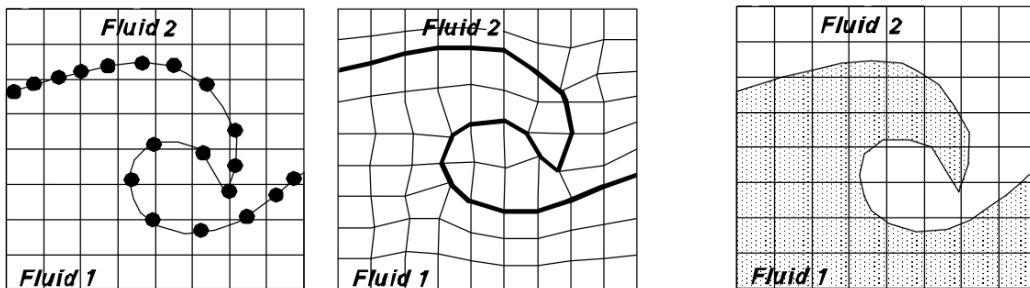


(a) ITM:Marker particles on the interface and an interface attached to a mesh surface.

(b) ICM:Fluids are marked by massless particles or a volume fraction function.

Figure 4.1: ITM and ICM in comparison. Figures from Ubbink (1997).

*Interface Tracking Methods* define a sharp interface, whose motion is followed. These methods explicitly track the interface either by marking it with special marker points (Daly, 1969), or by attaching it to a mesh surface which is forced to move with the interface (Glimm et al., 1986). The advantage of ITM is that the position of the interface is exactly known throughout the calculation, and no unphysical smearing of the interface occurs, as it is typically observed with the ICM. On the other hand, if the

interface is attached to a mesh surface, some problems may arise. Large distortions of
the mesh can be met, if the interface is subjected to deformations. As shown by Ra-
maswamy and Kawahara (1987) in numerical experiments on the collapse of a liquid
column, such large deformations can occur already at the beginning of the computa-
tion. To maintain a well defined mesh it would therefore be necessary to interpolate
a new mesh, which leads to additional computational effort. Another disadvantage is
that changes in the topology, like in wave breaking or droplet formation, are hard to
capture with ITM.

*Interface Capturing Methods* solve the equations of motion in the whole domain on
a fixed grid and the fluids on either side of the interface are marked. Two main
representations of interface capturing methods are marker and cell (MAC) methods
and volume of fluid (VOF) methods, which are explained in more detail in the next
sections.

## Marker And Cell (MAC) Methods

Instead of defining an interface directly, one can also work with the regions occupied by
the considered fluids. The marker and cell method, or MAC method, was introduced
by Harlow and Welch (1965) for free surface flows. In the MAC method massless
marker particles are distributed over the volume to determine the interface with each
particle specified to move with the fluid velocity at its location. The interface lies
between regions with and without marker particles. A cell without marker particles
is considered to be empty. More precisely, a mesh cell containing markers, but having
a neighboring cell with no markers, is defined as containing an interface. A sketch of
a typical marker and cell mesh layout can be seen in figure 4.2. The actual location
of the interface must be determined by some additional computation based on the
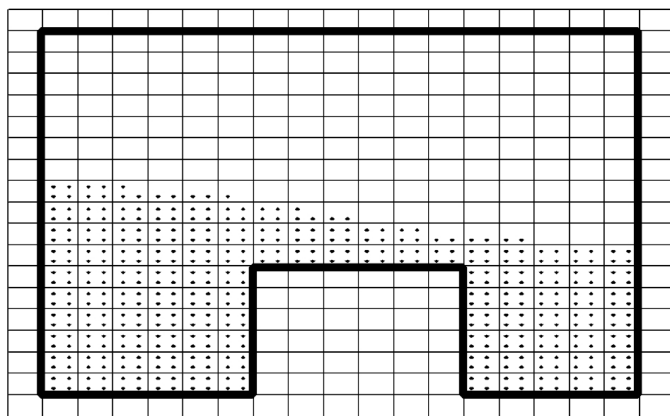distribution of markers within the cell.



Figure 4.2: Sketch of a typical marker and cell mesh layout. Figure from Ubbink
(1997).

The MAC method was extended by Daly (1967), to allow the computation of two-fluid phenomena. At the beginning the marker particles are classified according to the fluid they represent and this classification holds for the whole flow calculation. A mesh cell with marker particles from both fluids contains the interface. The approach is also applicable in three-dimensional computations. The deficit of ITM to capture topological changes is overcome by MAC methods. While MAC methods can describe these changes in topology, it suffers from a significant increase in computational effort. Especially in three-dimensional calculations the movement of a large amount of marker particles can cause intolerable computer costs.

The **Volume of Fluid method**, or VOF method, was introduced by Hirt and Nichols (1981) for free surface flows. Like in MAC methods a fixed grid is used in the whole domain. To reduce the computational effort a scalar color function $c$, or in the literature sometimes called indicator or marker function, is introduced instead of discrete marker particles. The color function $c$, in the framework of VOF methods, is defined as

$$c = \frac{\text{Volume of fluid 1}}{\text{Volume of the control volume}} \; . \tag{4.1}$$

With the above definition three possible cases can arise:

- $c = 1$, control volume is totally filled with fluid 1.
- $c = 0$, control volume is totally filled with fluid 2.
- $c \in (0, 1)$, control volume is partially filled.

In Figure 4.3 the values of the color function $c$ for a smooth circular portion of fluid 1 specified on a square grid can be seen.
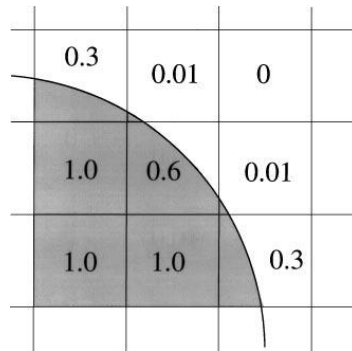


Figure 4.3: Representation of the volume fraction for a smooth circular portion of fluid on a square grid. Figure from Scardovelli and Zaleski (1999).

As mentioned earlier the color function $c$ obeys the transport equation

$$\frac{\partial c}{\partial t} + \nabla \cdot (c\mathbf{u}) = 0 \; . \tag{4.2}$$

The major difficulties connected with discretization of the transport equation of the color function are:

- *Boundedness of the color function*: The color function $c$ is bounded below by zero and above by one. No unphysical over- and undershoots should appear.

- *Sharpness of the interface*: The sharpness of the interface should be maintained. Numerical diffusion of the step-like interface profile should be avoided.

Many methods have been developed to satisfy these two constraints. Higher-order schemes often not fulfill the boundedness but can maintain the step-like interface profile. Lower order schemes are bounded but, lead typically to a smearing of the interface.

VOF methods can be categorized into two groups, depending on how they deal with the color function equation (4.2):

- *Interface reconstruction methods.*

- *High resolution schemes.*

## 4.2 Interface reconstruction methods

Interface reconstruction methods use the idea of geometric interface reconstruction. The transport equation of color function (4.2) is not directly discretized in the sense of a partial differential equation. Instead geometrical considerations are used to model adequately the convection of the color function. Usually these methods consist of two steps. First, a reconstruction step is carried out to determine the shape of the interface. Second, a propagation step is performed to obtain the new distribution of the color function.
Different interface reconstruction methods were proposed, and some of the most popular approaches are briefly described below.

*The simple line interface calculation (SLIC) method*, see Noh and Woodward (1976), has been developed to deal with two dimensional interfacial flow. The interface in each control volume is reconstructed as a line parallel to one of the coordinate axes. The reconstruction and propagations is done separately in each coordinate direction, which implies that only cell neighbours in the considered coordinate direction are used to determine the interface. This procedure is called operator splitting.

*Piecewise linear interface calculation (PLIC) method*, see Youngs (1982), uses lines of any orientation to approximate the interface in a control volume. Continuity across the cell faces is not required. Also for PLIC methods an operator splitting procedure can be used. After each propagation step into one direction the interface has to be reconstructed.

|  |  |  |
|---|---|---|
| 0 | 0 | 0 |
| 0 | 0.3 | 0.5 |
| 0.5 | 0.9 | 1 |

**(a)** True Interface      **(b)** Volume Fractions

**(c)** SLIC Approximation      **(d)** Piecewise Linear
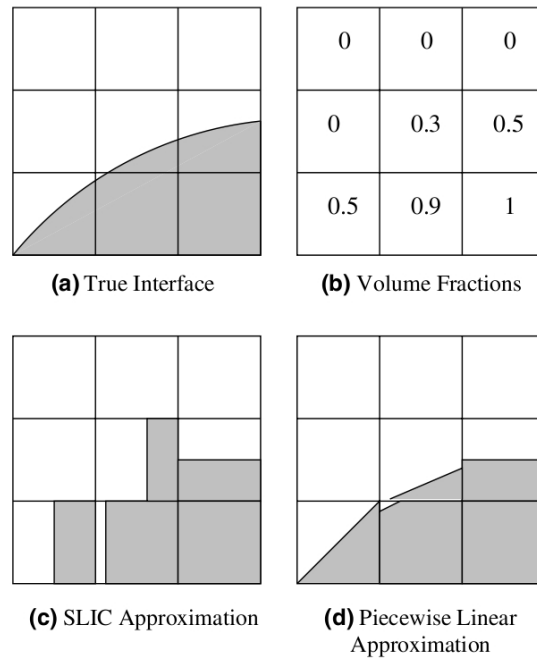Approximation

Figure 4.4: An approximation to the interface is produced using an interface reconstruction method such as SLIC or a more general piecewise linear approximation. Figure from Pilliod and Puckett (2004).

In figure 4.4 the differences between the SLIC method and the PLIC method can bee seen.

The advantage of interface reconstruction methods is their natural way to preserve the sharpness of the interface. They were developed and tested for two-dimensional problems. Complex expressions occur, especially in three dimensions, and an efficient implementation is a hard task, see López and Hernández (2008). The difficulty of the interface reconstruction becomes apparent in figure 4.5. The color function is represented as shaded squares of a size proportional to the local volume fraction. In the case on the left hand side shown the segment of a circle reconstruction is relatively easy to accomplish. In complex situations, like in drop collision, reconstruction is a much harder task. The difficulty in the reconstruction of the interface becomes significantly higher when dealing with three-dimensional flow problems, where the numerical resolution requires often unacceptable large computational resources. Other methods without an interface reconstruction step are therefore used and preferred in three dimensions. A popular alternative are high resolution schemes.

(a) A well-behaved distribution of the color function, corresponding to a segment of a circle.

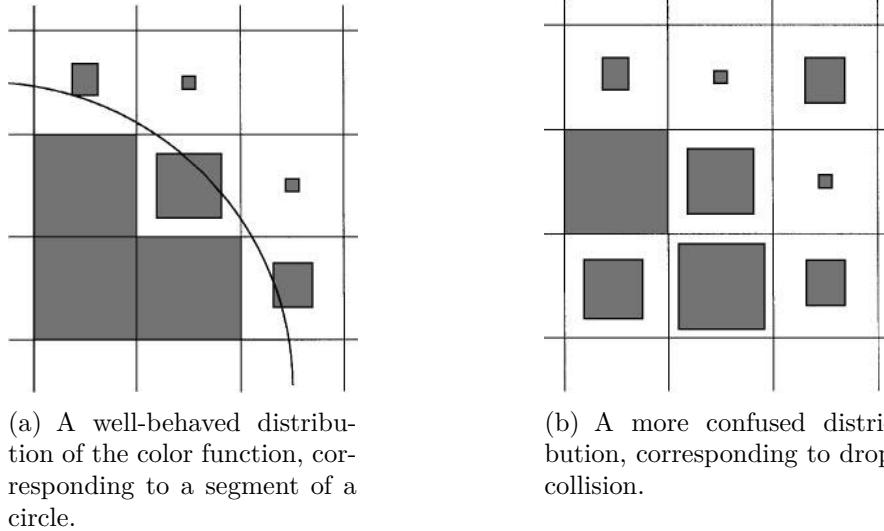(b) A more confused distribution, corresponding to drop collision.

Figure 4.5: Difficulty of the interface reconstruction. The color function is presented as shaded squares of a size proportional to the volume fraction. Figures from Scardovelli and Zaleski (1999).

## 4.3 High resolution schemes

Another approach is to discretize the color function equation (4.2) directly using a higher order differencing scheme. The term "high resolution" scheme, introduced by Harten (1983), represents a class of conservative schemes which produce solutions free from spurious oscillations and with high accuracy especially near discontinuities met in compressible flows like shocks, or contact surfaces. As such, the class of high resolution schemes also represent good candidates for the numerical solution of the color function equation.

The color function equation is usually solved with a finite volume approach to ensure a conservative scheme. Using a finite volume approach the fluxes of the control volume interfaces have to be calculated. In one dimension the color function equation at constant velocity $u > 0$ reduces to

$$\frac{\partial c}{\partial t} + \frac{\partial (uc)}{\partial x} = 0. \tag{4.3}$$

Using the finite volume approach this equation can be integrated in space over a control volume centered at point $x_i$ from $x_i - \Delta x/2$ to $x_i + \Delta x/2$, assuming a uniform mesh size $\Delta x$. This gives the exact semi-discrete equation

$$\int\limits_{x_{i-1/2}}^{x_{i+1/2}} \frac{\partial c}{\partial t} dx + (F_{i+1/2} - F_{i-1/2}) = 0 \tag{4.4}$$

with the definition $F_{i\pm1/2} := u \cdot c(x_{i\pm1/2}, t)$.

The main problem in defining finite volume discretizations of the convective transport equation (4.3) is the approximation of the fluxes across the cell faces. Using a staggered grid the velocities across the faces are known, while the convected scalars have to be approximated based on their known values at the cell centers. All of the schemes considered here calculate face values using the upwind-biased stencil configuration shown in Figure 4.6. It means that for the calculation of the face value $c_f$ only the
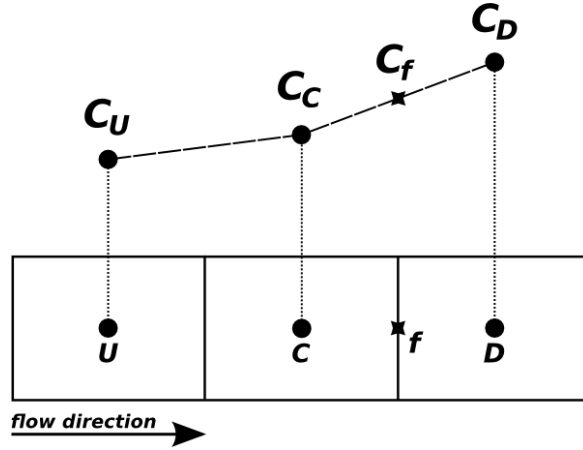


Figure 4.6: Upwind-biased stencil configuration.

values $c_U, c_C$ and $c_D$ are used. This assumption is supported by the fact that the true domain of dependence always upwind. From the various methods which have been proposed to calculate the numerical fluxes two particular high resolution schemes are used in the present calculations, namely, the Koren flux limiter scheme, Koren (1993), based on the flux limiter approach and the high resolution interface capturing (HRIC) scheme Muzaferija et al. (1998), based on the normalized variable diagram (NVD). These two schemes are discussed in more detail in the following sections.

## 4.3.1 High resolution schemes based on flux limiters - Koren flux limiter

The general idea of constructing high resolution schemes using flux limiters is to define the numerical flux $F_f$ in dependence of a low-order numerical flux $F_f^l$ and a high-order numerical flux $F_f^h$. The letter $f$ indicates any face value. The two fluxes $F_f^l$ and $F_f^h$ are combined through a flux limiter function $\gamma$ as follows:

$$F_f(s) = F_f^l + \gamma(s) \ (F_f^h - F_f^l).$$

Therein, $s$ represents the ratio of consecutive gradients of the solution defined by

$$s := \frac{c_D - c_C}{c_C - c_U} \ .$$

Sometimes $s$ is inversely defined, like in the widely cited paper on flux limiters by Sweby (1984).

The flux limiter function $\gamma$ is defined in such a way that it diminishes to zero in regions with extrema or discontinuities, so that the lower-order numerical flux approximation is used. In smooth solution regions the flux limiter $\gamma$ takes a value close to one to give a highly accurate approximation scheme.

The lower-order numerical flux approximation $F_f^l$ ensures boundedness of the solution but introduces numerical diffusion. Flux limiter methods remedy this by adding a limited amount of the antidiffusive flux $(F_f^h - F_f^l)$. So the flux limiter function $\gamma$ is constructed in such a way that the limited antidiffusive flux $(F_f^h - F_f^l)$ is maximized under the constraint that the numerical scheme does not produce spurious oscillations.

### $\beta$-scheme formulation

Following the concept Leer (1985) many well-established linear higher-order schemes can be classified as $\beta-$schemes. This concept is adopted for the derivation of the presently used flux limiter proposed by Koren (1993) as well. Using the $\beta-$scheme formulation the face value needed for the approximation of the fluxes is generally written as:

$$c_f = c_C + \left[ \frac{1+\beta}{4}(c_D - c_C) + \frac{1-\beta}{4}(c_C - c_U) \right], \qquad \beta \in [-1, 1].$$

For $\beta = 1$, one gets the central difference scheme (CDS), where the face value is calculated by linear interpolation from the two adjoining nodal values. For $\beta = -1$ the linear-upwind interpolation (LUI) scheme is obtained (Atias et al., 1977), where the face value is computed form a linear extrapolation of the two upwind nodal values. It is the only fully upwind $\beta$-scheme which is sometimes called second order upwind (SOU) scheme as well. For all other values $\beta \in [-1, 1]$, a dynamic blending is obtained between the CDS scheme and the LUI scheme.

Substituting the $\beta-$representation of $c(x_{i+1/2}, t)$ and $c(x_{i-1/2}, t)$ needed for $F_{i+1/2}$ and $F_{i-1/2}$, into (4.4) respectively, and applying a Taylor-series expansions with a truncation error of order $O(\Delta x^3)$, we get:

$$\frac{\partial c}{\partial t} + u \frac{\partial c}{\partial x} + \frac{1}{24}\Delta x^2 \frac{\partial^3 c}{\partial t \partial x^2} + \frac{\beta - \frac{1}{3}}{4}\Delta x^2 u \frac{\partial^3 c}{\partial x^3} = O(\Delta x^3), \qquad \beta \in [-1, 1].$$

It can be seen that for the steady convection equation any $\beta$-scheme discretization is at least second-order accurate for a sufficiently smooth solution. For the specific value $\beta = \frac{1}{3}$ the interpolation becomes third-order accurate. This was the motivation for Koren to use $\beta = \frac{1}{3}$.

These higher-order linear schemes still can produce unphysical oscillations, in particular in the presence of sharp gradients. This limitation is addressed by Godunov's famous theorem, stating that no linear convection scheme of second-order accuracy or

higher can be monotonic (Waterson and Deconinck, 2007).

This limitation gave the motivation to introduce non-linear schemes which use controlled fluxes to ensure boundedness.

### Flux limiter approach corresponding to the $\beta$-schemes

The flux limiter approach used by Koren follows that of Roe (1987) and it differs from that of Sweby (1984) in that the discretization of the spatial terms is completely separated from the time discretization used. For the higher-order numerical flux $F_f^h$ the LUI interpolation scheme, associated with $\beta = -1$, is used, and for the lower-order numerical flux $F_f^l$ the first-order upwind scheme is applied. This leads to

$$F_f = u\,c_f = F_f^l + \gamma(s)[F_f^h - F_f^l] = u\,c_C + \gamma(s)\left[u\left(\frac{3}{2}c_C - \frac{1}{2}c_U\right) - u\,c_C\right],$$

resulting in a formulation for a constant veloctiy $u > 0$

$$c_f = c_C + \gamma(s)\frac{c_C - c_U}{2}.$$

The flux limiter function written in terms of a $\beta$-scheme reads, (Waterson and Deconinck, 2007):

$$\gamma(s) = \frac{1+\beta}{2}s + \frac{1-\beta}{2}.$$

For $\gamma(s) = s$ the CDS scheme is obtained.

### Boundedness criteria - TVD concept

As mentioned above boundedness criteria have to be imposed to ensure an oscillation-free numerical solution. One approach used by Koren for his flux limiter derivation is the total variation diminishing (TVD) concept. The TVD concept introduced by Harten (1983) guarantee oscillation free numerical solutions for explicit conservative numerical schemes.

An explicit conservative numerical scheme is said to be TVD, if

$$TV(c^{n+1}) \leq TV(c^n),\ \forall n,\ \text{where}\ TV(c^n) := \sum_i |c_i^n - c_{i-1}^n|.$$

The TVD concept was translated by Sweby (1984) into a set of conditions imposed on the flux limiter functions. The constraints for a flux limiter function to ensure a TVD behavior read:

$$0 \leq \gamma(s) \leq \min(2s, 2), \quad \text{for } s \geq 0,$$
$$\gamma(s) = 0, \quad \text{for } s < 0.$$

It should be noted that the second constraint does not arise directly from the TVD requirement but is added as a safe treatment for extrema, (Waterson and Deconinck, 2007).

**Koren flux limiter**

Koren followed the TVD related considerations to define a non-linear scheme based on the flux limiter approach corresponding to $\beta = \frac{1}{3}$. The resulting flux limiter reads:

$$\gamma(s) = \max\left(0, \min\left(2s, \min\left(\frac{2}{3}s + \frac{1}{3}, 2\right)\right)\right) \tag{4.5}$$

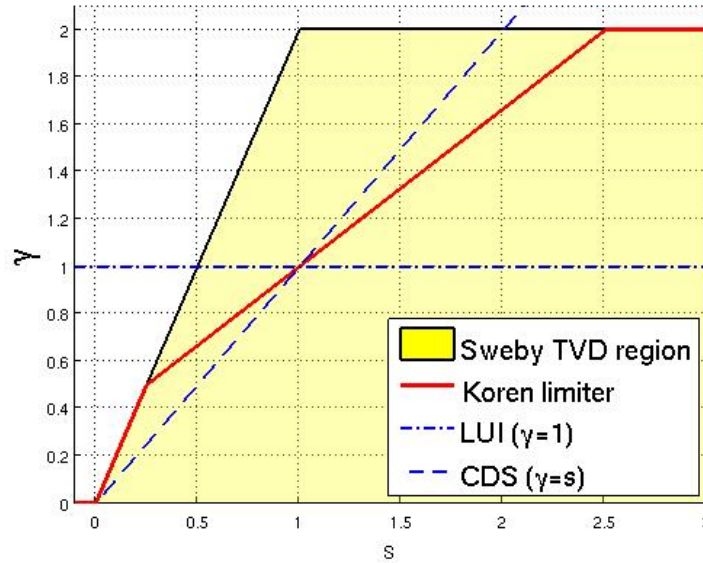In Figure 4.7 the Koren flux limiter is plotted into the Sweby TVD region. The LUI scheme, $\beta = -1$, and the CDS scheme, $\beta = 1$, are shown as well for completeness.



Figure 4.7: Koren flux limiter in the Sweby TVD region.

Sweby found a subdomain, where the TVD schemes are at least second order accurate, (Sweby, 1984). It can be shown that this second-order TVD subdomain is represented by the area, which is covered by the full range of $\beta - schemes$ inside the TVD region (Waterson and Deconinck, 2007). In Figure 4.8 the Koren flux limiter is displayed in the Sweby second-order TVD region.

**Multiple dimensions**

The extension to multiple dimensions of the numerical scheme based on the Koren flux limiter used in the present work is done in a relatively straightforward manner. The one-dimensional case is extended to the three-dimensional case through dimensional splitting, where each flux is calculated separately for each coordinate direction. No theoretically rigorous extension of the TVD criterion to multiple dimensions has yet been made, and so, when applying dimensional splitting such, schemes are technically not TVD. Nevertheless, Koren showed in numerical experiments that the application
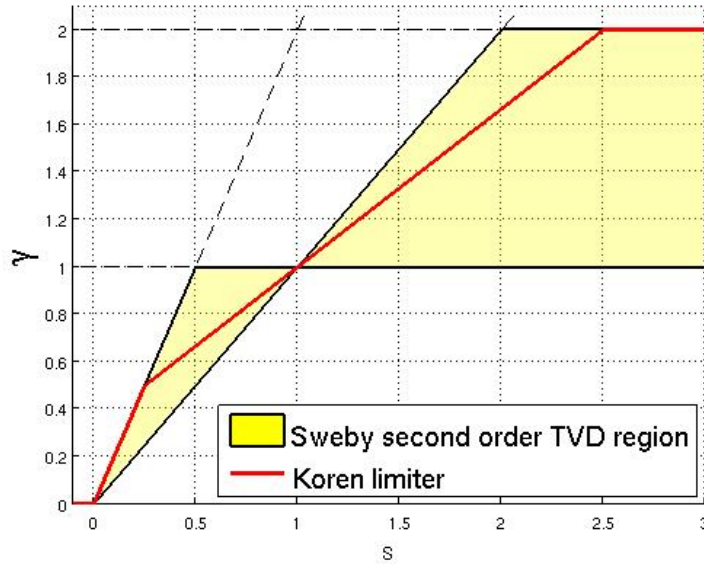
Figure 4.8: Koren flux limiter in the Sweby second order TVD region.

of the simple dimensional splitting did not lead to unsatisfactory results proving his concept as a robust discretization method without any tuning (Koren, 1993).

For the sake of completeness some important flux limiter functions which all lie in the second-order TVD region are listed below as well:

- Superbee: $\gamma(s) = \max[0, \min(2s, 1), \min(s, 2)]$
- MUSCL: $\gamma(s) = \max[0, \min(2s, \frac{s+1}{2}, 2)]$
- Minmod : $\gamma(s) = \max[0, \min(s, 1)]$
- von Albada : $\gamma(s) = \frac{s(s+1)}{s^2+1}$

## 4.3.2 High resolution schemes based on NVD - HRIC scheme

The alternative high resolution scheme for solving the convection equation used in the present calculations is the high resolution interface capturing (HRIC) scheme proposed by Muzaferija et al. (1998). The HRIC scheme is based on the normalized variable diagram (NVD), as mentioned by Leonard (1979). All schemes discussed earlier are based on the stencil configuration shown in figure 4.6, and the cell face value can be written as

$$c_f = f(c_U, c_C, c_D).$$

It appears as advantage to go for a normalized variable formulation, where the normalized face value $\tilde{c}_f$ depends only on one normalized variable to make comparison of the

individual schemes easier. This can be achieved using the normalization introduced by Leonard (1979), written as

$$\tilde{c} = \frac{c - c_U}{c_D - c_U},$$

so that the interpolation for $c_f = f(c_U, c_C, c_D)$ is simplified to

$$\tilde{c} = f(\tilde{c}_C).$$

It can be seen that for $\tilde{c}_f = c_C$ the FOU scheme is obtained, and for $\tilde{c}_f = 1$ follows the first-order downwind (FOD) scheme. All $\beta-$schemes can be expressed as a linear relationship between the normalized face values $\tilde{c}_f$ and $\tilde{c}_C$. Values of $\tilde{c}_C$ being between 0 and 1 indicate monotonic variation in the solution, while values lying outside this interval indicate the presence of an extremum.

**Boundedness criteria**

The most widely applied boundedness criterion using the NVD is Gaskell and Lau's convection-boundedness criterion (GL-CBC), (Gaskell and Lau, 1988). For the derivation of GL-CBC the one-dimensional steady convection diffusion equation was discretized using a finite volume approach, and restrictions on the cell face values were made under physical considerations to achieve a bounded numerical solution. Gaskell and Lau's two main requirements on a numerical scheme to ensure computed boundedness are convective stability (essentially enforcing an upwind bias) and interpolative boundedness (the face value must be bounded by the upwind and downwind centered control volume values). The GL-CBC states that a continues function or a piecewise continues function $\tilde{c}_f = f(\tilde{c}_C)$ yields a bounded finite difference approximation, if

$$
\begin{aligned}
&\tilde{c}_f = \tilde{c}_C, && \text{for } \tilde{c}_C \leq 0 \text{ and } \tilde{c}_C \geq 1 \\
&\tilde{c}_C \leq \tilde{c}_f \leq \tilde{c}_D, && \text{for } 0 < \tilde{c}_C < 1.
\end{aligned}
$$

The GL-CBC can be seen graphically represented by a certain region in the NVD, shown in Figure 4.9, where different linear schemes are plotted as well.
The GL-CBC and the associated region in the NVD have long been accepted as both a sufficient and necessary condition for a scheme to provide boundedness (Yu et al. (2001), Darvish (1993), Gaskell and Lau (1988)). However, it has been demonstrated that this is not true. In Yu et al. (2001) it is shown that the GL-CBC is just a sufficient condition for boundedness, and a new CBC was proposed. It was shown that schemes satisfying the following constraints are also bounded:

$$
\begin{aligned}
&\tilde{c}_C \leq \tilde{c}_f \leq \frac{\tilde{c}_C}{2}, && \text{for } \tilde{c}_C \leq 0, \\
&\tilde{c}_C \leq \tilde{c}_f \leq \frac{\tilde{c}_C + 1}{2}, && \text{for } 0 \leq \tilde{c}_C \leq 1, \\
&\frac{\tilde{c}_C + 1}{2} \leq \tilde{c}_f \leq \tilde{c}_C, && \text{for } \tilde{c}_C \geq 1.
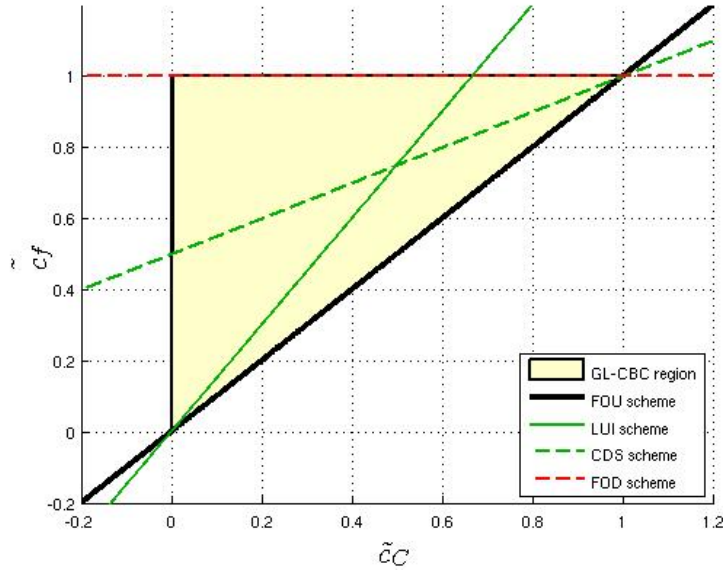\end{aligned}
$$

Figure 4.9: NVD with the GL-CBC region and some linear schemes.

These new constraints is called the extended boundedness criterion (ECBC). In follow-up studies it is shown that the GL-CBC and the ECBC represent two limiting cases of the general convective boundedness criterion (GCBC) proposed by Wei et al. (2007).

### High Resolution Interface Capturing (HRIC) Scheme

The HRIC scheme introduced by Muzaferija et al. (1998) essentially involves three steps.

*1.) GL-CBC based calculation of $\tilde{c}_f$*
The normalized cell face value is estimated from a scheme which continuously connects the FOU and FOD schemes in the NVD. Accordingly the cell face value is computed from the following expression:

$$\tilde{c}_f = \begin{cases} \tilde{c}_C, & \text{for } \tilde{c}_C \leq 0, \\ \tilde{2}c_C, & \text{for } 0 < \tilde{c}_C < 0.5, \\ 1, & \text{for } 0.5 \leq \tilde{c}_C \leq 1, \\ \tilde{c}_C, & \text{for } \tilde{c}_C > 1. \end{cases}$$

Figure 4.11 shows a graphical interpretation of the scheme in NVD.

*2.) Consideration of the orientation of the interface*
Downwind discretization may cause an alignment of the interface with the computational grid, (Ubbink, 1997). This implies that the direct use of the value of $\tilde{c}_f$ causes

wrinkles in the interface, if the flow is parallel to the interface. To avoid this problem, the discretization has to account for the angle $\theta$ between the unit normal vector on the interface and the normal vector on the cell face $\hat{\mathbf{d}}$, as shown in Figure 4.10. As
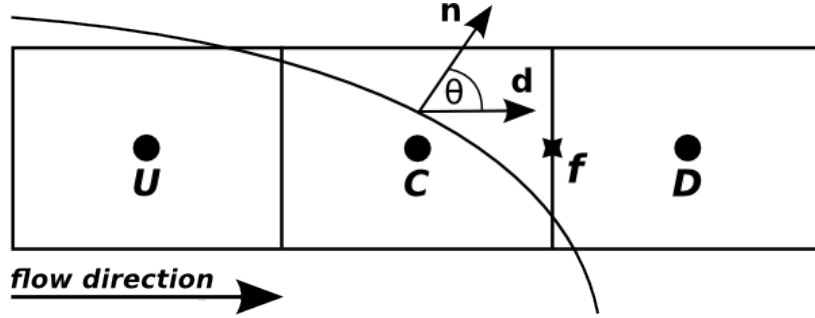


Figure 4.10: Definition of the unit normal vector on the interface $\hat{\mathbf{n}} := \frac{\nabla c}{\|\nabla c\|}$ and the unit normal vector on the cell face $\hat{\mathbf{d}}$.

mentioned earlier the unit normal vector on the interface is defined by the gradient of the color function, written as

$$\hat{\mathbf{n}} := \frac{\nabla c}{\|\nabla c\|}.$$

The face value $\tilde{c}_f$ is then corrected according to the following expression:

$$\tilde{c}_f^\star = \tilde{c}_f \sqrt{|\cos\theta|} + \tilde{c}_C(1 - \sqrt{|cos\theta|})$$

The term $\cos\theta = \hat{\mathbf{n}} \cdot \hat{\mathbf{d}}$ approaches one, if the angle $\theta$ becomes very small and, it approaches zero, if the angle $\theta$ is closed to $\pi/2$.

*3.) Consideration of the local Courant number*
If the local Courant number

$$Co = \frac{\mathbf{u}_f \cdot \hat{\mathbf{n}}\, S_f \Delta t}{V_C},$$

where $\mathbf{u}_f$ is the current velocity at the cell face, $S_f$ is the area of the cell face, and $V_C$ is the volume of the control volume, is too large, explicit discretization schemes of the color function equation may cause stability problems. To prevent this, the HRIC discretization also takes into account of the Courant number according to the following expression:

$$\tilde{c}_f^{\star\star} = \begin{cases} \tilde{c}_f^\star, & \text{for } Co < 0.3, \\ \tilde{c}_C + (\tilde{c}_f^\star - \tilde{c}_C)\frac{0.7-Co}{0.7-0.3}, & \text{for } 0.3 \le Co \le 0.7, \\ \tilde{c}_C, & \text{for } Co > 0.7. \end{cases} \tag{4.6}$$

Finally, the cell face value $c_f^{HRIC}$ is computed as follows:

$$c_f^{HRIC} = \zeta c_C + (1 - \zeta)c_D$$

with the blending factor $\zeta$ defined as:

$$\zeta = \frac{(1 - \tilde{c}_f^{\star\star})(c_D - c_U)}{c_D - c_C}$$

For multiple dimensions the HRIC scheme is extended in the same way as the Koren flux limiter scheme applying the algorithm separately into each direction.

## 4.4 Comparison of the Koren flux limiter scheme and HRIC scheme

For a meaningful comparison of the two schemes the Koren flux limiter function is also displayed in the NVD. We recall the general flux limiter formulation for a constant velocity $u > 0$ in the one-dimensional case is written as

$$c_f = c_C + \gamma(s)\frac{c_C - c_U}{2},$$

Rewritten in normalized variables this expression becomes

$$\tilde{c}_f = \tilde{c}_C + \gamma(s)\frac{\tilde{c}_C}{2}.$$

In Figure 4.11 the $\tilde{c}_f-$ values obtained from the Koren flux limiter scheme and from equation (4.6) in the HRIC scheme neglecting the two correction steps are drawn in the NVD for the one-dimensional case. The TVD region is shown, as well. It can be
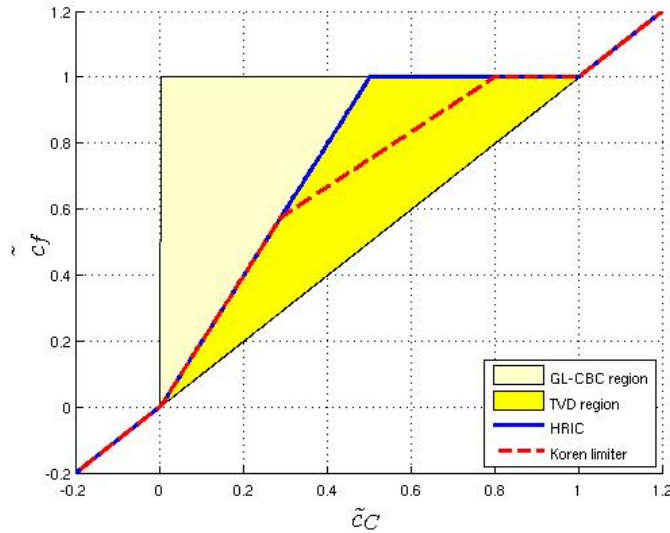


Figure 4.11: The NVD for Koren flux limiter scheme and the HRIC scheme.

observed that the Koren flux limiter scheme and the HRIC scheme are quite similar. First both, are following the left border of the TVD region. At $\tilde{c}_C = 0.285$ the Koren limiter changes its gradient taking a lower path. They intersect each other again at $\tilde{c}_C = 0.8$ and continue on top of each other.

It can be concluded that the HRIC scheme has a bit more compressive nature, than the Koren flux limiter scheme because of the faster transition to the FOD scheme, whose compressive nature is well known, (Muzaferija et al., 1998). This conclusion can be easily verified by a simple one-dimensional test case. In this test case the finite volume approximation (4.4) is solved using a step function defiend by

$$c_0(x) := \begin{cases} 1, & \text{for } x < a, \\ 0, & \text{if } x \geq a, \end{cases}$$

as initial condition. The integration in time is done using a simple Euler-forward discretization. The computational domain extends within the range $x \in [0, 2]$. The initial position of the step is $a = 0.5$, the velocity is set to $u = 0.1 = const$. The time increments and the mesh size are $\Delta t = 0.1$ and $\Delta x = 0.05$, respectively, which results in a Courant number $Co = 0.2$. The solution obtained after $t = 5$ is shown in Figure 4.12. The HRIC scheme gives evidently a better approximation of the exact
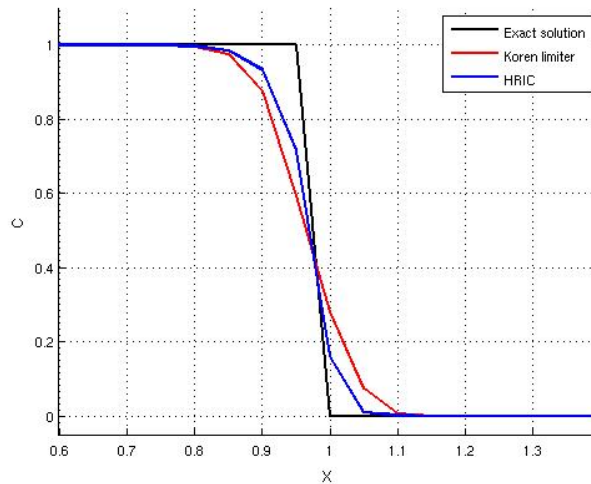


Figure 4.12: Comparison of Koren flux limiter scheme and HRIC scheme for the one dimensional test case.

solution than the Koren flux limiter scheme. Due to its more compressive nature the HRIC scheme appears to be better suited to maintain sharp gradients. As for the application in VOF methods dealing with two-phase flows, where the evolution of a step-like colour function has to be numerically captured without unacceptably strong smearing of the gradients, the HRIC scheme is expected to be superior to the Koren flux limiter scheme.

# 5 Disintegration Theory of Jets

The present work considers the disintegration of liquid free jets surrounded by a gas with much lower density, which may be essentially driven by two particular mechanisms:

- Rayleigh instability (Rayleigh, 1878),

- Kinematic travelling time effects (Meier et al., 1992).

The classical theory of Lord Rayleigh (Rayleigh, 1878) describes the disintegration of liquid jets in the so called capillary breakup regime, where surface tension plays a dominant role. Among destabilizing effects like aerodynamic forces or turbulent fluctuation it has been shown by Meier et al. (1992), that pure kinematic effects can strongly affect the disintegration of a jet as well without considering any surface tension or viscous forces, which is generally termed travelling time theory. In main practical cases both mechanism are active. The theoretical analysis of both mechanisms shall be described in more detail in the next sections.

## 5.1 Rayleigh instability

Lord Rayleigh could show in his famous paper, (Rayleigh, 1878), that so called capillary breakup of a cylindrical liquid column into drops is caused by an unstably increasing transfer of kinetic energy into surface energy and vice versa triggered by a small deformation of the surface. It is precisely this Rayleigh instability, sometimes called Plateau–Rayleigh instability, which is responsible for the pinch-off of thin water jets emerging from kitchen taps. The Rayleigh or capillary breakup represents a particular type of liquid disintegration, whose occurrence can be parametrized based on the Reynolds and the Ohnesorge number, as shown in the nomogram in figure 5.1 due to Ohnesorge (1936). The Ohnesorge number defined as

$$Oh := \frac{\mu}{\sqrt{\rho \sigma L_0}} = \frac{\sqrt{We}}{Re} \tag{5.1}$$

relates the viscous forces to the surface tension forces (Ohnesorge, 1936). It can be expressed in terms of the Weber and Reynolds number. It can be seen that for small Reynolds and Ohnesorge numbers the capillary forces are responsible for jet breakup. The wind-induced breakup is driven by aerodynamic forces on the surface of the liquid. Atomization is generally associated with high jet exit velocities with high overpressures in the nozzle chamber upstream of the orifice.
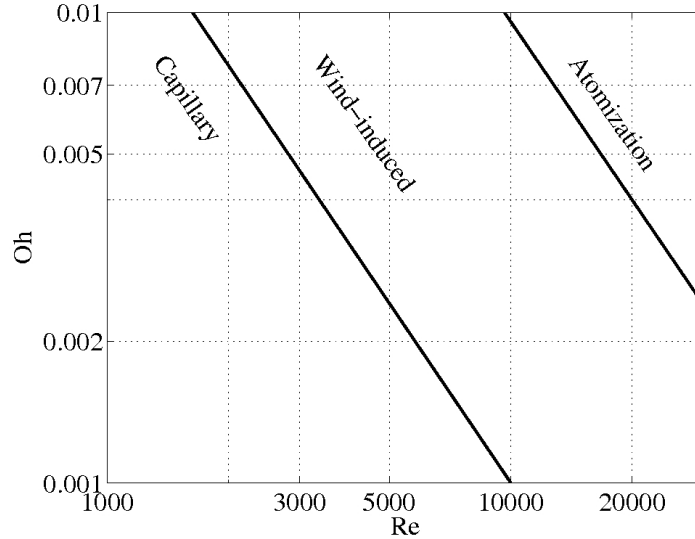
Figure 5.1: Different breakup regimes depending on the Reynolds and Ohnesorge number. (Ohnesorge, 1936).

In this section a theoretical description of this instability, established by Lord Rayleigh, shall be given. For this theoretical analysis the following assumptions are made:

- The liquid is inviscid.
- The jet is of infinite length.
- Only capillary forces are considered.
- The jet just undergoes small deformations.
- The surroundings are evacuated and the gravitational forces are neglected.

The main idea of the analysis is that the sum of the surface energy and the kinetic energy is independent of time,

$$\sum E_{kin} + E_{surf} \neq f(t).$$

An infinitely long quiescent cylindrical liquid column is considered as starting configuration, whose surface is deformed by infinitesimal varicose perturbations on the interface. Assuming a cylindrical coordinate system the instantaneous perturbed radius reads

$$h(\theta, z, t) := h_0 + f(\theta, z, t) = h_0 + \alpha_m(t) \cos(m\theta) \cos(kz), \qquad (5.2)$$

where $k$ is the wave number of the disturbance into the axial direction $z$, $h_0$ the initial radius of the undeformed cylindrical fluid column, $m \in \mathbb{N}$ is the mode of the periodic perturbation into the direction $\theta$, and $\alpha_m(t)$ represents a growth or damping of the disturbance in time in dependence of the the parameter $m$. The wave number $k$ is

connected to a corresponding wave length $\lambda$ by

$$k := \frac{2\pi}{\lambda}. \tag{5.3}$$

From the assumption that the jet just undergoes small deformations it is deduced that $f \ll h_0$. In figure 5.2 the disturbed and undisturbed jet are shown, where $r$ and $z$ denote the radial and axial coordinates, respectively. The volume within one wave
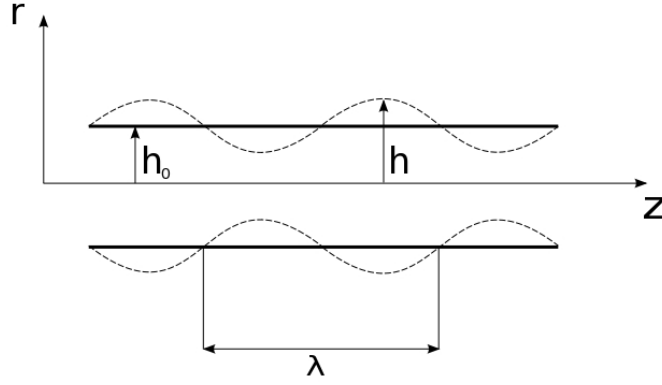


Figure 5.2: Disturbed and undisturbed jet.

length can be calculated as

$$
\begin{aligned}
V &= \int_{r=0}^{h} \int_{z=0}^{\lambda} \int_{\theta=0}^{2\pi} r \; d\theta dz dr \\
&= \frac{1}{2} \int_{z=0}^{\lambda} \int_{\theta=0}^{2\pi} h^2(\theta, z, t) \; d\theta dz \\
&= \frac{1}{2} \int_{z=0}^{\lambda} \int_{\theta=0}^{2\pi} [h_0^2 + 2h_0 \alpha_m \cos(m\theta)\cos(kz) + \alpha_m^2 \cos^2(m\theta)\cos^2(kz)] \; d\theta dz
\end{aligned}
$$

A distinction is made between the cases $m = 0$ and $m \neq 0$, which yields:

$$m \neq 0: \quad V = \lambda(\pi h_0^2 + \frac{\pi}{4}\alpha_m^2), \tag{5.5a}$$

$$m = 0: \quad V = \lambda(\pi h_0^2 + \frac{\pi}{2}\alpha_0^2). \tag{5.5b}$$

A new constant parameter $\bar{h}$ is introduced, which is based on the principle of mass conservation written as

$$V = \pi\bar{h}^2\lambda = const.$$

Using the expression in equations (5.5a) and (5.5b) $h_0$ is obtained as

$$m \neq 0: \quad h_0 = \bar{h}\sqrt{1 - \frac{\alpha_m^2}{4\bar{h}^2}}, \tag{5.6a}$$

$$m = 0: \quad h_0 = \bar{h}\sqrt{1 - \frac{\alpha_0^2}{2\bar{h}^2}}. \tag{5.6b}$$

Analogously to the Volume $V$ the surface $S$ of the liquid within one wave length is calculated as

$$
\begin{aligned}
S &= \int\limits_{z=0}^{\lambda} \int\limits_{\theta=0}^{2\pi} \sqrt{1 + \left(\frac{1}{h}\frac{\partial h}{\partial \theta}\right)^2 + \left(\frac{\partial h}{\partial z}\right)^2}\, h\, d\theta dz \\
&\approx \int\limits_{z=0}^{\lambda} \int\limits_{\theta=0}^{2\pi} \left[1 + \frac{1}{2}\left(\frac{1}{h}\frac{\partial h}{\partial \theta}\right)^2 + \frac{1}{2}\left(\frac{\partial h}{\partial z}\right)^2\right] h\, d\theta dz \\
&= \int\limits_{z=0}^{\lambda} \int\limits_{\theta=0}^{2\pi} \left[1 + \frac{1}{2}\underbrace{\frac{1}{h^2}}_{\approx \bar{h}^2}\alpha_m^2 m^2 \sin^2(m\theta)\cos^2(kz) + \frac{1}{2}\alpha_m^2 \cos^2(m\theta)\sin^2(kz)k^2\right] h\, d\theta dz \\
&= \lambda\left[2\pi h_0 + \frac{\pi}{4}m^2\frac{\alpha_m^2}{\bar{h}^2}h_0 + \frac{\pi}{4}k^2\alpha_m^2 h_0\right]
\end{aligned}
$$

Here again the assumption of small deformation was applied, so that the root was is linearised and $h^2$ was approximated by $\bar{h}^2$. Using a linearized approximation of (5.6a) and (5.6b)

$$
\begin{aligned}
m \neq 0 : \quad h_0 &\approx \bar{h}(1 - \frac{\alpha_m^2}{8\bar{h}^2}), \\
m = 0 : \quad h_0 &\approx \bar{h}(1 - \frac{\alpha_0^2}{4\bar{h}^2}),
\end{aligned}
$$

the surface area is obtain as

$$
\begin{aligned}
m \neq 0 : \quad S &= \lambda\left[2\pi\bar{h} + \frac{\pi}{4}\frac{\alpha_m^2}{\bar{h}^2}(k^2\bar{h}^2 + m^2 - 1)\right], \\
m = 0 : \quad S &= \lambda\left[2\pi\bar{h} + \frac{\pi}{2}\frac{\alpha_m^2}{\bar{h}^2}(k^2\bar{h}^2 - 1)\right],
\end{aligned}
$$

where higher-order terms associeted with $\alpha_m^4$ have been neglected. The surface area $S$ is evidently composed of two parts:

- A non-deformed constant part $\lambda 2\pi\bar{h}$.

- A deformed non-constant part $\lambda\frac{\pi}{4}\frac{\alpha_m^2}{\bar{h}^2}(k^2\bar{h}^2 + m^2 - 1)$.

For the change in the surface energy only the deformed non-constant part is of interest, so that only the deformed non-constant part multiplied by the surface tension coefficient $\sigma$ has to be considered for the surface energy $P$, which reads

$$
\begin{aligned}
m \neq 0 : \quad P &= \lambda\frac{\pi}{4}\frac{\alpha_m^2}{\bar{h}}(k^2\bar{h}^2 + m^2 - 1)\sigma, \\
m = 0 : \quad P &= \lambda\frac{\pi}{2}\frac{\alpha_m^2}{\bar{h}}(k^2\bar{h}^2 - 1)\sigma.
\end{aligned}
$$

For the first case $m \neq 0$ the surface energy $P$ is always greater than 0. Hence, it always represents a sink of energy, and in consequence the jet stays stable. For the case $m = 0$ the surface energy $P$ is negative under the condition $k^2 \bar{h}^2 - 1 < 0$ and the jet gets unstable. This immediately leads to the conclusion that only perturbations associated with $m = 0$ can lead to a capillary instability, and the wave length of the perturbation must satisfy

$$\lambda > 2\pi \bar{h}. \tag{5.7}$$

The kinetic energy contained inside the considered volume may be generally written as

$$K = \frac{1}{2}\rho \int_V \mathbf{u}^2 \; dV, \tag{5.8}$$

where $\rho$ is the density of the liquid. Assuming inviscid flow the irrotational velocity flied can be computed form a potential $\xi$ written as $\mathbf{u} = \nabla \xi$. Using Greens first identity the volume integral of the kinetic energy can be split into a surface integral and a volume integral involving the Laplacian $\Delta \xi$, which is identically zero in potential flow. Accordingly, equation (5.8) becomes

$$\begin{aligned}
K &= \frac{1}{2}\rho \int_V (\nabla \xi)^2 \; dV \\
&= \frac{1}{2}\rho \left[ \int_S \xi (\nabla \xi) \cdot \mathbf{n} \; dS - \int_V \xi \underbrace{\Delta \xi}_{=0} \; dV \right] \\
&= \frac{1}{2}\rho \int_S \xi (\nabla \xi) \cdot \mathbf{n} \; dS. \tag{5.9}
\end{aligned}$$

The unknown potential is computed form the Laplace equation

$$\Delta \xi = \frac{\partial^2 \xi}{\partial r^2} + \frac{1}{r}\frac{\partial \xi}{\partial r} + \frac{1}{r^2}\frac{\partial^2 \xi}{\partial \theta^2} + \frac{\partial^2 \xi}{\partial z^2} = 0.$$

Using a separation ansatz

$$\xi = A(r)B(\theta)C(z)D(t),$$

substituting this ansatz into the Laplace equation and multiplying by $1/(ABC)$ yields

$$\frac{A''}{A} + \frac{1}{r}\frac{A'}{A} + \frac{1}{r^2}\frac{B''}{B} + \frac{C''}{C} = 0. \tag{5.10}$$

Isolating the term $C''/C$ on the right hand side the equation becomes

$$\frac{A''}{A} + \frac{1}{r}\frac{A'}{A} + \frac{1}{r^2}\frac{B''}{B} = -\frac{C''}{C} = const = k^2.$$

Since the left hand side depends only on independent variables $r, \theta$ and $t$ and the right hand side only on $z$, sides must be both equal to a constant. The equation

$$C'' + k^2 C = 0$$

is solved, and the solution, which is consistent with the specification of the perturbed radius $r$ given by equation (5.2), reads

$$C = C_1 \cos(kz).$$

Substituting this solution into equation (5.10), separating the $\theta-$dependent parts and using the same arguments as above we obtain

$$r^2 \frac{A''}{A} + r\frac{A'}{A} - r^2 k^2 = -\frac{B''}{B} = const = m^2.$$

The equation

$$B'' + m^2 B = 0$$

is solved and the solution which is consistent with equation (5.2) reads

$$B = C_2 \cos(m\theta).$$

The two solutions $C(z)$ and $B(\theta)$ substituted into equation (5.10) yielding a differential equation for $A(r)$:

$$r^2 A'' + rA' - (m^2 + k^2 r^2)A = 0$$

The so obtained ordinary differential equation represents a modified Bessel differential equation of order $m$, whose solutions may be written in terms of the modified Bessel functions:

$$A(r) = C_3 I_m(k\rho) + C_4 J_m(kr)$$

Since $J_m(kr)$ goes to infinity as $r$ goes to zero, the integration constant $C_4$ must be zero to provide a finite solution at the center of the jet, reads

$$A(r) = C_3 I_m(kr).$$

Collecting the results for the individual functions in the separation ansatz the potential $\xi$ can be rewritten as

$$\xi(r, \theta, z, t) = D_m(t) I_m(kr) \cos(m\theta) \cos(kz). \tag{5.11}$$

A relation between $\alpha_m$ and $D_m$ is found using the kinematic boundary condition at the surface of the jet $r = h(\theta, z, t)$ written as

$$u = \frac{\partial h}{\partial t} + w\frac{\partial h}{\partial z} + v\frac{\partial h}{h\partial v}. \tag{5.12}$$

Assuming small deformations the gradients with respect to $z$ and $\theta$ are very small so that equation (5.12) can be approximated as

$$\frac{\partial h}{\partial t} = u = \left. \frac{\partial \xi}{\partial r} \right|_{r=\bar{h}} \tag{5.13}$$

The deviation of the kinematic boundary condition needs the assumption that the gradients of $h$ in radial direction $r$ are huge compared to the gradients in axial direction $z$. Substituting (5.2) and (5.11) into the kinematic boundary condition (5.13) yields:

$$\frac{d\alpha_m}{dt} = kD_m(t)I'_m(k\bar{h}). \tag{5.14}$$

Approximating the scalar product in equation (5.9) as $\nabla\xi \cdot \mathbf{n} \approx \left.\frac{\partial\xi}{\partial r}\right|_{r=\bar{h}}$ the kinetic energy is obtained as

$$K = \frac{1}{2}\rho \int\limits_{z=0}^{\lambda} \int\limits_{\theta=0}^{2\pi} \xi \left.\frac{\partial\xi}{\partial\rho}\right|_{r\approx\bar{h}} \bar{h}\,d\theta dz \tag{5.15a}$$

$$= \frac{1}{2}\rho\bar{h}D_m^2 I_n(k\bar{h})I'_m(k\bar{h}) \int\limits_{z=0}^{\lambda} \int\limits_{\theta=0}^{2\pi} \cos^2(m\theta)\cos^2(kz)d\theta dz \tag{5.15b}$$

$$= \frac{1}{2}\rho\bar{h}D_m^2 I_n(k\bar{h})I'_m(k\bar{h})\pi\frac{\lambda k}{2}. \tag{5.15c}$$

Using the relationship (5.14) and inserting it in (5.15c) yields for different $m$:

$$m \neq 0 : \quad K = \frac{\pi}{4}\lambda\rho\bar{h}^2 \frac{I_m(k\bar{h})}{I'_m(k\bar{h})}\frac{1}{k\bar{h}}\left(\frac{d\alpha_m}{dt}\right)^2$$

$$m = 0 : \quad K = \frac{\pi}{2}\lambda\rho\bar{h}^2 \frac{I_0(k\bar{h})}{I'_0(k\bar{h})}\frac{1}{k\bar{h}}\left(\frac{d\alpha_0}{dt}\right)^2$$

Recalling the condition that the sum of the surface energy and the kinetic energy does not vary in time, which implies

$$\frac{d}{dt}(P + K) = 0, \tag{5.17}$$

the following equation for $\alpha_m$ is obtained:

$$\frac{d}{dt}\left[\lambda\frac{\pi}{4}\sigma\frac{\alpha_m^2}{a}(k^2\bar{h}^2 + m^2 - 1) + \lambda\frac{\pi}{4}\rho\bar{h}^2 \frac{I_m(k\bar{h})}{I'_m(k\bar{h})}\frac{1}{k\bar{h}}\left(\frac{d\alpha_m}{dt}\right)^2\right] = 0. \tag{5.18}$$

Transformation of the previous equation gives an ordinary second order differential equation for $\alpha_m(t)$ for all $m$,

$$\frac{d^2\alpha_m}{dt^2} + \frac{\sigma}{\rho\bar{h}^3}k\bar{h}(k^2\bar{h}^2 + m^2 - 1)\frac{I'_m(k\bar{h})}{I_m(k\bar{h})}\alpha_m = 0 \qquad \forall m,$$
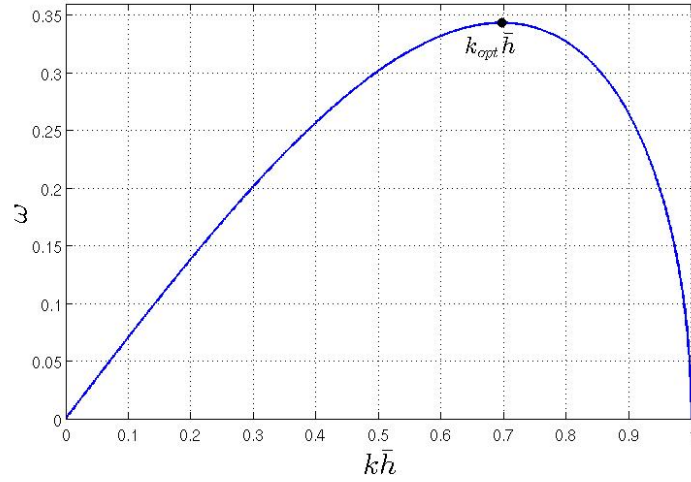
with the exact solution

$$\alpha_m = C_5 e^{i\omega t},$$

Figure 5.3: Dispersion relation to show the dependence of the growth rate $\omega$ on the wave number $k$ for the Rayleigh instability.

where

$$\omega^2 = \frac{\sigma}{\rho\bar{h}^3}k\bar{h}(k^2\bar{h}^2 + m^2 - 1)\frac{I'_m(k\bar{h})}{I_m(k\bar{h})}.$$

The motion can evidently become unstable only if $\omega$ is imaginary associated with $\omega^2 < 0$ and $\omega = \pm i\omega_i$. As mentioned earlier, this can occur only in the case $m = 0$ for $k\bar{h} < 1$, see equation (5.7). The solution for the imaginary $\omega_i$ represents the so called dispersion relation written as

$$\omega_i^2 = \frac{\sigma}{\rho\bar{h}^3}k\bar{h}(1 - k^2\bar{h}^2)\frac{I'_0(k\bar{h})}{I_0(k\bar{h})}. \tag{5.21}$$

Any disturbance $\alpha_m$, whose wave number lies within the range

$$0 < k\bar{h} < 1 \tag{5.22}$$

tend to infinity, which finally leads to a disintegration of the jet. In figure 5.3 the dispersion relation is plotted. The maximum of the curve denotes the fastest growing mode, which occurs at $k_{opt}\bar{h} = 0.697$. The wave length of this mode is

$$\lambda_{opt} \approx 9.02\bar{h}.$$

With the above equation a diameter of the resulting droplets can be estimated based on th volumetric considerations

$$\frac{\pi}{6}D^3 \approx \pi\bar{h}^2\lambda_{opt},$$

which yields the following expression:

$$D \approx 1.89 \cdot 2\bar{h} \approx 1.89 \cdot 2h_0$$

Thus, the expected diameter of a droplet is approximately of the double size of the initial diameter of the undeformed jet $2h_0$.

## 5.2 Travelling time theory

In contrast to the theory on capillary breakup established by Lord Rayleigh the travelling time theory, as presented by Meier et al. (1992), neglects surface tension effects while it considers kinematic effects, which lead to modulations of the local velocity inside the liquid column, and finally to jet instability. As such, the theory assumes an one-dimensional unsteady incompressible inviscid flow without surface tension and gravitational acceleration. The pressure inside the jet is equal to the ambient pressure. Thus the flow of the liquid column is determined only by the local instantaneous velocity $u(r,t)$ and the cross-sectional area $G(r,t)$ of the jet, where the symbols $t$ and $r$ denote the time and space coordinate into the flow direction, respectively. The continuity equation and the momentum equation read

$$\frac{\partial G}{\partial t} + u\frac{\partial G}{\partial r} + G\frac{\partial u}{\partial r} = 0, \tag{5.23a}$$

$$\frac{\partial u}{\partial t} + u\frac{\partial u}{\partial r} = 0. \tag{5.23b}$$

The boundary conditions at the inlet $r = 0$ are imposed as

$$u(0,t) = u_{inl}(t), \tag{5.24a}$$

$$G(0,t) = G_{inl}(t). \tag{5.24b}$$

Lagrangian coordinates are introduced:

$$t(\vartheta) = \vartheta, \tag{5.25a}$$

$$r(\vartheta,\tau) = u_{inl}(\tau)(\vartheta - \tau). \tag{5.25b}$$

The coordinate $\vartheta$ represents the actual time, and $\tau$ stands for the starting time of the flow particles. The transformation of the conservation equations (5.23) into Lagrangian coordinates yields

$$\frac{dG}{d\vartheta} = \frac{G\frac{du_{inl}}{d\tau}}{u - \frac{du_{inl}}{d\tau}(\vartheta - \tau)}, \tag{5.26a}$$

$$\frac{du}{d\vartheta} = 0, \tag{5.26b}$$

and transformed boundary conditions read

$$G(\tau,\tau) = G_{inl}(\tau), \tag{5.27a}$$

$$u(\tau,\tau) = u_{inl}(\tau). \tag{5.27b}$$

An arbitrary but fixed intervall $\tau \in [0, \vartheta]$ is assumed and equation (5.26a) can be rewritten as

$$\frac{dG}{d\vartheta} = a(\vartheta)G(\vartheta), \tag{5.28}$$

with the function

$$a(\vartheta) = \frac{\frac{du_{inl}}{d\tau}}{u(\vartheta) - \frac{du_{inl}}{d\tau}(\vartheta - \tau)}.$$

The exact solution of equation (5.28) is

$$G(\vartheta) = C_1 \ \exp(\int_\tau^\vartheta a(s)ds), \tag{5.29}$$

where $C_1$ is an arbitrary constant. From the fundamental theorem of calculus it follows that

$$\int_\tau^\vartheta a(s)ds = A(\vartheta) - A(\tau),$$

where $A$ is an antiderivative of $a$ and is given as

$$A(s) = \frac{du_{inl}}{d\tau} \ln|u(s) - \frac{du_{inl}}{d\tau}(s - \tau)| \frac{1}{\frac{du(s)}{ds} - \frac{du_{inl}}{d\tau}}$$

$$= -\ln|u(s) - \frac{du_{inl}}{d\tau}(s - \tau)|,$$

because $\frac{du(s)}{ds} = 0$ following equation (5.26b). Substituting the antiderivatives $A(\vartheta)$ and $A(\tau)$ into (5.29) yields:

$$G(\vartheta) = C_1 \frac{u_{inl}}{|u(\vartheta) - \frac{du_{inl}(\tau)}{d\tau}(\vartheta - \tau)|}$$

Recalling the boundary conditions (5.27a), (5.27b) and equation (5.26) it can be seen that

$$G(\tau) = G_{inl}(\tau) = C_1$$

and

$$u(\vartheta, \tau) = u_{inl}(\tau).$$

The resulting theoretical solution in Langrangian coordinates can finally be written as

$$G(\vartheta, \tau) = \frac{G_{inl}(\tau)u_{inl}(\tau)}{|u_{inl}(\tau) - \frac{du_{inl}(\tau)}{d\tau}(\vartheta - \tau)|}, \tag{5.30a}$$

$$u(\vartheta, \tau) = u_{inl}. \tag{5.30b}$$

The present Lagrangian solution yields an instantaneous variation of the local velocity component $u(r, t)$ and the cross-sectional area $G(r, t)$ at a given instant of time $t = \vartheta$ with $r(\vartheta, \tau)$ obtained fom equation (5.25b). The cross-sectional area $G$ becomes infinity, as the denominator in equation (5.30a) vanishes. The location of these

singularities of cross-sectional area shall be determined considering a rotationally symmetric jet. The nozzle radius $R_{inl} := D_{inl}/2$ is assumed constant and the inlet velocity is perturbed introducing a sinusoidal perturbation of the form

$$u_{inl}(\tau) = u_{jet}(1 + \epsilon \sin(2\pi f\tau)), \tag{5.31}$$

where $u_{jet}$ is the unperturbed base velocity, $f$ the frequency and $\epsilon$ the amplitude of the modulation. Dimensionless quantities are introduced in using exactly the same reference quantities as in the numerical flow simulations to obtain comparable results. Thus, the following reference scales are used:

$$L_0 := D_{inl}10, \qquad u_0 := \frac{u_{jet}}{10}, \qquad t_0 := \frac{L_0}{u_0} = \frac{D_{inl}}{u_{jet}}100.$$

This yields the following dimensionless representation of the velocity inflow boundary condition

$$\vartheta^* = \frac{\vartheta}{t_0}, \qquad \tau^* = \frac{\tau}{t_0}, \qquad R^* = \frac{R}{L_0}, \qquad f^* = ft_0$$

$$u_{inl}^* = \frac{u_{inl}}{u_0} = 10(1 + \epsilon \sin(\Omega^*\tau^*)), \tag{5.32}$$

with the dimensionless frequency $\Omega^* := 2\pi f^*$. Based on these assumptions a dimensionless representation of the radius can be directly deduced from equation (5.30a)

$$R^*(\vartheta^*, \tau^*) = \sqrt{\frac{R_{inl}^{*}{}^2(1 + \epsilon \sin(\Omega^*\tau^*))}{|(1 + \epsilon \sin(\Omega^*\tau^*)) - \epsilon\Omega^* \cos(\Omega^*\tau^*)(\vartheta^* - \tau^*)|}} \tag{5.33}$$

As already mentioned above, the solution becomes singular at points of infinite radius. Downstream of the first point of infinite radius, the distribution of the flow material is no longer unique. It is possible to find the shortest distance $r_p^*$ for the first singularity, based on two conditions. One condition is that the denominator in equation (5.30a) is zero,

$$D(\vartheta^*, \tau^*) = \frac{\partial r^*}{\partial \tau^*}\frac{1}{10} = -1 - \epsilon \sin(\Omega^*\tau^*) + \epsilon\Omega^* \cos(\Omega^*\tau^*)(\vartheta^* - \tau^*) = 0.$$

The second condition for the shortest distance $r_p^*$ is that $r^*$ is monotonously increasing with respect to $\tau^*$, which implies

$$\frac{\partial^2 r^*}{\partial \tau^{*2}} = -20\epsilon\Omega^* \cos(\Omega^*\tau^*) - 10\epsilon\Omega^{*2} \sin(\Omega^*\tau^*)(\vartheta^* - \tau^*) = 0.$$

Using both conditions the values $\vartheta_{p,T}^*$ and $\tau_{p,T}^*$ can be obtained in a closed form as follows:

$$\tau_{p,T}^* = \frac{1}{\Omega^*} \arcsin\left(\frac{1}{2\epsilon} - \frac{1}{2}\sqrt{\frac{1}{\epsilon^2} + 8}\right) \tag{5.34}$$

$$\vartheta_{p,T}^* = \tau_{p,T}^* - \frac{2}{\Omega^*} \cot(\Omega^*\tau_{p,T}^*) \tag{5.35}$$

The subscript $T$ refers to the travelling time theory. Knowing these quantities the first critical value $r_{p,T}^*$ can be obtained as

$$r_{p,T}^* = 10[1 + \epsilon \sin(\Omega^* \tau_{p,T}^*)](\vartheta_{p,T}^* - \tau_{p,T}^*). \tag{5.36}$$

It can be seen that equation (5.34) and (5.35) represent only one particular solution of an inifinte number of periodic solutions which are associated with equation (5.33) generalized to

$$\tau_{p_l,T}^* = \frac{1}{\Omega^*} \arcsin \left( \frac{1}{2\epsilon} - \frac{1}{2}\sqrt{\frac{1}{\epsilon^2} + 8} \right) + \frac{2l\pi}{\Omega^*}, \quad l \in \mathbb{Z}. \tag{5.37}$$

Each individual solution for $l \in \mathbb{Z}$ corresponds to a maximum cross-section, as the denominator of equation (5.33) attains a local minimum, or become zero. Based on the periodicity given by equation (5.37) the dimensionless distance between two neighboring points of maximum cross-section can be calculated as

$$\lambda_T^* = \frac{20\pi}{\Omega^*} \left( 1 + \epsilon \left( \frac{1}{2\epsilon} - \frac{1}{2}\sqrt{\frac{1}{\epsilon^2} + 8} \right) \right). \tag{5.38}$$

In figure 5.4 the streamwise variation of the dimensionless radius $R^*$ obtained from equation (5.33) for the parameters $D_{inl}^* = 1$, $\Omega^* = 100$, $\epsilon = 2.5\%$, and $\vartheta^* = 0.7$ is shown beginning from the position of the orifice $r^* = 0$. The positions associated with
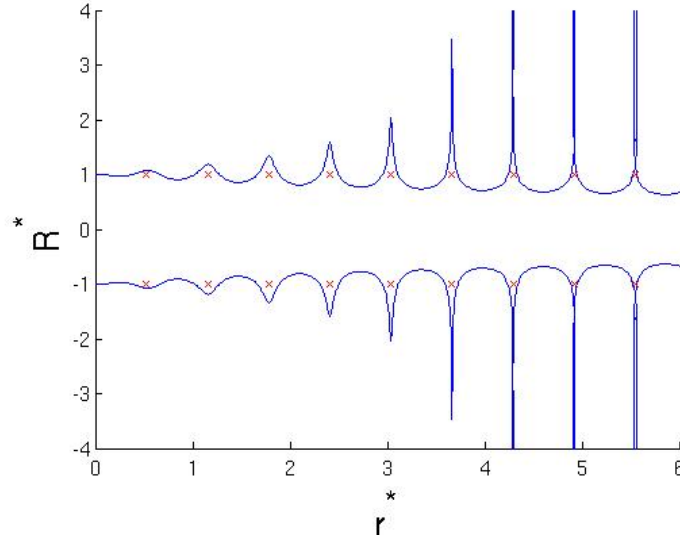


Figure 5.4: Streamwise variation of the dimensionless radius $R^*$ and position of maximum cross-section.

a local maximum cross-section are indicated by red crosses. Downstream of the first

point of infinite radius, the distribution of the flow material is no longer unique. Figure 5.5 shows for the considered parameters the evolution of the characteristic lines, which correspond to the trajectories of the material particles with different starting time $\tau^*$. In the shown space-time domain the starting times $\tau^*$ are varying from 0 to 0.7 with $\Delta\tau^* = 0.02$. The thick black line indicates the ending time $\vartheta^* = 0.7$. The characteristics remain always straight lines, whose inclination angle is determined by the instantaneous inlet velocity according to equation (5.32) dependent of the starting time $\tau^*$. The sinusoidal perturbation of the velocity leads to a converging/diverging pattern of the characteristics in the space-time domain resulting in a periodic accumulation of material. Positions with maximum cross-section but finite radius seen in figure 5.4 near the orifice appear in figure 5.5 as regions on the line $\vartheta^* = 0.7$, where characteristics are getting closer but do not intersect. The intersection point of two neighboring characteristics located on the line $\vartheta^* = 0.7$, which is nearest to the orifice (indicated by a circle in figure 5.5) corresponds to the position of the first singularity given by equation (5.36). Since the travelling time theory is based on purely kinematic
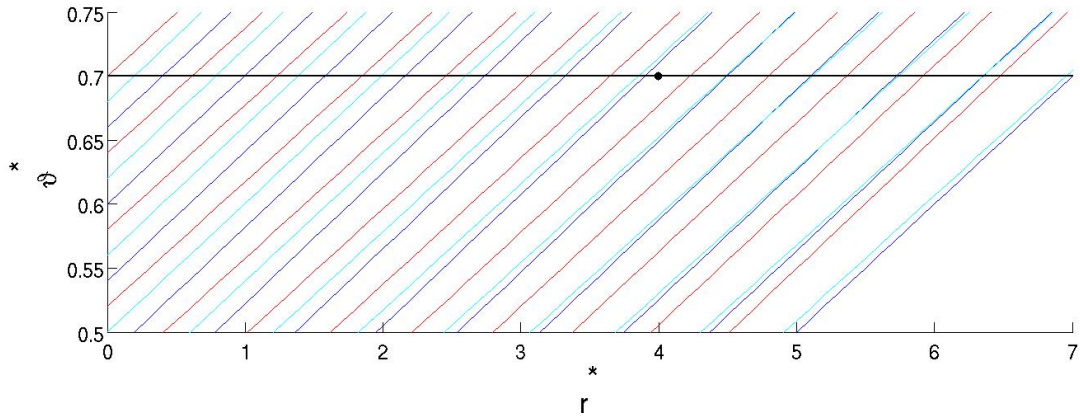


Figure 5.5: Characteristic lines for different starting times $\tau^*$.

considerations, it is not supposed to describe the phenomenon of capillary breakup. It is nonetheless a useful approach for describing the streamwise distribution of liquid material emerging from a perturbed inflow. The strong local accumulation of liquid due to the perturbations may lead to a breakup so that this essentially kinematic mechanism prevails over the typical capillary instability mechanism.

# 6 Numerical Simulations

The present numerical computations of the disintegration of a liquid column consider a perturbed jet flow configuration which was experimentally investigated by Meier et al. (1992). Their experimental arrangement, the experimental conditions, and some essential optical observations on the presently considered cases will be shown in more detail in the following subsection.

## 6.1 Experimental results

The here simulated cases are taken from an experimental study of Meier et al. (1992), who examined differently modulated jets at fairly low Weber numbers, so that the flow conditions are basically well inside the capillary breakup regime. At the orifice the inlet velocity $u_{inl}$ is modulated with a sinusoidal perturbation

$$u_{inl}(t) = u_{jet}(1 + \epsilon \sin(2\pi f t)), \tag{6.1}$$

where $u_{jet}$ is a constant average inlet velocity, $\epsilon$ is a dimensionless amplitude, and $f$ a frequency in Hertz ($Hz$). In figure 6.1 the main components of the apparatus for the
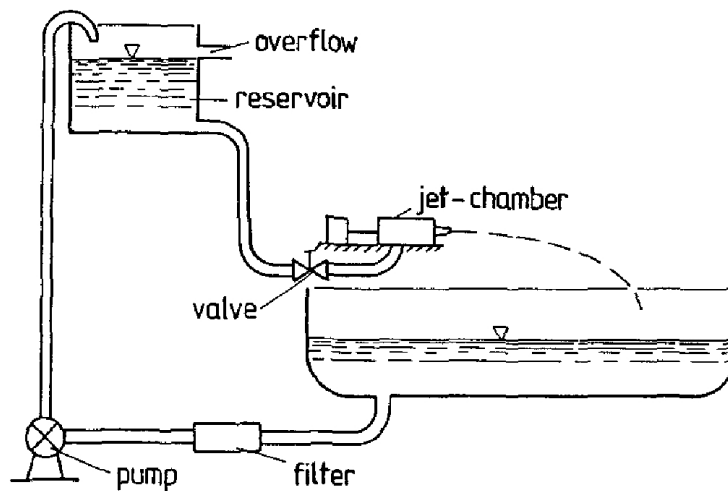


Figure 6.1: Schematic of the experimental facility. Figure from Meier et al. (1992).

flow experiments of Meier et al. (1992) are shown. A reservoir with an overflow outlet

ensures a constant hydrostatic pressure. Inside a jet-chamber upstream of the nozzle a periodically moving piston is used to realize the desired sinusoidal velocity modulation. Four experimental cases were chosen as test cases for the present numerical studies. In figure 6.2 photographs taken for the four considered experimental cases are shown. The
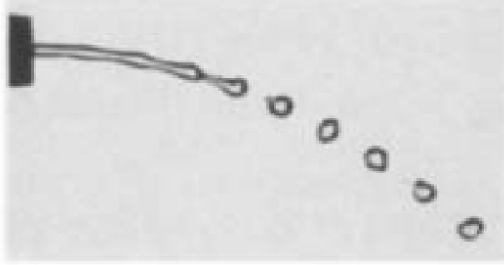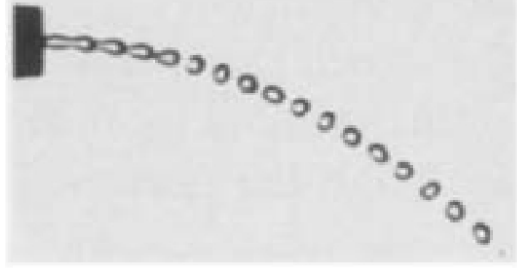


(a) Case I: Jet with a frequency $f = 100Hz$ and an amplitude $\epsilon = 2.5\%$.
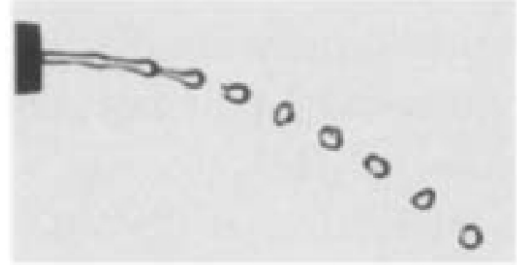
(b) Case II: Jet with a frequency $f = 100Hz$ and an amplitude $\epsilon = 5\%$.
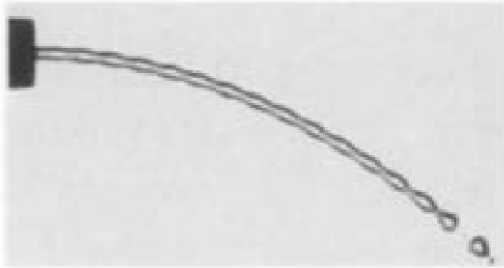
(c) Case III: Jet with a frequency $f = 180Hz$ and an amplitude $\epsilon = 2.5\%$.

(d) Case IV: Jet with a frequency $f = 180Hz$ and an amplitude $\epsilon = 5\%$.

Figure 6.2: Different jets for various modulation frequencies and amplitudes. The diameter of the nozzle is $2.4mm$, the mean jet velocity is $u_{jet} = 1m/s$ and the Weber number is $We = 34$. Figures from Meier et al. (1992).

pictures were taken in $35mm$ format using high-resolution film material. For all four experiments the diameter of the nozzle is $D_{inl} = 2.4mm$, the mean jet inlet velocity is $u_{jet} = 1m/s$. Using water at atmospheric ambient conditions as working liquid the Reynolds, Weber and Ohnesorge numbers based on the nozzle inlet conditions read

$$Re = 2400, \qquad We = 34, \qquad Oh = 2.43 \cdot 10^{-3},$$

respectively. Introducing the values of these dimensionless parameters into the nomogram shown in figure 5.1 it becomes obvious that all four experimental cases lie inside the capillary breakup regime. In table 6.1 the disintegration lengths are listed for each experimental case. It can be seen that as the frequency is increased from $100Hz$ to $180Hz$ in the case $\epsilon = 2.5\%$, the disintegration length increases. It seems that the jet gets stabilized through the higher frequency $180Hz$. This tendency of stabilization was also observed in other experimental cases examined in the study of Meier et al. (1992).

| Case | Frequency | Amplitude | Disintegration length |
|:----:|:---------:|:---------:|:---------------------:|
| I    | 100Hz     | 2.5%      | $r^*_{p,exp} = 13.3 D^*_{inl}$ |
| II   | 100Hz     | 5.0%      | $r^*_{p,exp} = 10.0 D^*_{inl}$ |
| III  | 180Hz     | 2.5%      | $r^*_{p,exp} = 27.8 D^*_{inl}$ |
| IV   | 180Hz     | 5.0%      | $r^*_{p,exp} = 8.9 D^*_{inl}$  |

Table 6.1: Considered cases and experimentally observed disintegration lengths.

However no deterministic rule could be deduced, because there are also experimental cases, where an increasing frequency caused a decreasing disintegration length. Moreover, increasing the amplitude from 2.5% to 5.0% reduces the disintegration length for both frequencies to almost the same axial extension as seen from figure 6.2(b) and 6.2(d). In all experiments with the exception of case IV the diameters of the droplets are approximately double in size of the inlet diameter. This is in consistence with the Rayleigh instability theory. In case IV the diameters of the droplets are somewhat smaller than the double in size of the inlet diameter.

## 6.2 Computational setup

All computations are performed on a multi-processor server of the Institute of Fluid Mechanics and Heat Transfer at Graz University of Technology. The numerical program used for the simulations is an inhouse Fortran code, which solves the governing equations in a non-dimensional representation based on the following reference quantities:

$$L_0 := D_{inl}10, \quad U_0 := \frac{u_{jet}}{10}, \quad t_0 := \frac{L_0}{U_0} = \frac{D_{inl}}{u_{jet}}100.$$

Using these reference quantities the dimensionless representation of the imposed inflow boundary condition reads:

$$D^*_{inl} = \frac{D_{inl}}{L_0} = 0.1, \qquad u^*_{jet} = \frac{u_{jet}}{U_0} = 10,$$

$$f^* = ft_0, \qquad u^*_{inl} = \frac{u_{inl}}{U_0} = u^*_{jet}(1 + \epsilon \sin(\Omega^* t^*)),$$

with the dimensionless frequency $\Omega^* := 2\pi f^*$. For all four considered cases the following nozzle inlet conditions and material properties are assumed:

$$u_{jet} = 1.0\text{m/s}, \qquad D_{inl} = 2.4 \cdot 10^{-3}\text{m},$$
$$\rho_1 = 984 \ kg/m^3, \qquad \rho_2 = 1.204 \ kg/m^3,$$
$$\mu_1 = 1.0 \ \text{m}Pa \cdot s, \qquad \mu_2 = 1.8 \cdot 10^{-2} \ \text{m}Pa \cdot s.$$

The subscript 1 indicates water, and the subscript 2 indicates air. Using the above parameters the reference time becomes $t_0 = 0.24s$. The geometry of the presently used
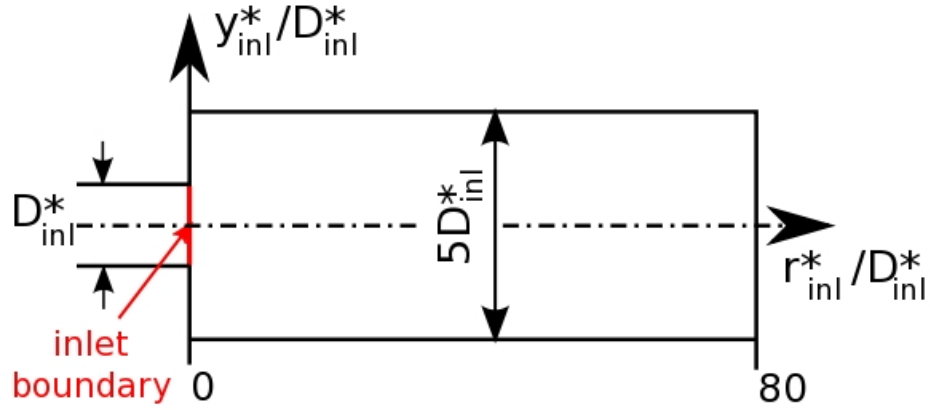
Figure 6.3: Computational domain.

domain is sketched in figure 6.3. The counting of the radial coordinate pointing into the streamwise direction starts with $r^* = 0$ at the inlet boundary. The streamwise and lateral extensions of the domain are $80D^*_{inl}$ and $5D^*_{inl}$, respectively. In table 6.2 all important parameters for the numerical simulations are listed. $N_r$, $N_\theta$, $N_\phi$ are the number of cells in streamwise, lateral, and azimuthal directions, respectively, and $N$ is the total number of cells. It is noted that the here considered flow can be assumed as axisymmetric, so that the resolution in the azimuthal direction is irrelevant. Therefore, the minimum possible number of grid cells admitted by the spatially three-dimensional code is chosen for the azimuthal direction.

| Domain size and grid: | Material properties: | Dimensionless numbers: |
|---|---|---|
| streamwise extension: $r^*_{max} = 80D^*_{inl}$ | $\rho^*_1 = 1$ | $Re = \frac{U_0 \rho_1 L_0}{\mu_1} = 2400$ |
| lateral extension: $y^*_{max} = 5D^*_{inl}$ | $\rho^*_2 = 1.223 \cdot 10^{-3}$ | $\widetilde{W}e = \frac{\rho_1 U_0^2 L_0}{\sigma} = 3.4$ |
| grid resolution: | $\mu^*_1 = 1$ | |
| $N_r = 2304$ | $\mu^*_2 = 1.8 \cdot 10^{-2}$ | |
| $N_\theta = 80$ | | |
| $N_\phi = 4$ | | |
| $N = 737280$ | | |

Table 6.2: Key parameters for the numerical simulations.

## 6.3 Numerical results

As noted in the previous subsection, four different cases were computed and analyzed. All of these simulations were carried out using two alternative approaches for capturing the liquid/gas interface, the Koren flux limiter (KFL) scheme and the HRIC scheme. All calculations were started from the same initial condition, prescribed as a continuous water column with the diameter of the orifice extending from the inlet to the outlet of the domain.
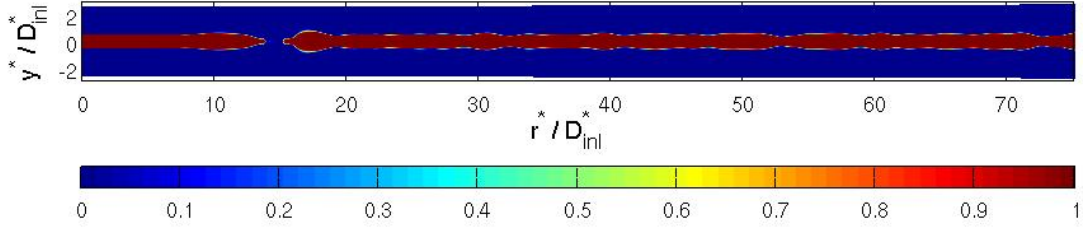


Figure 6.4: The liquid color function at time $t^* = 0.14$.

The streamwise velocity of the initial water column was set to $u^* = 10$, while the other components were set to zero. The velocity of the ambient air was initialized with zero into all directions. Even without imposing any perturbation on the jet inlet velocity the initial accommodation of the prescribed water column to a solution, which satisfies the balances of mass and momentum, introduces sufficiently high perturbations to trigger a capillary breakup of the column. Figure 6.4 exemplarily shows contours of the liquid color function obtained at a relatively early stage at $t^* = 0.14$. Here the liquid column has evidently started to break up, but the shown solution is still far aways from a temporally converged state. Therefore, all simulations were run until the disintegration length exhibited neither increasing nor decreasing tendency anymore, but stably varied within a certain narrow range of a couple of jet diameters in distance. Depending on the considered inflow perturbation this converged state could be reached already after approximately two up to eight flow-through times. The flow-through time for the presently considered cases is

$$t^* = \frac{r^*_{max}}{U^*_{jet}} = 0.8. \tag{6.2}$$

### 6.3.1 Numercial results obtained with the Koren flux limiter scheme

All numerical experiments described in this subsection are done with the Koren flux limiter scheme. The initial condition is always the starting solution mentioned above.

**Case I**

The characteristic parameters for the inflow perturbation in this case are:

$$\epsilon = 2.5\%, \qquad\qquad f = 100\text{Hz},$$
$$\Omega^* = 2\pi f t_0 = 150.80, \qquad\qquad u^*_{inl} = 10(1 + 0.025\sin(\Omega^* t^*)).$$

In figure 6.5(a) the contours of the liquid color function are shown at $t^* = 1.78$, which corresponds to roughly two flow through-times. It can be seen that the disintegration length extends approximately to the point $r^*_p = 22 D^*_{inl}$. The diameters of the predicted droplets, especially downstream of $r^* = 35 D^*_{inl}$, are approximately of the double size of the initial diameter of the undeformed jet, which is consistent with the Rayleigh breakup theory. As compared to the experiment the simulated disintegration length is evidently longer than the experimental one, being $r^*_{p,exp} = 13.3 D^*_{inl}$. Regarding the position of the first singularity in the solution of the travelling time theory as breakup position the evaluation of equation (5.36) would give a disintegration length $r^*_{p,T} = 26.5 D^*_{inl}$. The wave length (= distance between two neighboring maxima in $R^*$) predicted by the travelling time theory is:

$$\lambda^*_T = 4.2 D^*_{inl}.$$

In figure 6.5(b) the upper plot shows the simulated contours of the color function together with streamwise variation of the dimensionless radius of the jet $R^*$ analytically obtained from equation (5.33), and the wave lengths $\lambda^*_{sim}$, $\lambda^*_T$ in the near-field of the orifice. The simulated wave length which is obtained as the distance between two neighboring maximum cross-sections of the liquid is $\lambda^*_{sim} = 3.7 D^*_{inl}$ in this region. The wave length predicted by the travelling time theory is evidently greater than the simulated wave length. It can be also seen that the simulated contours do not agree with the pattern of the travelling time theory. In figure 6.5(b) the lower plot shows the contours of the liquid color function near the breakup of the liquid into individual droplets. The simulated wave length is here around $\lambda^*_{sim} = 3.4 D^*_{inl}$, which is a bit smaller than the simulated wave length in the near-field of the orifice.

**Case II**

The second numerical test case differs from case I only in the twice as high amplitude of the perturbation $\epsilon$. The characteristic parameters of this case are:

$$\epsilon = 5.0\%, \qquad\qquad f = 100\text{Hz},$$
$$\Omega^* = 2\pi f t_0 = 150.80, \qquad\qquad u^*_{inl} = 10(1 + 0.05\sin(\Omega^* t^*)).$$

In figure 6.6(a) the solution of the contours of the color function are shown at $t^* = 1.77$, which is somewhat beyond approximately two flow-through times. It can be observed that the disintegration length $r^*_p = 22 D^*_{inl}$ is the same as in case I. Increasing the amplitude from $\epsilon = 2.5\%$ to $\epsilon = 5.0\%$ does evidently not cause a significant change in the predicted disintegration length for a frequency $f = 100 Hz$. Again

the calculated disintegration length is longer than the experimental one, i.e. $r_{p,exp}^* = 10.0D_{inl}^*$. The travelling time theory predicts a disintegration length $r_{p,T}^* = 13.2D_{inl}^*$ given by equation (5.36). The wave length predicted by the travelling time theory and the simulated counterpart in the near-field of the orifice are:

$$\lambda_T^* = 4.2D_{inl}^*, \qquad \lambda_{sim}^* = 3.5D_{inl}^*.$$

This discrepancy can also be seen in figure 6.6(b) in the upper plot, where the wave length predicted by the travelling time theory is smaller than the simulated wave length. The underlying predictions for the clustering of material differ somewhat more than in case I. The simulated wave length in near-field of the orifice is smaller in case II than in case I. The wave length predicted by the travelling time theory stays almost the same in the cases I and II,as the higher amplitude $\epsilon = 5\%$ changes the result only in the second digit. The lower subplot in figure 6.6(b) shows the conditions immediately upstream of the disintegration point, where the simulated wave length is around $3.6D_{inl}^*$. The simulated wave lengths in the near-field of the orifice and upstream of the disintegration point are evidently nearly the same.

**Case III**

The numerical simulation for case III applies the same amplitude $\epsilon$ for the velocity inlet perturbation as in case I, but with an increased frequency $f$. The characteristic parameters are:

$$\epsilon = 2.5\%, \qquad\qquad f = 180\text{Hz},$$
$$\Omega^* = 2\pi f t_0 = 271.43, \qquad u_{inl}^* = 10(1 + 0.025\sin(\Omega^* t^*)).$$

In figure 6.7(a) the contours of the liquid color function are shown at $t^* = 8.18$. In this case the simulation had to be run for a much longer dimensionless time to reach a converged solution as compared to the cases I and II. The axial extension of the domain was increased to $100D_{inl}^*$ to avoid any upstream effect of the outlet boundary condition on the liquid breakup. The converged solution exhibits a disintegration length around $70D_{inl}^*$. Increasing the frequency from $f = 100Hz$ to $f = 180Hz$, while keeping $\epsilon = 2.5\%$ the same, evidently exerts a stabilizing effect also in the numerical solution. As such the numerical solution features correctly the experimentally observed tendency that the increase in frequency increases the disintegration length. Its quantitative extension is, however, significantly overpredicted as compared to the experiments, where the disintegration length extends only to $r_{p,exp}^* = 27.7D_{inl}^*$. Again the diameters of the droplets are approximately of the double size of the initial diameter of the undeformed jet as predicted by the Rayleigh instability theory. The travelling time theory predicts a disintegration length and a perturbation wave length, as obtained from equations (5.36) and (5.38), $r_{p,T}^* = 14.7D_{inl}^*$ and $\lambda_T^* = 2.3D_{inl}^*$ respectively.
In the upper subplot of figure 6.7(b) it can be seen that the wave length predicted by the travelling time theory is smaller than the simulated wave length in the near-field of the orifice, which is $\lambda_{sim}^* = 2.7D_{inl}^*$. This is in contrast to the cases I and II, where the
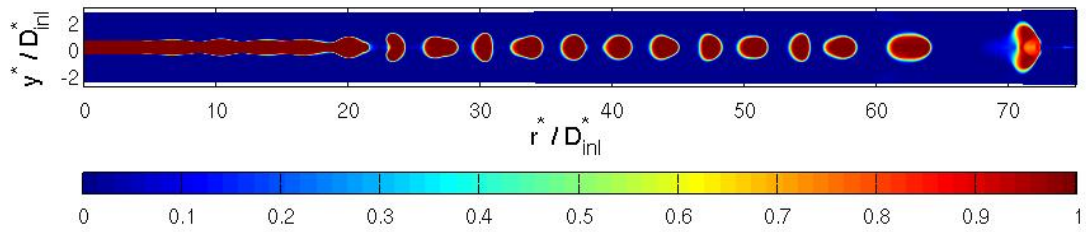
travelling time theory always predicted larger values than the simulations. The lower plot of figure 6.7(b) indicates an increase of the simulated wave length compared to the value obtained in the near-field of the orifice. In the shown region near the breakup of the liquid into individual droplets the simulated wave length is around $4.7D^*_{inl}$.

## Case IV

Case IV assumes the same conditions as case III but with an increased perturbation amplitude $\epsilon$. The characteristic parameters are:

$$\epsilon = 5.0\%, \qquad\qquad\qquad f = 180\text{Hz},$$
$$\Omega^* = 2\pi f t_0 = 271.43, \qquad\qquad u^*_{inl} = 10(1 + 0.05\sin(\Omega^*t^*)).$$

In figure 6.8(a) the simulated contours of the color function obtained at $t^* = 5.19$ are shown. The disintegration length is $r^*_p = 64D^*_{inl}$. Alike in case III the numerical simulation had to be run over several flow through times until a converged solution was reached. Increasing the amplitude from 2.5% to 5.0% with a frequency $f = 180Hz$ causes a decrease in the simulated disintegration length from about $70D^*_{inl}$ (case III) to about $64D^*_{inl}$. The same effect is observed in the experimental results, see figure 6.2, but in the experimental results the relative quantitative reduction of the disintegration length is much stronger, where it is reduced from $r^*_{p,exp} = 27.8D^*_{inl}$ to $r^*_{p,exp} = 8.9D^*_{inl}$. Similar to the case III the numerical results reflect correctly the experimentaly observed tendency, but not the quantitative extent of the changes. The perturbation wave length predicted by the travelling time theory and that obtained from the simulations are $\lambda^*_T = 2.3D^*_{inl}$, and $\lambda^*_{sim} = 2.6D^*_{inl}$, respectively. This is well visible in figure 6.8(b) in the upper plot, where the simulated wave length of the perturbation is bigger than the wave length predicted by the travelling time theory. In this particular case the travelling time theory seems to give a quite accurate prediction of the disintegration length. The evaluation of the equation (5.36) gives a value $r^*_{p,T} = 7.3D^*_{inl}$, which is close to the experimental results. Comparing the upper with the lower plot in figure 6.8(b) a streamwise increase of the simulated wave length can be observed. Accordingly, the simulated wave length seen in the lower plot of figure 6.8(b) upstream of the disintegration point is around $3.4D^*_{inl}$, which is greater than value obtained in the near-field of the orifice.
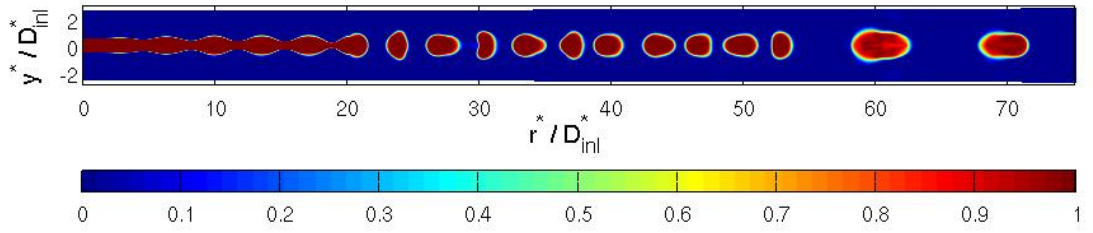
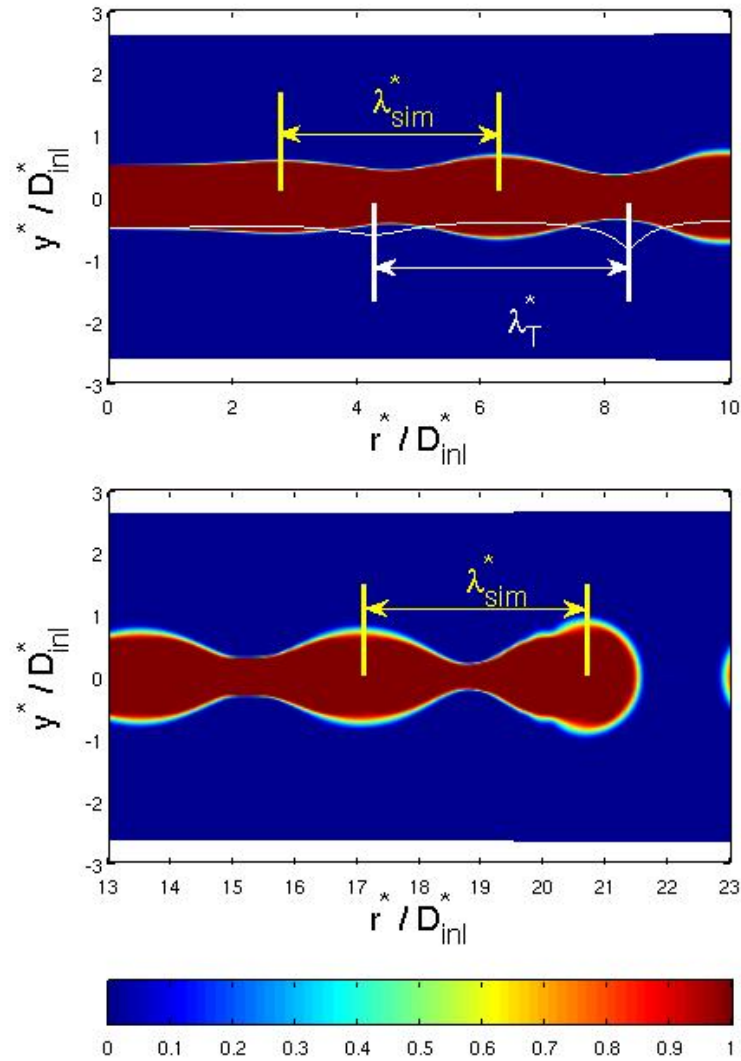(a) Contours of liquid color function at $t^* = 1.78$ shown in the full domain.
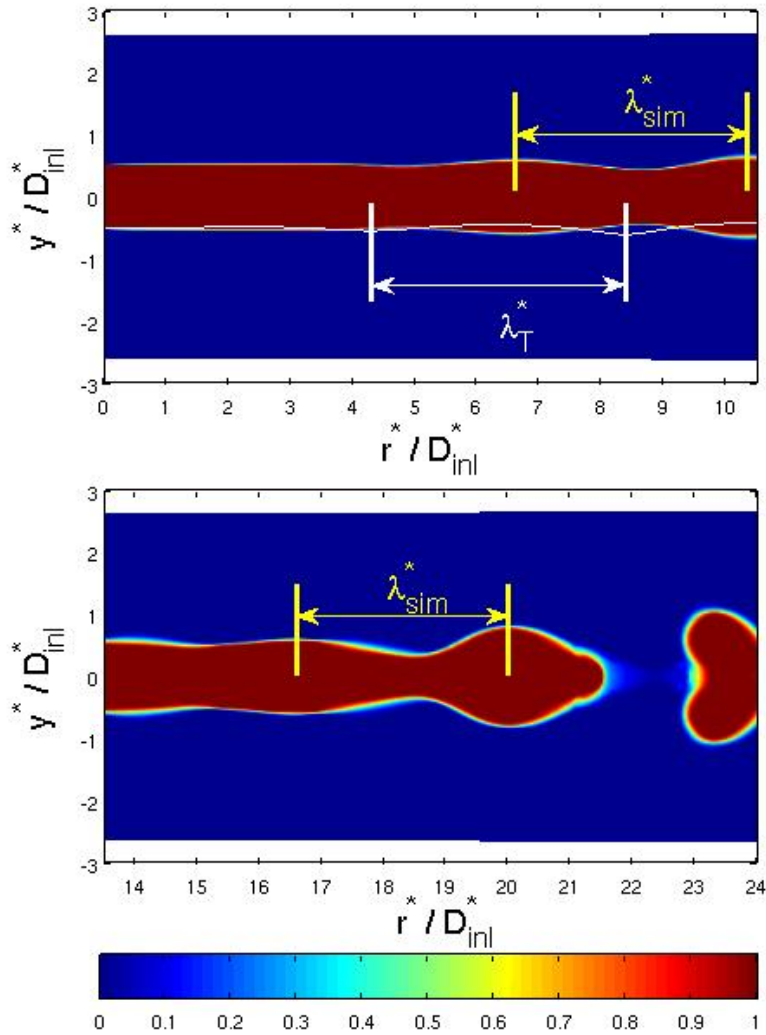


(b) Upper subfigure: Contours of the liquid color function, the dimensionless radius $R^*$ predicted by the travelling time theory plotted as white line, and the wave lengths $\lambda^*_{sim}$ and $\lambda^*_T$ in the near-field of the orifice.
Lower subfigure: The simulated wave length $\lambda^*_{sim}$ immediately upstream of the disintegration point.

Figure 6.5: Case I: $f = 100$ and $\epsilon = 2.5\%$; Solution obtained with the Koren flux limiter scheme.
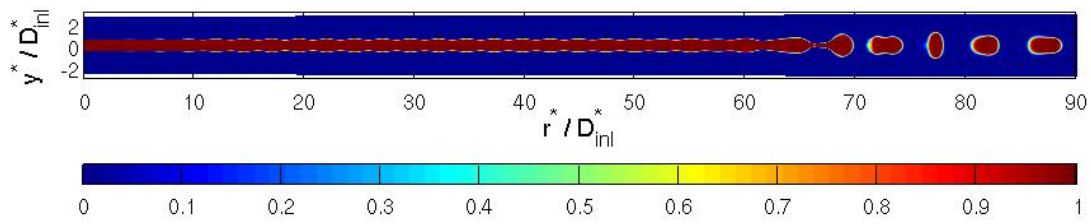
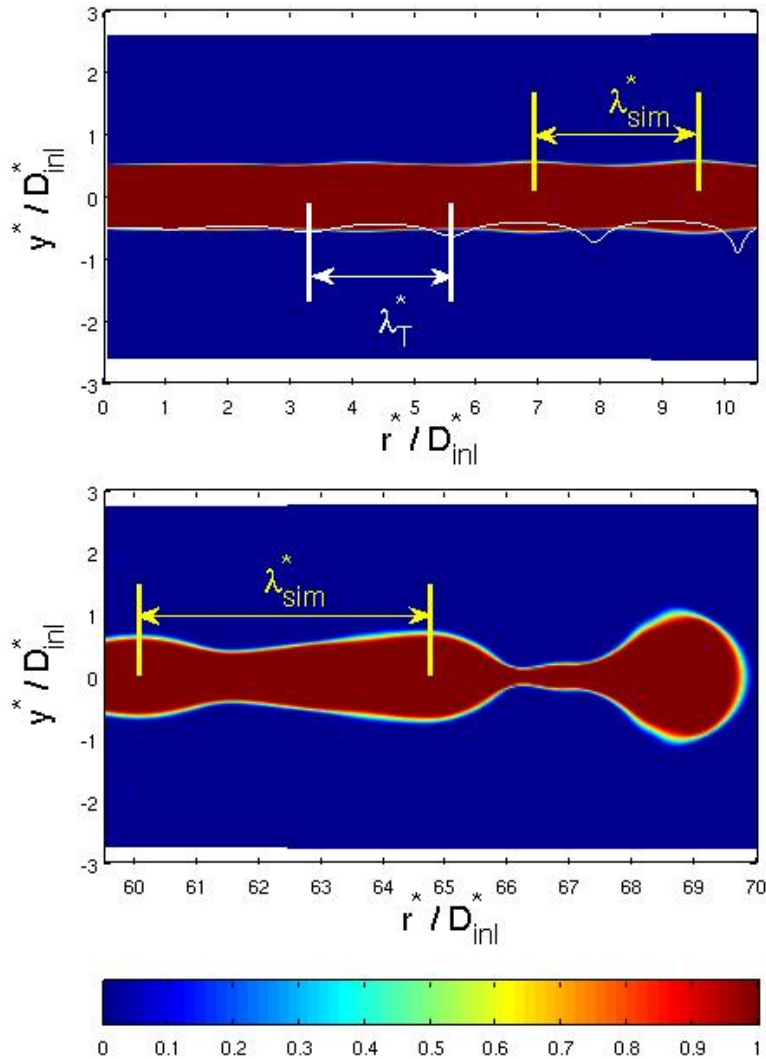(a) Contours of liquid color function at $t^* = 1.77$ shown in the full domain.



(b) Upper subfigure: Contours of the liquid color function, the dimensionless radius $R^*$ predicted by the travelling time theory plotted as white line, and the wave lengths $\lambda^*_{sim}$ and $\lambda^*_T$ in the near-field of the orifice.
Lower subfigure: The simulated wave length $\lambda^*_{sim}$ immediately upstream of the disintegration point.

Figure 6.6: Case II: $f = 100$ and $\epsilon = 5.0\%$; Solution obtained with the Koren flux limiter scheme.
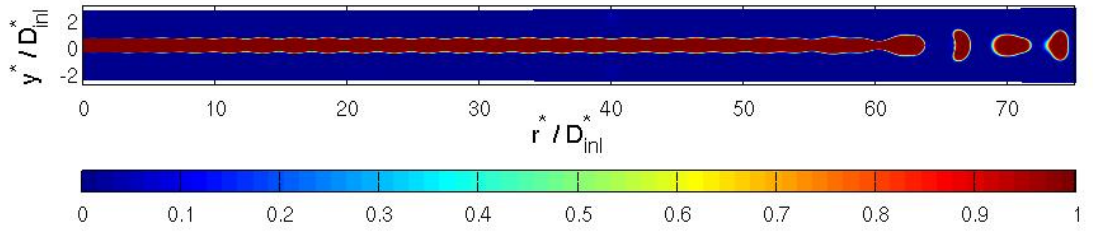
(a) Contours of liquid color function at $t^* = 8.18$ shown in the full domain.



(b) Upper subfigure: Contours of the liquid color function, the dimensionless radius $R^*$ predicted by the travelling time theory plotted as white line, and the wave lengths $\lambda^*_{sim}$ and $\lambda^*_T$ in the near-field of the orifice.
Lower subfigure: The simulated wave length $\lambda^*_{sim}$ immediately upstream of the disintegration point.

Figure 6.7: Case III: $f = 180$ and $\epsilon = 2.5\%$; Solution obtained with the Koren flux limiter scheme.

(a) Contours of liquid color function at $t^* = 5.19$ shown in the full domain.
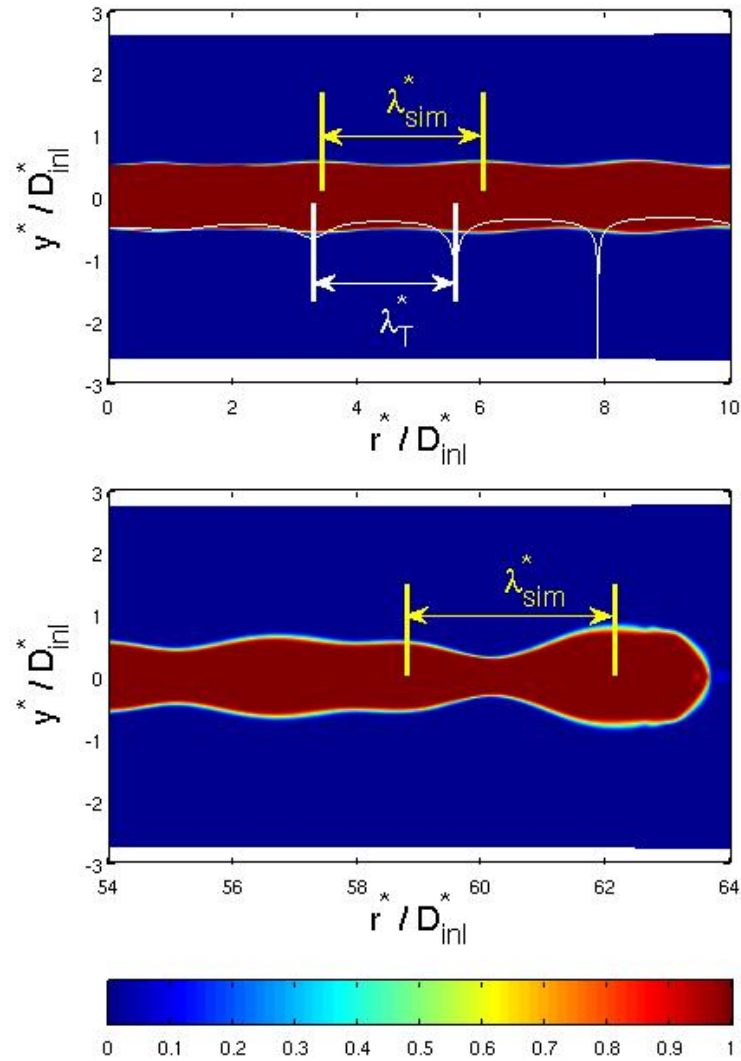


(b) Upper subfigure: Contours of the liquid color function, the dimensionless radius $R^*$ predicted by the travelling time theory plotted as white line, and the wave lengths $\lambda^*_{sim}$ and $\lambda^*_T$ in the near-field of the orifice.
Lower subfigure: The simulated wave length $\lambda^*_{sim}$ immediately upstream of the disintegration point.

Figure 6.8: Case IV: $f = 180$ and $\epsilon = 5.0\%$; Solution obtained with the Koren flux limiter scheme.

## 6.3.2 Numerical results obtained with the HRIC scheme

All numerical experiments described in this section are carried out using the HRIC scheme for capturing the liquid/gas interface. The same initial conditions were prescribed, as it was done in the computations with the Koren flux limiter scheme. Before describing the numerical results obtained with the HRIC scheme in detail one particular aspect of the implementation of the HRIC scheme shall be outlined in the following.

### Filtering of the color function

As mentioned above in subsection 2.3 using a rather compressive interface capturing scheme may cause spurious perturbations appearing as wrinkles in the iso-contour lines of the color function. These small scale irregularities generally lead to difficulties in the computation of the surface tension force $f_\sigma$, which is very sensitive to any local perturbations of the curvature computed from the instantaneous distribution of the color function. Using alternatively the rather diffusive Koren flux limiter scheme inherently produces a fairly smooth distribution of the color function, so that no such difficulty arises. This was not the case for the more compressive HRIC scheme, where the surface tension had to be computed from a solution of the colour function, which was smoothened by a filtering procedure. The effect of this procedure shall be demonstrated here by the results of a simple test simulation. As seen from the iso-contour lines of the liquid color function associated with the values $c = 0.1$, $0.5$, $0.9$, and $0.95$ in figure 6.9(a), the flow field is initialized with a cylindrical column of liquid, whose radius is $0.5D^*_{inl}$, and axial length is $2.5D^*_{inl}$. A uniform initial velocity field is prescribed for the liquid as well for the ambient gas, being $u^* = 10$ into the axial direction, and zero into all other directions. Imposing such a uniform velocity field the liquid should simply be advected downstream at a constant velocity $u^* = 10$, while it attains an ellipsoidal shape due the action of the capillary forces. In figure 6.9(b) the contour lines of the color function obtained with the Koren flux limiter scheme at $t^* = 7.0 \cdot 10^{-2}$ are shown. The contour lines of the color function obtained with the HRIC scheme at $t^* = 7.0 \cdot 10^{-2}$ without any filtering for the computation of the capillary forces are plotted in figure 6.9(c). While the liquid element reaches the expected axial position extending within $12D^*_{inl} \leq r^* \leq 14.5D^*_{inl}$ in the results of the Koren flux limiter scheme, the solution of the HRIC scheme stays evidently behind. Computing directly the surface tension force from the color function field produced by the HRIC scheme translates obviously into a significant retardation of the motion of the liquid. This unphysical retardation can be impeded by computing the surface tension forces with a spatially filtered representation of the color function. This can be clearly seen in figure 6.9(d), where the solution of the HRIC scheme using a filtered color function for the computation of the surface tension forces is shown. The artificial loss of momentum is sufficiently reduced, so that the axial distance passed by the liquid is nearly the same as in figure 6.9(b). A filtering procedure based on the Simpson rule, which is defined as

$$\mathcal{F}(c_i) = \frac{1}{6}c_{i-1} + \frac{2}{3}c_i + \frac{1}{6}c_{i+1}, \tag{6.3}$$

was applied here three times into radial and azimuthal directions $r^*$ and $\theta$, respectively. This filtering concept was used for all numerical simulations carried out with the HRIC scheme. By doing so the compressive nature of the HRIC scheme is preserved in the advection of the interface, while eventually occurring wrinkles in the solution for the color function do not unphysically perturb the surface tension force.

**Case I**

In figure 6.10(a) the solution of the color function is shown at $t^* = 2.17$. It can be seen that the disintegration length extends approximately to the point $r_p^* = 14.5D_{inl}^*$, which is only bit longer than the experimental one, i.e., $r_{p,exp}^* = 13.3D_{inl}^*$. For this case the HRIC scheme yields evidently a quantitatively much better agreement that the Koren flux limiter scheme, which considerably overpredicts $r_p^*$. Again the predicted diameters of the droplets are approximately of the double size of the initial diameter of the undeformed jet as predicted by the Rayleigh instability theory. The simulated wave length in the near-field of the orifice is obtained as $\lambda_{sim}^* = 3.9D_{inl}^*$, which is somewhat longer than that produced by the Koren flux limiter scheme. It is still shorter than the wave length predicted by the travelling time theory as seen from figure 6.10(b) in the upper plot, where the color function contours and the dimensionless radius of the jet $R^*$ given through equation (5.33) are shown. As seen from the lower subplot in figure 6.10(b) the simulated wave length near the breakup of the liquid is around $4.2D_{inl}^*$, which is somewhat greater than the value obtained in the near-field of the orifice.

**Case II**

In figure 6.11(a) the solution of the color function is shown at $t^* = 1.80$, which represents a bit more than two flow-though times. It can be observed that the disintegration length is $r_p^* = 11D_{inl}^*$. An increase of the amplitude from $\epsilon = 2.5\%$ to $\epsilon = 5.0\%$ for a fixed frequency $f = 100Hz$ evidently reduces the disintegration length predicted with the HRIC scheme. This reduction was not observed in the corresponding results of the Koren flux limiter scheme. The HRIC scheme even yields a fairly good quantitative agreement with the experimental results, where the disintegration length decreases to $r_p^* = 10D_{inl}^*$ as the amplitude $\epsilon$ is increased, as seen in figure 6.2. The simulated wave length in the near-field of the orifice predicted with the HRIC scheme is $\lambda_{sim}^* = 4.0D_{inl}^*$, which again exceeds somewhat the corresponding prediction of the Koren flux limiter scheme. Again the wave length predicted by the travelling time theory is greater than the wave length obtained from the simulation, as seen in figure 6.11(b) in the upper plot. The wave length measured from the simulated contours shown in the lower plot of 6.11(b) is around $3.9D_{inl}^*$. The wave lengths obtained in the near-field of the orifice and immediately upstream of the breakup are evidently almost the same.

**Case III**

In this particular case the domain length was increased to $100D_{inl}^*$ like in the case III for the Koren flux limiter scheme to ensure a sufficiently long axial distance of

the breakup zone to the outlet boundary. The converged solution shown in figure 6.12(a) at $t^* = 3.93$ exhibits a disintegration length around $70D^*_{inl}$. Similar to the solution obtained with the Koren flux limiter scheme the solution obtained with the HRIC scheme overpredicts the stabilizing effect of the increase in the frequency from $100Hz$ to $180Hz$ as compared to the experiments. Again the predicted diameters of the droplets are approximately of the double size of the initial diameter. The perturbation wave length obtained from the simulations in the near-field of the orifice is $\lambda^*_{sim} = 2.7D^*_{inl}$. In the upper plot of figure 6.12(b) it can be seen that the wave length predicted by the travelling time theory is smaller than the wave length predicted by the simulation in the near-field of the orifice. The tendency of a streamwise increasing simulated wave length before reaching the point of jet breakup can be from a comparison to the lower plot of figure 6.12(b), where a wave length $\lambda^*_{sim} = 3.5D^*_{inl}$ is measured.

**Case IV**

In figure 6.13(a) the numerical solution obtained with the HRIC scheme at $t^* = 3.2$ can be seen in the whole domain. Using the HRIC scheme predicts evidently almost the same quantitative reduction in the disintegration length for this case, as it was obtained with the Koren flux limiter scheme. With this respect the solution obtained with either scheme exhibits the right tendency, although the predicted disintegration lengths always exceed significantly the corresponding experimental values. The wave length in the near-field of the orifice predicted by the simulation is $\lambda^*_{sim} = 2.7D^*_{inl}$. In the upper plot of figure 6.13(b) it is well visible that the wave length in the near-field of the orifice is bigger than the wave length predicted by the travelling time theory. In figure 6.8(b) the lower plot indicates again an axial increase of wave length. The simulated wave length immediately upstream of the disintegration point seen in the lower plot of figure 6.8(b) is around $3.9D^*_{inl}$. Alike in case III the simulated wave length near the breakup of the liquid is greater than the wave length in the near-field of the orifice.
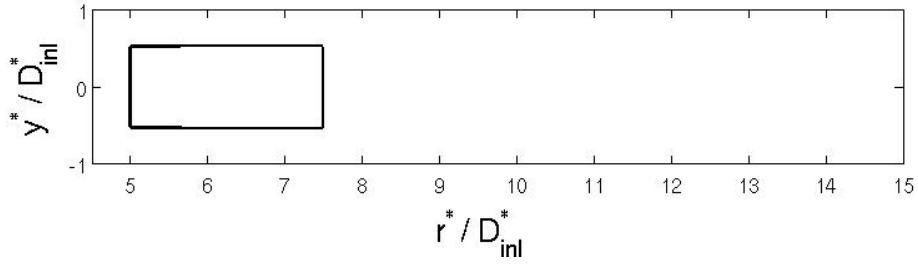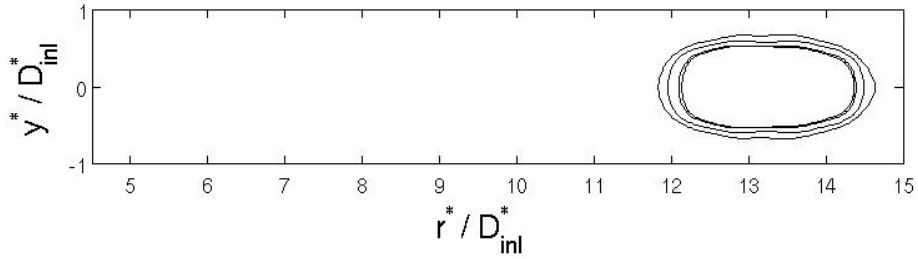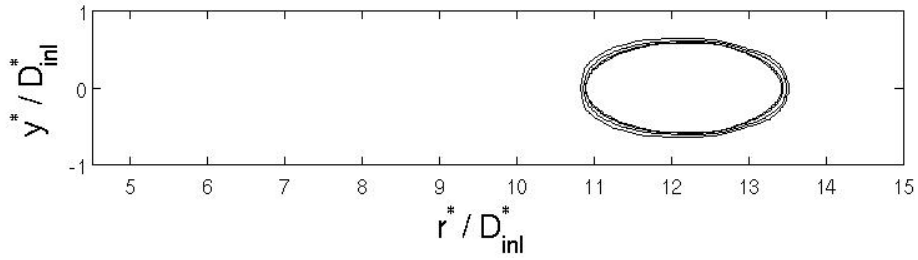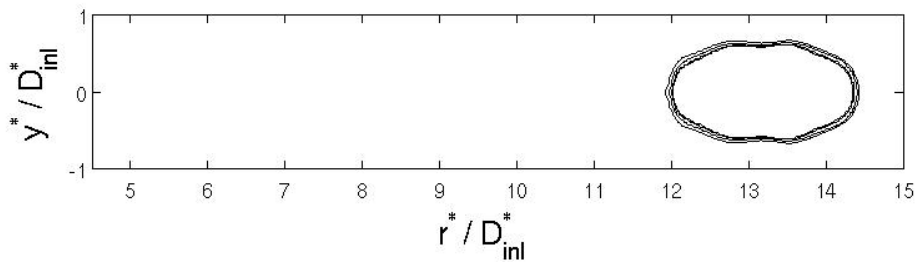
(a) Initial condition of the test simulation at $t^* = 0$.



(b) Contour lines at $t^* = 7 \cdot 10^{-2}$ obtained with the Koren flux limiter scheme.



(c) Contour lines at $t^* = 7 \cdot 10^{-2}$ obtained with the HRIC scheme using directly the color function for the computation of the surface tension forces without prefiltering.



(d) Contour lines at $t^* = 7 \cdot 10^{-2}$ obtained with the HRIC scheme using a filtered color function for the computation of the surface tension forces.

Figure 6.9: Test simulation of liquid cylinder moving in a uniform velocity field; contour lines of liquid color function associated with values $c = 0.1$, $0.5$, $0.9$, and $0.95$, at different times.
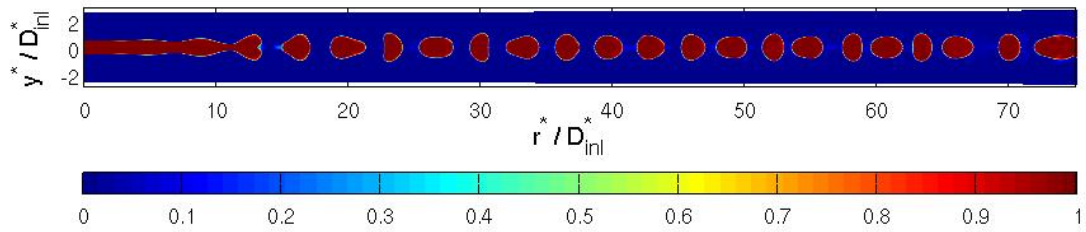
(a) Contours of liquid color function at $t^* = 2.17$ shown in the full domain.
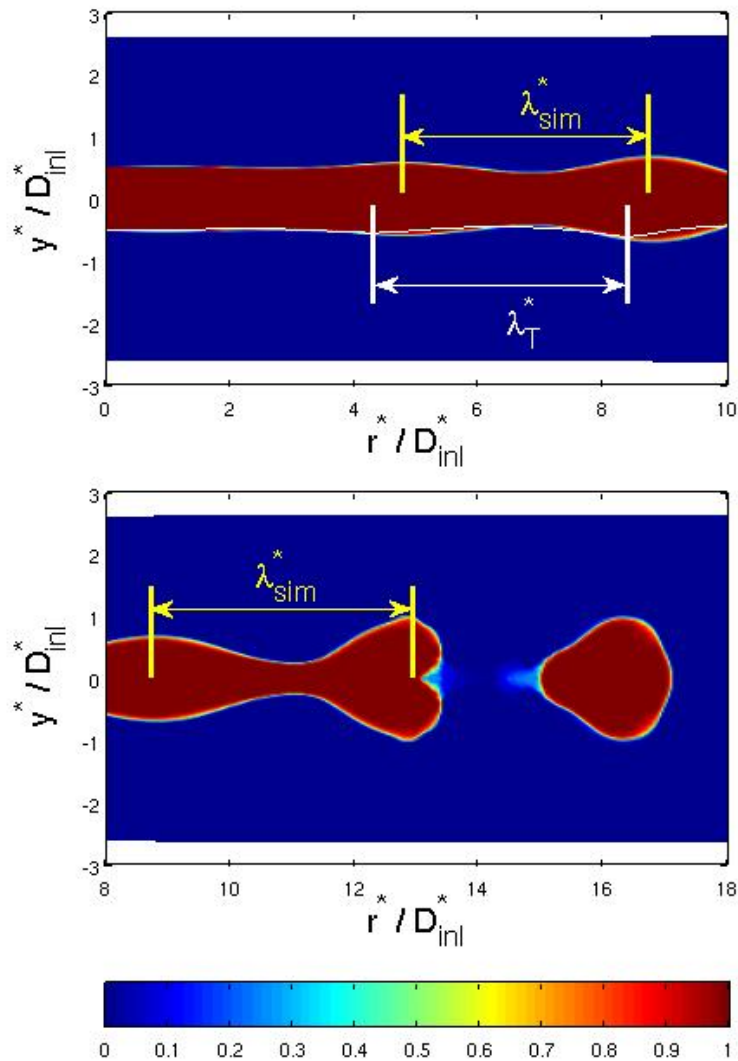


(b) Upper subfigure: Contours of the liquid color function, the dimensionless radius $R^*$ predicted by the travelling time theory plotted as white line, and the wave lengths $\lambda^*_{sim}$ and $\lambda^*_T$ in the near-field of the orifice.
Lower subfigure: The simulated wave length $\lambda^*_{sim}$ immediately upstream of the disintegration point.

Figure 6.10: Case I: $f = 100$ and $\epsilon = 2.5\%$; Solution obtained with the HRIC scheme.

(a) Contours of liquid color function at $t^* = 1.80$ shown in the full domain.



(b) Upper subfigure: Contours of the liquid color function, the dimensionless radius $R^*$ predicted by the travelling time theory plotted as white line, and the wave lengths $\lambda^*_{sim}$ and $\lambda^*_T$ in the near-field of the orifice.
Lower subfigure: The simulated wave length $\lambda^*_{sim}$ immediately upstream of the disintegration point.

Figure 6.11: Case II: $f = 100$ and $\epsilon = 5.0\%$; Solution obtained with the HRIC scheme.
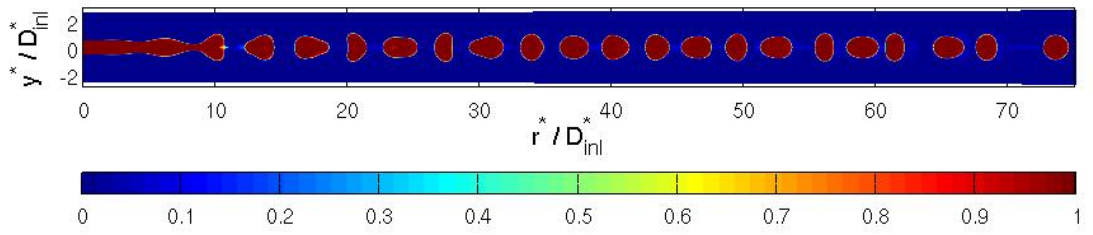
(a) Contours of liquid color function at $t^* = 4.81$ shown in the full domain.
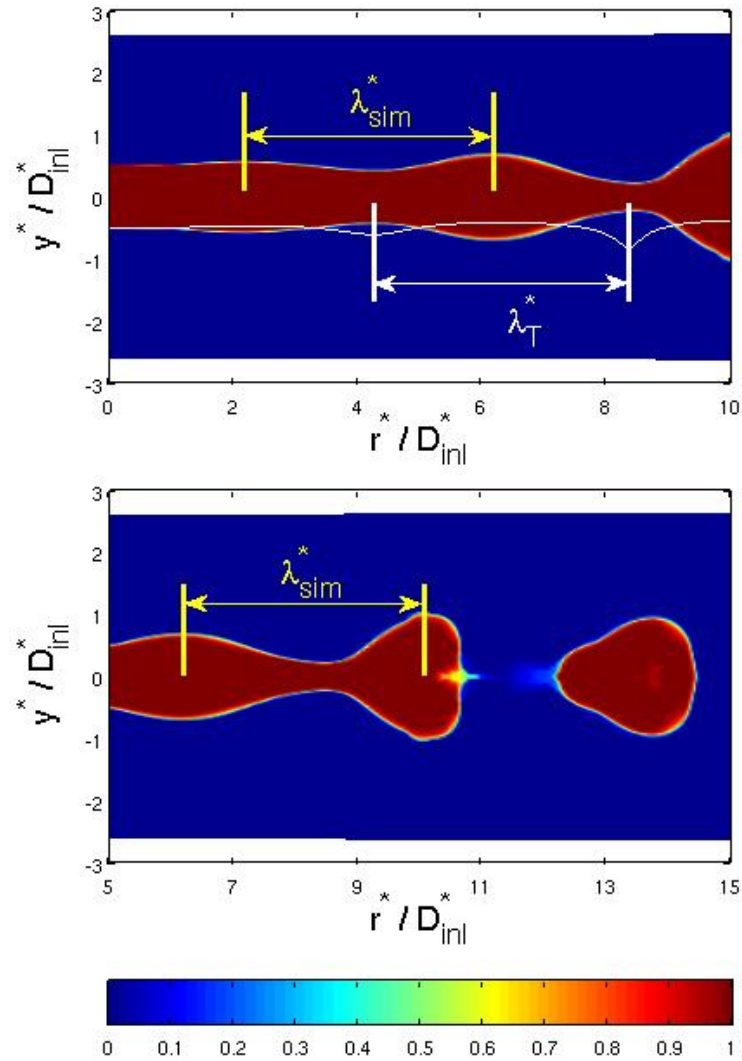


(b) Upper subfigure: Contours of the liquid color function, the dimensionless radius $R^*$ predicted by the travelling time theory plotted as white line, and the wave lengths $\lambda^*_{sim}$ and $\lambda^*_T$ in the near-field of the orifice.
Lower subfigure: The simulated wave length $\lambda^*_{sim}$ immediately upstream of the disintegration point.

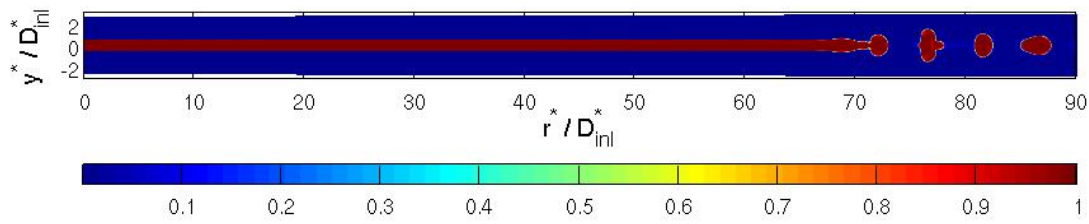Figure 6.12: Case III: $f = 180$ and $\epsilon = 2.5\%$; Solution obtained with the HRIC scheme.

(a) Contours of liquid color function at $t^* = 3.2$ shown in the full domain.
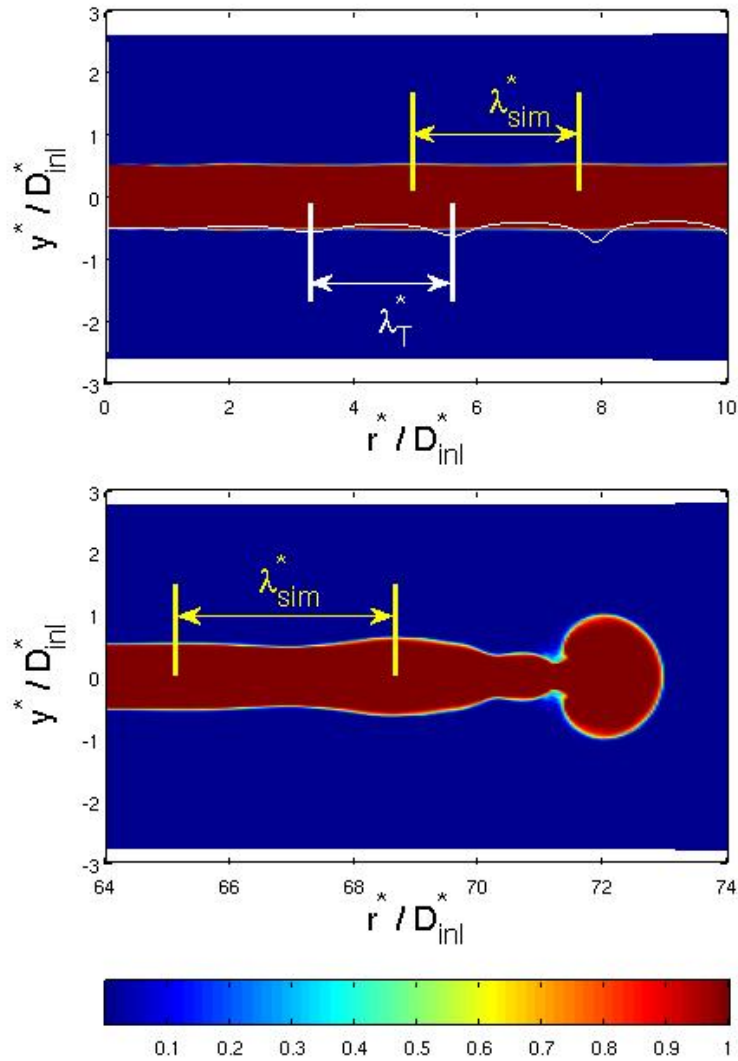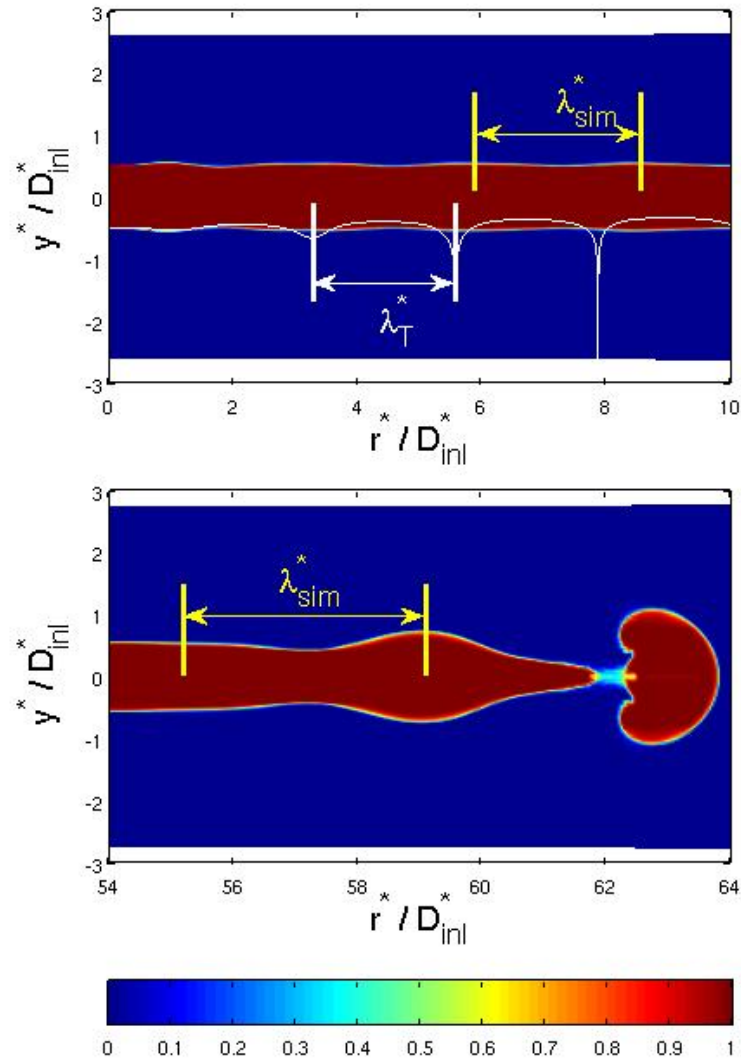


(b) Upper subfigure: Contours of the liquid color function, the dimensionless radius $R^*$ predicted by the travelling time theory plotted as white line, and the wave lengths $\lambda^*_{sim}$ and $\lambda^*_T$ in the near-field of the orifice.
Lower subfigure: The simulated wave length $\lambda^*_{sim}$ immediately upstream of the disintegration point.

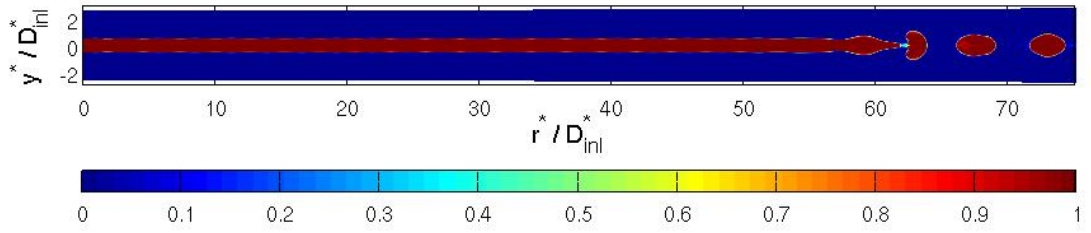Figure 6.13: Case IV: $f = 180$ and $\epsilon = 5.0\%$; Solution obtained with the HRIC scheme.

# 6.4 Interpretation and discussion

In table 6.3 the essential parameters and results obtained from the numerical and analytical computations, and from the experiments for all cases I, II, III and IV are summarized for comparison.

The abbreviation $KFL$ stands for Koren flux limiter. The simulated wave length in the near-flied of the orifice is indicated by the abbreviation $ori$. The simulated wave length immediately upstream of the disintegration point is indicated by the abbreviation $dp$. The subscript $exp$ refers to the experimental results, and the subscript $T$ to the travelling time theory.

| Case | VOF scheme | $f$ (in $Hz$) | $\epsilon$ (in %) | $r_p^*/D_{inl}^*$ | $\lambda_{sim}^*/D_{inl}^*$ (ori) | $\lambda_{sim}^*/D_{inl}^*$ (dp) | $r_{p,exp}^*/D_{inl}^*$ | $\lambda_T^*/D_{inl}^*$ | $r_{p,T}^*/D_{inl}^*$ |
|------|------------|---------------|-------------------|-------------------|-----------------------------------|----------------------------------|-------------------------|-------------------------|-----------------------|
| I | KFL | 100 | 2.5 | 22 | 3.7 | 3.4 | 13.3 | 4.2 | 26.5 |
| II | KFL | 100 | 5.0 | 22 | 3.5 | 3.6 | 10.0 | 4.2 | 13.2 |
| III | KFL | 180 | 2.5 | 70 | 2.7 | 4.7 | 27.8 | 2.3 | 14.7 |
| IV | KFL | 180 | 5.0 | 64 | 2.6 | 3.4 | 8.9 | 2.3 | 7.3 |
| I | HRIC | 100 | 2.5 | 14.5 | 3.9 | 4.2 | 13.3 | 4.2 | 26.5 |
| II | HRIC | 100 | 5.0 | 11 | 4.0 | 3.9 | 10.0 | 4.2 | 13.2 |
| III | HRIC | 180 | 2.5 | 73 | 2.7 | 3.5 | 27.8 | 2.3 | 14.7 |
| IV | HRIC | 180 | 5.0 | 62 | 2.7 | 3.9 | 8.9 | 2.3 | 7.3 |

Table 6.3: Essential parameters and results obtained from the computations and experiments.

As a salient feature the numerical simulations predicted a longer disintegration length $r_p^*$ than it was observed in the experiments for all cases. With this respect the most significant deviation between the experimental results and the numerical results appears in case IV, and the best agreement is found in case I in the prediction obtained with the HRIC scheme.

In general, the HRIC scheme still produced a better agreement with the experiments than the Koren flux limiter scheme. This indicates that using a rather diffusive scheme like the Koren flux limiter may effectively exert a stabilizing effect, which shifts the breakup of the liquid farther downstream. Accordingly, the stabilizing effect appears as less pronounced in the results of the less diffusive, i.e., more compressive, HRIC scheme.

In the cases I and II the predicted disintegration lengths of the HRIC scheme come quantitatively very close to the experimental results. The predictions reflect very well the experimentally observed decrease in the disintegration length as the amplitude $\epsilon$ is increased from 2.5% to 5%. This reduction is not featured by the results obtained with the Koren flux limiter scheme for the cases I and II.

Assuming the travelling time theory the wave length of the perturbation of the liquid

surface is analytically obtained from equation (5.38) dependent of the frequency and the amplitude. As such it does not vary with streamwise position. Considering rather small amplitudes $\epsilon = 0.025$ and $\epsilon = 0.05$ the wave lengths are always very close to $\frac{\lambda_T}{D_{inl}} \approx \frac{u_{jet}}{f D_{inl}}$. The wave lengths, which were measured from the numerically obtained contours of the liquid color function, expectedly reflect this inverse dependence of frequency in the region close to the orifice as well.

It is interesting to note that the simulations predict near the nozzle always somewhat shorter wave lengths than the travelling time theory for the cases with the smaller frequency (cases I and II), while they do the opposite for the cases with the higher frequency (cases III and IV).

For the cases I and II the numerically predicted wave lengths do not significantly change downstream to the point of liquid breakup. In contrast, for the cases III and IV the predicted wave lengths become significantly longer immediately upstream of the breakup. Rayleigh's theory on capillary breakup offers a possible explanation for this observed increase. One essential conclusion of the Rayleigh instability theory is, see equation (5.22), that only perturbations with a wave number in the range

$$0 < kh_0 < 1 \tag{6.4}$$

can lead to capillary instabilities under the assumption that $\bar{h} \approx h_0$. Using $k = \frac{2\pi}{\lambda}$, $D_{inl} = 2h_0$ and $\lambda = \frac{u_{jet}}{f}$ the condition (6.4) can be rewritten as

$$0 < \frac{\pi f D_{inl}}{u_{jet}} < 1. \tag{6.5}$$

Substituting $u_{jet} = 1m/s$, $D_{inl} = 2.4 \cdot 10^{-3}m$ and the frequency $f = 100Hz$ yields

$$kh_0 = \frac{\pi f D_{inl}}{u_{jet}} = 0.75.$$

Thus, a stimulation of the capillary instabilities is caused by a perturbation signal with a frequency $f = 100Hz$. It is not far away from the fastest growing mode, which occurs at $kh_0 = 0.697$, see figure 5.3. For a frequency $f = 180Hz$ it follows

$$kh_0 = \frac{\pi f D_{inl}}{u_{jet}} = 1.36.$$

Thus, no stimulation of the capillary instabilities is triggered by a perturbation frequency $f = 180Hz$, because $kh_0 \geq 1$. This explains the extended disintegration lengths and longer perturbation wave lengths upstream of the breakup, as the initially introduced high frequency perturbation has to be propagated farther downstream until a low frequency mode associated with long wave length has grown strong enough to cause a capillary breakup. Accordingly, the wave lengths observed in the numerical results for the cases III and IV are increased from the level introduced at the orifice to a higher level upstream of the breakup, which satisfies the condition (6.4). This increase is not observed in the cases I and II, where the initially introduced wave number of

the perturbation already satisfies the condition (6.4), necessary for capillary breakup according to Rayleigh's theory.

Is the numerically predicted phenomenon of a shift to higher wave lengths also observed in real flow experiments? This question can't be answered satisfactorily based on the underlying experimental results. The resolution of the used pictures is too low to obtain wave lengths especially in the near-field of the orifice. Further experimental studies are necessary. Nevertheless in all the experimental results the droplets had roughly the double size of the inlet diameter, which is consistent with the Rayleigh instability theory on capillary breakup.

The numerical results obtained with either interface capturing scheme could reproduce the increase in the disintegration length caused by the increase of the frequency of the inlet velocity perturbation, as observed in the experiments in case III. Despite this good qualitative agreement, the predicted increase of the disintegration length exceeds significantly the experimentally observed value. This quantitative discrepancy clearly illustrates the limits of the presently used VOF based schemes for predicting accurately the position of liquid breakup. This shortcoming is not surprising. The breakup of a continuous portion of liquid into individual droplets basically involves a singularity, because the relevant length scale, i.e., the thickness of the liquid locally goes to zero. This pages a fundamental problem to any numerical simulation, because it is impossible to resolve a vanishing length scale. A further possible source of the observed quantitative disagreement can be associated with the idealized boundary condition at the inlet, which can cause a stabilizing effect. The prescribed box-shaped velocity profile contains less kinetic energy than the real rather curved velocity profile. As a consequence, less kinetic energy is available to be transformed into surface energy and back, which is the underlying mechanism of the capillary instability. As such, possible differences to the real inlet boundary conditions can also help to explain, why the simulated disintegration length $r_p^*$ was always longer than the experimental disintegration length $r_{p,exp}^*$.

As for the effect of the change in the amplitude of the perturbation the simulations always show the correct tendency, i.e., a reduced disintegration length as the amplitude is increased. This is consistent with the experiments, although the predicted disintegration lengths quantitatively disagree considerably especially in the high frequency cases III and IV.

The travelling time theory has proven some potential to describe the accumulation of material in the perturbed liquid column near the orifice. However, interpreting the occurrence of the first singularity, where the analytically predicted radius goes to infinity, as streamwise position of the liquid breakup yields no adequate description of this phenomenon. Being based only on kinematic wave propagation and neglecting the effect of surface tension the analytical solution given by equation (5.36) always predicts reduced disintegration lengths for increased perturbation frequencies and/or amplitudes. This is exactly the opposite tendency of that observed in the case III in both the experiments and in the numerical results.

# 7 Conclusions and Outlook

The influence of kinematic waves on jet breakup has been computationally investigated. The considered scenario is a liquid (water) free jet surrounded by a gas (air) with much lower density. The mathematical formulation used for the numerical simulation is based on an one single fluid approach, so that in the whole domain of interest just one single set of governing equations is solved. A color function was introduced to distinguish the liquid from the gas phase. The continuum surface force (CSF) model was used to account for surface tension effects. Two different VOF methods for capturing the liquid/gas interface, the Koren flux limiter scheme and the HRIC scheme, were implemented and compared. The performance of the HRIC scheme is of special interest, because it is used in popular commercial CFD software (e.g. Comet, Fluent). Eight numerical simulations were performed imposing a certain variation of sinusoidal velocity modulations at the inlet. The obtained numerical solutions were compared against the corresponding experimental observations of Meier et al. (1992) and against the predictions of the travelling time theory (Grabitz and Meier, 1983).

In summary, the following conclusions can be drawn from the computational investigations:

- The numerical simulation predicted in general more stable jet flow conditions than observed in the experiments. This means that in every numerical experiment the predicted disintegration length was longer than that of the experiments. This quantitative disagreement does not only reveal possible deficiencies of the applied schemes, it also points at the fundamental problem of liquid breakup, which involves a vanishing spatial length scale excluding an numerical resolution. Possible differences of the prescribed inflow conditions to the real condition may be an additional reason for the observed deviations.

- The HRIC scheme gives in general a better agreement with the experimental results than the Koren flux limiter scheme. This is especially seen for the cases I and II associated with the lower frequency of the velocity modulation.

- In all numerical experiments the simulated wave length in the near-field of the orifice was somewhat different from the wave length predicted by the travelling time theory. The differently predicted clustering of the flow material can be attributed to the effect of surface tension and viscous forces, which are neglected by the travelling time theory.

- In the case III the numerical results reflect correctly the experimentaly observed stabilizing tendency, but not the quantitative extent of the changes. The stabilizing effect can be explained based on the Rayleigh instability theory, because

the imposed inlet velocity perturbations in the case III are associated with wave numbers, which are outside the stimulation range $0 < kh_0 < 1$.

- In all numerical simulations the correct tendency of the effect of the change in the amplitude is obtained. Increasing the amplitude yields to a reduced disintegration length, which is consistent with the experiments.

- A streamwise increase of the simulated wave lengths could be observed in the cases III and IV. The simulated wave lengths immediately upstream of the breakup reached a level which always satisfies the inequality $0 < kh_0 < 1$.

Based on the results obtained in this work, suggestions for possible improvements and future work are proposed, as outlined below:

- Investigation of the influence of the perturbed inflow velocity profile: A modulated parabolic velocity profile should be prescribed at the inlet as an alternative to the modulated box-shaped profile.

- Using an alternative concept for describing the two-phase flow instead of the VOF approach, for example a level set approach.

- Further real flow experiments in the capillary breakup regime could be made to examine if the predicted streamwise increase of the wave lengths is also visible in real flow experiments.

- More numerical simulations could be made to determine a specific frequency $f_{max}$ and amplitude $\epsilon_{max}$, where the disintegration length $r^*_{p,max}$ reaches a maximum. The same could be made to determine the modulation which leads to a minimum disintegration length $r^*_{p,min}$.

# Bibliography

Atias, M., Wolfshtein, M., and Israeli, M. (1977). Efficiency of Navier-Stokes solvers. *AIAA Journal*, 15(2):263–266.

Boersma, B. (1998). Direct simulation of a jet diffusion flame. *Center for Turbulence Research Annual Research Briefs*, pages 47–56.

Brackbill, J., Kothe, D., and Zemach, C. (1992). A Continuum Method for Modelling Surface Tension. *Journal of Computational Physics*, 100:335–354.

Daly, B. (1967). Numerical study of two fluid Rayleigh-Taylor instability. *The Physics of Fluids*, 10(2):297–307.

Daly, B. (1969). A technique for including surface tension effects in hydrodynamic calculations. *Journal of Computational Physics*, 4:97–117.

Darvish, M. (1993). A New High-Resolution Scheme Based on the Normalized Variable Formulation. *Numerical Heat Transfer, Part B*, 24:353–373.

Duclaux, V. and Clanet, C. (2004). Does Plateau-Rayleigh instability occur in our lungs? In *American Physical Society, 57th Annual Meeting of the Division of Fluid Dynamics*, pages 21–23.

Ferziger, J. and Peric, M. (1996). *Computational Methods for Fluid Dynamics*. Springer, Berlin Heidelberg.

Fröhlich, J. (2006). *Large Eddy Simulation turbulenter Strömungen*. Teubner, Wiesbaden.

Gaskell, P. and Lau, A. (1988). Curvature-compensated convective transport: SMART, a new boundedness-preserving transport algorithm. *Int. Journal for Numerical Methods in Fluids*, 8:617–641.

Glimm, J., McBryan, O., Menikoff, R., and Sharp, D. (1986). Front tracking applied to Rayleigh-Taylor instability. *SIAM Scientific and Statistical Computing*, 7(1):230–251.

Goedde, E. and Yuen, M. (1970). Experiments on liquid jets instability. *Journal of Fluid Mechanics*, 40:495–511.

Grabitz, G. and Meier, G. (1983). Über Laufzeitinstabilitäten in Flüssigkeitsstrahlen. *Zamm*, 63:255–257.

Haenlein, A. (1931). Über den Zerfall eines Flüssigkeitsstrahles. *Forschung 2*, 4:139–148.

Harlow, F. and Welch, E. (1965). Numerical calculation of time-dependent viscous incompressible flow of fluid with free surface. *The Physics of Fluids*, 8(12):2182–2189.

Harten, A. (1983). High Resolution Schemes for Hyperbolic Conservation Laws. *Journal of Computational Physics*, 49:357–393.

Heidron, D. and Steiner, H. (2009). Subgrid-scale interface model for atomizing high-speed liquid jets. *Turbulence Heat and Mass Transfer*, 6:791–794.

Hirt, C. and Nichols, B. (1981). Volume of fluid (VOF) method for dynamics of free boundaries. *Journal of Computational Physics*, 39:201–221.

Keller, J. and Rubinow, S. (1973). Spatial instability of a jet. *Physics of Fluids*, 16:2052–2055.

Koren, B. (1993). A robust upwind discretization method for advection, diffusion and source terms. In *Numerical Methods for Advection-Diffusion Problems*, pages 117–138. Braunschweig/Wiesbaden.

Leer, B. V. (1985). Upwind-difference methods for aerodynamic problems governed by the Euler equations. *Lectures in Applied Mathematics*, 22:327–336.

Leonard, B. (1979). A stable and accurate convection modelling procedure based on quadratic interpolation. *Computer Methods in Applied Mechanics and Engineering*, 19:59–98.

López, J. and Hernández, J. (2008). Analytical and geometrical tools for 3d volume of fluid methods in general grids. *Journal of Computational Physics*, 227:5939–5848.

Meier, G., Klöpper, A., and Grabitz, G. (1992). The influence of kinematic waves on jet break down. *Experiments in Fluids*, 12:173–180.

Muzaferija, S., Peric, M., Sames, P., and Schellin, T. (1998). A Two-Fluid Navier-Stokes Solver to Simulate Water Entry. *Proc. Twenty-Second Symposium on Naval Hydrodynamics*, pages 638–649.

Noh, W. and Woodward, P. (1976). SLIC (Simple Line Interface Calculations). *Lecture Notes in Physics*, 59:330–340.

Ohnesorge, W. (1936). Die Bildung von Tropfen an Düsen und die Auflösung flüssiger Strahlen. *ZAMM - Journal of Applied Mathematics and Mechanics*, 16:355–258.

Pilliod, J. E. and Puckett, E. G. (2004). Second-order accurate volume-of-fluid algorithms for tracking material interfaces. *Journal of Computational Physics*, 199:465–502.

Prosperetti, A. and Tryggvason, G. (2007). *Computational Methods for Multiphase Flows.* Cambridge University Press, New York.

Ramaswamy, B. and Kawahara, M. (1987). Lagrangian finite element analysis applied to viscous free surface fluid flow. *Numerical Methods in Fluids*, 7:953–984.

Rayleigh, L. (1878). On the instability of jets. *Proceedings of the London mathematical society*, 10:4–13.

Roe, P. (1987). Finite-volume methods for the compressible Navier-Stokes equations. In *Proceedings of the 5th International Conference on Numerical Methods in Laminar and Turbulent Flow*, pages 2088–2101. Pineridge Press.

Scardovelli, R. and Zaleski, S. (1999). Direct numerical simulation of free-surface and interfacial flow. *Annual Reviews of Fluid Dynamics*, 31:567–603.

Spurk, J. and Aksel, N. (2007). *Strömungslehre.* Springer, Berlin Heidelberg.

Sweby, P. (1984). High Resolution Schemes Using Flux Limiters for Hyperbolic Conservation Laws. *SIAM Journal on Numerical Analysis*, 21(5):995–1011.

Ubbink, O. (1997). *Numerical prediction of two fluid systems with sharp interfaces.* PhD thesis, University of London, London, UK.

Walchshofer, C. (2011). *Analysis of the Dynamics at the Base of a Lifted Strongly Buoyant Jet Flame Using Direct Numerical Simulation.* PhD thesis, Technical University of Graz, Graz, AUT.

Waterson, N. and Deconinck, H. (2007). Design principles for bounded higher-order convection schemes - a unified approach. *Journal of Computational Physics*, 224:182–207.

Wei, J. J., Yo, B., and Tao, W. (2007). A new General Convective Boundedness Criterion. *Numerical Heat Transfer, Part B*, 49:585–598.

Youngs, D. (1982). Time-dependent multi-material flow with large fluid distortion. In *Numerical methods for fluid dynamics*, pages 273–285. London Academic Press.

Yu, B., Tao, W., Zhang, D., and Wang, Q. (2001). Discussion on numerical stability and boundedness of convective discretized schemes. *Numerical Heat Transfer, Part B*, 40:343–365.

# Eidesstattliche Erklärung

Ich erkläre an Eides statt, dass ich die vorliegende Arbeit selbständig verfasst, andere als die angegebenen Quellen/Hilfsmittel nicht benutzt, und die den benutzten Quellen wörtlich und inhaltlich entnommenen Stellen als solche kenntlich gemacht habe.

Graz, am . . . . . . . . . . . . . . . . . . . . . . .        . . . . . . . . . . . . . . . . . . . . . . . . . . . . . . . . . . . . . . .
                                                            (Unterschrift)


# Statutory Declaration

I declare that I have authored this thesis independently, that I have not used other than the declared sources/resources, and that I have explicitly marked all material which has been quotes either literally or by content from the used sources.

. . . . . . . . . . . . . . . . . . . . . . . . . . . . .        . . . . . . . . . . . . . . . . . . . . . . . . . . . . . . . . . . . . . . .
            date                                                    (signature)